

**M.Sc. in Climate Change**

# **Committed mass loss of Mittivakkat glacier from optical remote sensing**

Jasper Lennard Heuer

Supervised by Jason E. Box (GEUS) and Rasmus Fensholt (IGN)

15th of August 2024



**Jasper Lennard Heuer**

*Committed mass loss of Mittivakkat glacier from optical remote sensing*

M.Sc. in Climate Change, 15th of August 2024

Supervisors: Jason E. Box (GEUS) and Rasmus Fensholt (IGN)

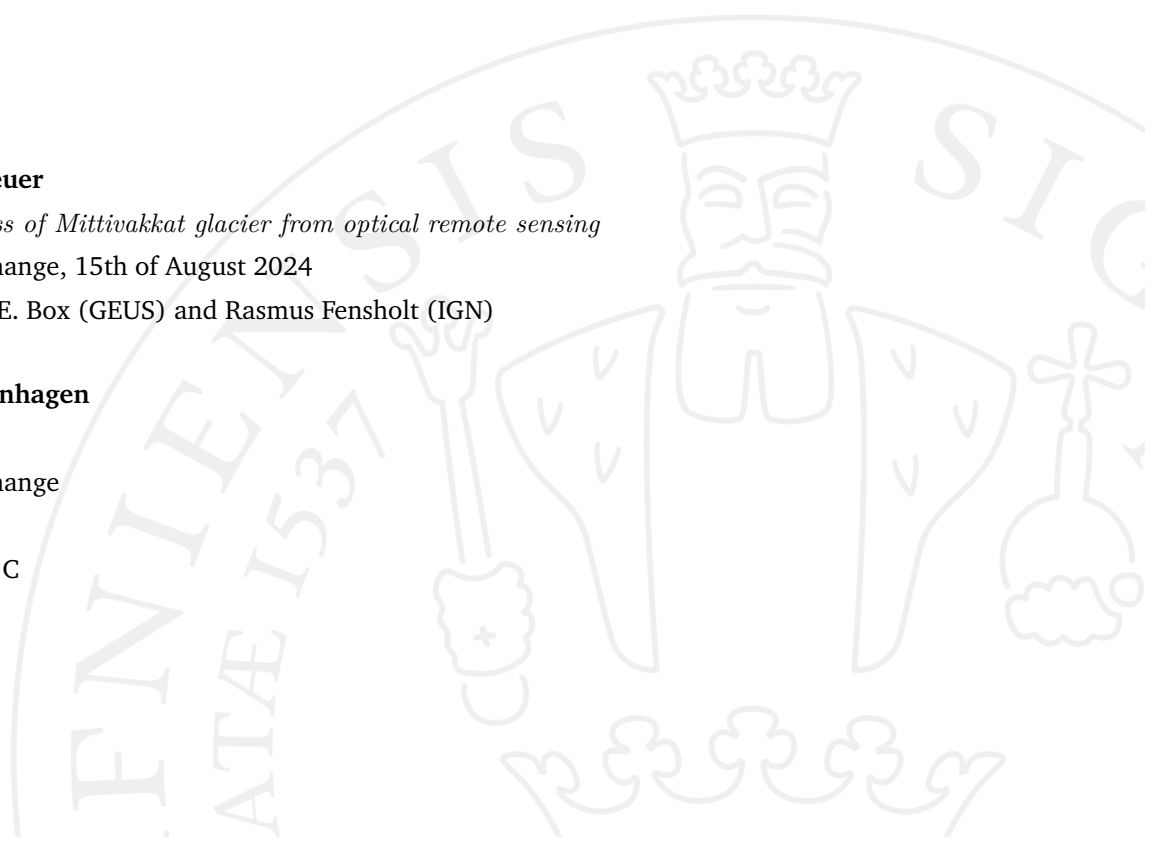
**University of Copenhagen**

*Faculty of Science*

M.Sc. in Climate Change

Bülowsvej 17

1870 Frederiksberg C



*"A man who keeps company with glaciers comes  
to feel tolerably insignificant by and by."*

Mark Twain, 1880

*"I will bully you relentlessly if you put a pretentious Mark Twain  
quote in your thesis, so please do."*

Zoe Carr, 2024

# Abstract

By regressing the ratio between the accumulation area and the total area of a glacier (AAR) against its annual mass balance, one can determine the degree to which the glacier is out of balance with the current climate. This degree of imbalance conveniently serves as a measure of the area adjustment the glacier needs to undergo in order to be in dynamic equilibrium with the climate again. The corresponding volume change can then be estimated based on glaciological scaling theory in order to establish a lower bound of the expected mass loss, known as the committed mass loss.

Despite their large contribution to global sea level rise, only 5 of the roughly 20,000 glaciers and ice caps peripheral to the Greenland ice sheet have on-going mass balance observation programs due to the logistical challenges associated with field work in Greenland. A fully remote methodology for the estimation of the committed mass loss of these glaciers can therefore serve as a justifiable, complementary approach to monitor their response to the changing climate and enable decision- and policymakers to adept to the resulting impacts.

In this study, a Python-based tool chain is presented that uses Landsat satellite imagery and MAR climate reanalysis mass balance data to calculate the committed mass loss of a glacier. The tool chain is then validated against in-situ observations at Mittivakkat glacier, the only glacier with an on-going, long-term mass balance observation program in Greenland. Based on this remote approach, Mittivakkat is projected to lose 39% of its area and 50% of its volume, notably less than the 72% area loss and 83% volume loss estimated based on in-situ observations. These differences likely arise from multiple sources, first and foremost the low accuracy of the surface classification algorithm used to estimate the AAR and the low temporal resolution of the Landsat imagery. Other sources of uncertainty include the low spatial resolution of the mass balance data and the fact that the tool chain is currently unable to mask out small patches of snow that distort the AAR.

When these issues are resolved, however – for instance through the use of high resolution satellite imagery and more advanced surfaces classification algorithms – the tool chain presented in this study promises to be a valuable asset to glacier monitoring efforts in Greenland and other remote and inaccessible regions.

# Contents

<b>1</b>	<b>Introduction</b>	<b>1</b>
1.1	Global glacier melt . . . . .	1
1.2	Glacier melt in Greenland . . . . .	2
1.3	Objectives of the thesis . . . . .	4
1.4	Structure of the thesis . . . . .	4
<b>2</b>	<b>Glossary</b>	<b>6</b>
2.1	Glaciology . . . . .	6
2.2	Remote sensing . . . . .	7
<b>3</b>	<b>Study area</b>	<b>8</b>
3.1	Surrounding topography . . . . .	8
3.2	Scientific research . . . . .	9
3.3	Climatology . . . . .	10
3.3.1	Ammassalik region . . . . .	10
3.3.2	Mittivakkat glacier . . . . .	12
3.3.3	Climate and large-scale circulations . . . . .	13
3.4	Recent changes at Mittivakkat . . . . .	16
<b>4</b>	<b>Data</b>	<b>18</b>
4.1	Digital elevation model (DEM) . . . . .	18
4.2	Modèle Atmosphérique Régional (MAR) . . . . .	18
4.3	Randolph Glacier Inventory (RGI) . . . . .	20
4.4	WGMS Fluctuations of Glaciers (FoG) . . . . .	20
4.5	Landsat imagery . . . . .	20
4.5.1	The Landsat program . . . . .	21
4.5.2	Caveats and limitations . . . . .	22
4.5.3	Cloud masking . . . . .	22
4.5.4	Data sets and access . . . . .	23
<b>5</b>	<b>Methodology</b>	<b>24</b>
5.1	Background . . . . .	24
5.2	Workflow . . . . .	26
5.2.1	Retrieval of Landsat imagery . . . . .	27

5.2.2	Pre-processing . . . . .	30
5.2.3	Surface classification . . . . .	30
5.2.4	ELA and AAR calculation . . . . .	30
5.2.5	Surface mass balance calculation . . . . .	31
<b>6</b>	<b>Results</b>	<b>33</b>
6.1	Equilibrium-line altitude (ELA) . . . . .	33
6.1.1	Original data . . . . .	33
6.1.2	Comparison with WGMS data . . . . .	35
6.2	Accumulation area ratio (AAR) . . . . .	36
6.2.1	Original data . . . . .	36
6.2.2	Comparison with WGMS data . . . . .	38
6.3	Surface mass balance (SMB) . . . . .	39
6.3.1	Original data . . . . .	39
6.3.2	Comparison with WGMS data . . . . .	41
6.4	Glacier area . . . . .	42
6.5	Length of hydrological year . . . . .	44
6.6	AAR-SMB regression . . . . .	46
6.6.1	Original data . . . . .	46
6.6.2	Comparison with WGMS data . . . . .	47
6.6.3	Comparison of SMB-AAR regression periods . . . . .	49
<b>7</b>	<b>Discussion</b>	<b>51</b>
7.1	Methodology . . . . .	51
7.1.1	Classification . . . . .	51
7.1.2	Landsat imagery retrieval . . . . .	54
7.2	Data . . . . .	55
7.2.1	Landsat data . . . . .	55
7.2.2	MAR surface mass balance . . . . .	56
7.2.3	Digital elevation model . . . . .	56
7.3	Results . . . . .	57
7.3.1	Equilibrium-line altitude (ELA) . . . . .	57
7.3.2	Accumulation area ratio (AAR) . . . . .	57
7.3.3	Surface mass balance (SMB) . . . . .	58
7.3.4	ELA, AAR, and SMB in relation to the climate . . . . .	58
7.3.5	AAR-SMB regression . . . . .	61
7.3.6	$AAR_0$ fluctuations . . . . .	63
7.3.7	Glacier area . . . . .	64
7.3.8	Length of hydrological year . . . . .	66
<b>8</b>	<b>Conclusion</b>	<b>67</b>
<b>9</b>	<b>Bibliography</b>	<b>71</b>

<b>A Data</b>	<b>81</b>
<b>B Scripts</b>	<b>87</b>

# List of Figures

3.1	Southern terminus of Mittivakkat glacier . . . . .	9
3.2	Mittivakkat glacier complex . . . . .	11
3.3	Temperature and precipitation in Tasiilaq and at Mittivakkat . . . . .	12
3.4	Temperature and precipitation anomalies . . . . .	14
3.5	AMO and NAO indices . . . . .	16
3.6	Glacier extent over time . . . . .	17
4.1	Position of MAR tiles . . . . .	19
5.1	Example AAR-SMB regression . . . . .	25
5.2	Area and volume adjustment of a glacier . . . . .	27
5.3	Methodology flowchart. . . . .	28
5.4	Number of retrieved Landsat scenes . . . . .	29
5.5	k1-Moore neighborhood . . . . .	31
6.1	ELA over time, including linear regression trend line and uncertainty envelope. . . . .	34
6.2	Mittivakkat glacier with low, mean, and high ELA contour lines . . . . .	35
6.3	Comparison of ELA time series including linear regression trend lines. . . . .	36
6.4	ELA time series correlation . . . . .	37
6.5	AAR over time, including linear regression trend line and uncertainty envelope. . . . .	37
6.6	Comparison of AAR time series including linear regression trend lines. . . . .	39
6.7	AAR time series correlation . . . . .	40
6.8	SMB over time, including linear regression trend line . . . . .	40
6.9	Comparison of SMB time series including linear regression trend lines . . . . .	42
6.10	SMB time series correlation . . . . .	43
6.11	Accumulation, ablation, at total glacier area over time. . . . .	43
6.12	Length of hydrological year over time, including linear regression trend line. . . . .	44
6.13	Scatterplot of SMB against length of the hydrological year. . . . .	45
6.14	Regression of SMB against AAR for original data. . . . .	46
6.15	Regression of SMB against AAR for WGMS data. . . . .	48
6.16	Time-average ELA and $AAR_0$ -ELA . . . . .	49
6.17	Comparison of AAR-SMB regression based on original data. . . . .	50
7.1	Comparison of true color image and corresponding classification . . . . .	52
7.2	AAR-SMB second-order polynomial regression for original data. . . . .	62

7.3	Fluctuations of AAR <sub>0</sub>	63
7.4	AAR-SMB regressions for the highest and lowest AAR <sub>0</sub>	65
7.5	AAR-SMB regressions for the highest and lowest AAR <sub>0</sub> (WGMS)	65
B.1	Flowchart overview of Google Earth Engine and Python scripts	88

# List of Tables

4.1	Landsat mission dates . . . . .	22
4.2	Landsat mission meta data . . . . .	23
5.1	Manually deleted Landsat scenes . . . . .	30
5.2	Reflectance threshold values. . . . .	31
7.1	Correlations between climate and ELA, AAR, and SMB . . . . .	60
7.2	Correlations between AMO and NAO, and ELA, AAR, and SMB . . . . .	60
A.1	Original data overview table. . . . .	82
A.2	WGMS data overview table. . . . .	83
A.3	Regression overview table (original data) . . . . .	83
A.4	Regression overview table (WGMS data) . . . . .	84
A.5	Regression overview table (other glacier metrics) . . . . .	84
A.6	Regression overview table (climate data) . . . . .	84
A.7	Correlations overview table . . . . .	85
A.8	Correlations overview table (climate data) . . . . .	85
A.9	Correlations between climate and ELA, AAR, and SMB . . . . .	85
A.10	Correlations between AMO and NAO, and ELA, AAR, and SMB . . . . .	86

# Introduction

## 1.1 Global glacier melt

Even if global warming is successfully limited to 1.5°C as targeted in the 2015 Paris Agreement, roughly half of all glaciers worldwide ( $49 \pm 9\%$ ) are projected to disappear before the end of the century (Rounce et al., 2023). Some regions, such as western Canada, central and northern Europe, and southeast Asia, could even lose between 60% and 100% of their glaciers depending on the warming scenario, with near-complete deglaciation expected at a temperature increase of 3°C (Rounce et al., 2023). This loss of glacier mass is thought to have grave humanitarian, environmental, and economic consequences, the most prominent and well-studied of them being the rise of global sea levels.

Between 2000 and 2019, glacier melt alone – here and below referring to both glaciers and ice caps – was responsible for  $21 \pm 3\%$  of sea level rise (Hugonnet et al., 2021). In this time frame, glaciers contributed between 0.70 and 0.78 mm of sea level equivalent (SLE) every year, with the annual rate expected to rise up to 2.5 mm by 2100 under the RCP 8.5 scenario (Hugonnet et al., 2021; Marzeion et al., 2020). Until the end of the century, the absolute sea level rise attributed to glaciers is projected to range from  $90 \pm 26$  mm for a warming of 1.5°C to  $154 \pm 44$  mm for a warming of 4°C (Rounce et al., 2023). With more than 600 million people living in coastal areas today (meaning within 10 m of current sea levels), any further sea level rise could potentially displace millions (Desmet et al., 2021; Hauer et al., 2020; Nicholls et al., 2011). As its impacts are felt worldwide, Desmet et al. (2021) expect sea level rise to result in a loss of 4.5% of the global GDP, underlining the importance of limiting sea level rise from an economic perspective as well.

In addition to the threat of rising sea levels, glaciers – together with snow sheets – play an important role as water storage in many regions along the Arctic and Pacific coastlines as well as in mountainous areas, such as Iceland and Patagonia where they serve as a water resource for ecosystems and human communities (Immerzeel et al., 2020). According to Immerzeel et al. (2020) around 1.9 billion people – roughly every fifth person on Earth – are currently depending to some extent on glaciers as a water supply, be it for irrigation, hydropower, mining, or agriculture (Huss et al., 2017). In their World Heritage Report, the United Nations Education, Scientific, and Cultural Organization (UNESCO) even states that glaciers serve as a vital water

resource for up to half of the world's population (UNESCO International Union for Conservation of Nature and Natural Resources, 2022).

Changing glacier melt rates in response to increased warming also alter the maximum and minimum flowrate amplitudes of melt water streams, changing erosion rates and leading to an increased risk of slope failures, landslides, and outburst floods (Huss et al., 2017). Altered erosion rates furthermore impact the nutrient fluxes and water quality of the melt water run-off, exerting stress on downstream ecosystems and ultimately leading to the disruption of local food webs and a loss of biodiversity (Gutiérrez et al., 2015; Jacobsen et al., 2012; Milner et al., 2017).

Apart from their environmental and economic significance, glaciers also play an important role as sacred places in the spiritual life of numerous cultures, such as the Quechua in the Peruvian Andes or the Sherpa in the Himalayas (Allison, 2015; UNESCO International Union for Conservation of Nature and Natural Resources, 2022). Already now, some communities had to change their cultural interactions with glaciers due to the increased mass loss. One example is the centuries old celebration of Qoyllur Rit'l (Quechua: *Qoyllur* = star, *Rit'l* = snow) that no longer involves the ceremonial cutting of ice blocks from the local glacier after the Quechua noticed the increasing melt rates (UNESCO International Union for Conservation of Nature and Natural Resources, 2022). Worldwide, the UNESCO has identified over 18,000 glaciers in 50 World Heritage Sites that are of notable cultural and/or scientific significance, such as the Te Wahipounamu site in southwest New Zealand or the Jakobshavn Isbræ glacier in the Ilulissat fjord in western Greenland (UNESCO International Union for Conservation of Nature and Natural Resources, 2022). Regardless of the climate change scenario, the glaciers in about a third of these Heritage Sites are projected to disappear by 2050, with up to half of all sites following the same fate by the end of the century, if emissions are not reduced (UNESCO International Union for Conservation of Nature and Natural Resources, 2022).

## 1.2 Glacier melt in Greenland

With temperatures in the Arctic rising two to three times faster than the global mean, the Greenlandic ice masses have been heavily impacted by climate change (Mernild et al., 2011; Rantanen et al., 2022). In the 1980s, the mass balance of the main ice sheet has first moved past the limits of its internal variability, experiencing a roughly sixfold increase of mass loss since then: from  $51 \pm 17$  Gt/y in 1980-1990 to  $286 \pm 20$  Gt/y in 2010-2018 (Mouginot et al., 2019). About half of the mass loss in Greenland is attributed to the glaciers peripheral to the main ice sheet, even though they only cover a small fraction of the total ice area – about 5% according to Kargel et al. (2012) and Rastner et al. (2012) (Mernild, Knudsen, et al., 2013). In fact, 12% of the global projected sea level rise until 2100 are expected to be contributed solely by these glaciers (Rounce et al., 2023).

Besides their contribution to global sea level rise, the melting of the peripheral glaciers has local consequences as well. First, the water discharging from these glaciers carries a large amount of sediment into the fjords and ocean which includes dissolved organic carbon and bioavailable iron, both of which are crucial from primary production in aquatic ecosystems (Bhatia et al., 2013; Musilova et al., 2017; Overeem et al., 2017). This nutrient-rich discharge plays an important role in making the Greenlandic fjords foraging hot spots for marine mammals and seabirds, and the loss of these glaciers – especially tide water glaciers – therefore threatens the existence of many local ecosystems (Lydersen et al., 2014).

The increasing melt water run-off is, however, not only affecting natural ecosystems, but also putting pressure on local human communities (Sugiyama et al., 2021). While Greenland is becoming a more and more popular tourist destination, many tourists state that their primary reason for coming to Greenland is to see the glaciers, before they melt away (Chow, 2019). But already now, glaciers are becoming more inaccessible and smaller, and glacier tourism more risky, with an increasing number of crevasses, landslides, and avalanches being reported (Wang & Overland, 2004). This development is beginning to threaten the livelihoods of those working in the tourism industry (Wang & Zhou, 2019). This is also true for Mittivakkat glacier: while the glacier used to be easily accessible from the shore, it has now retreated up into higher and rougher terrain and to access it, one must complete at least 45 minutes of demanding hiking without marked trails. Mittivakkat also used to be a convenient transport route used by dog sledders but has now become too inaccessible and crevassed to be safe (Ander Bjørk, personal communication, 13th of June 2024).

Apart from its role in Greenlandic tourism, glacier melt also poses a risk to the local infrastructure, with one example being the town of Qaanaaq in northwest Greenland, where a flooding of the outlet stream of the Qaanaaq glacier destroyed the road connection to the local airport in both 2015 and 2016 (Sugiyama et al., 2021). Moreover, multiple bridges in the town were destroyed by increased discharge in the glacial outlet stream, both due to intense melting and a heavy rain event in 2016 (Kondo et al., 2019). In addition to threatening the transport infrastructure, glaciers also play an important role in the power infrastructure with hydropower plants in Greenland often relying on melt water feeding into the reservoirs to generate electricity (Ellekrog, 2023). One example is the town of Tasiilaq located around 15km east of Mittivakkat glacier where a hydropower plant was opened in 2004 that mostly got its water supply from small glaciers located close to the reservoir (Ellekrog, 2023). As these glaciers were melting away, the resulting water shortage threatened the power supply of the town (Ellekrog, 2023). While a rerouting of melt water from Mittivakkat helped to temporarily mitigate the shortage, this is certainly no long-term solution, as Mittivakkat is also shrinking rapidly (Ellekrog, 2023; GEUS, 2018; Mernild et al., 2011).

Regarding the cultural significance of glaciers in the region, unfortunately not much has been published (Bjarne Grønnow, personal communication, 29th of June 2024). Still it can generally

be said that the glaciers and ice caps peripheral to the ice sheet are mainly seen as part of the border region between the human settlements along the coast and the strange and dangerous world of the main ice sheet (Grønnow, 2009). Serving both as access routes to hunting grounds in the summer and as the entrance to the main ice sheet filled with many of the dangerous creatures of the Greenlandic oral mythology (examples include the *qivittut* [human outcasts], the *tornit/tunit* [inland dwellers], or the *eqqillit* [dog people of the interior] which are particularly present in legends from eastern Greenland), glaciers evoke conflicting emotions and play a central role in the Greenlandic culture (Grønnow, 2009).

### 1.3 Objectives of the thesis

The projections of future melt from the glaciers peripheral to the Greenland ice sheet and the severe impacts their loss could have – and in fact already has – on human communities and natural ecosystems underscore the need to accurately quantify the expected mass loss of these glaciers. Their remote location, however, makes in-situ observations both logistically challenging and expensive as well as dangerous, resulting in very few glaciers having any mass balance records at all. Out of the roughly 20,000 glaciers in Greenland, only 20 have recorded mass balance observations, and only 5 of them have ongoing observational programs (Machguth et al., 2016; Mernild et al., 2018).

A methodology that allows for the quantification of the expected mass loss of the peripheral glaciers without the need for in-situ observations would therefore serve as a valuable addition to on-going glacier monitoring efforts in Greenland. For this purpose, a simple Python-based tool chain is developed that estimates the committed mass loss of a glacier based on Landsat satellite imagery and MAR climate reanalysis surface mass balance data.

In this study the committed mass loss is estimated for the Mittivakkat glacier in southeast Greenland, as it is the only glacier with a continuous, long-term time series (observations going back to the hydrological year 1995/96) that allows for a validation of the newly generated data against in-situ field observations (Mernild et al., 2011). This way, it can be evaluated whether the methodology presented in this study could be used to determine committed mass loss of the remaining peripheral glaciers. The produced tool chain should in theory be applicable to any land-terminating glacier.

### 1.4 Structure of the thesis

After this brief introduction to the significance of Greenland glacier melt on both the global and local scale, Chapter 2 provides a short definition of the most important glaciological and remote sensing-related terms used in this study. Then the study area is introduced in

Chapter 3, including an overview of the local topography, climate, scientific significance, and recent glaciological changes in response to the changing climate. Chapter 4 introduces the data used for the computation of the committed mass loss and Chapter 5 explains the applied methodology and workflow. The results of the analysis are presented in Chapter 6 and compared to existing observations. Chapter 7 discusses these results as well as the suitability of the used data and methodology for the purposes of the study, and Chapter 8 summarizes the main findings and gives an outlook towards possible improvements in the future.

# Glossary

## 2.1 Glaciology

**Hydrological year:** The hydrological year (also known as the budget year) of a glacier describes the time period of accumulation and subsequent ablation from one mass minimum to the next (Hagg, 2022). It begins with the first accumulation of mass at the end of the previous ablation season and ends with the next beginning accumulation season (Hagg, 2022). It is therefore defined by the date at which the ablation area reaches its maximum extent (Box et al., 2022). In the case of Mittivakkat glacier, the hydrological year usually begins and ends in August or September.

**Mass balance (MB):** The mass balance is a measure used to determine whether a glacier is gaining or losing mass and is typically expressed as height in water equivalent (w.eq.) (USGS, 2022a). The mass balance is often given as an average for the entire glacier at the end of its hydrological year, but can also be calculated for smaller areas, such as the accumulation or ablation area or only for a specific period, such as the ablation or accumulation season (USGS, 2022a). A positive mass balance indicates that the glacier is gaining mass, a negative balance indicates that it is losing mass.

**Surface mass balance (SMB):** The surface mass balance of a glacier describes its mass balance based on mass gain through precipitation and mass loss through evaporation and melt water run-off alone (NASA, 2024). It does specifically not include mass loss at the glacier margins through calving or thinning as is the case for marine-terminating glaciers (NASA, 2024). For land-terminating glaciers the surface mass balance and the mass balance are the same.

**Accumulation area:** The area of a glacier that has a positive net mass balance at the end of the hydrological year (Hagg, 2022).

**Ablation area:** The area of a glacier that has a negative net mass balance at the end of the hydrological year (Hagg, 2022).

**Transient snowline (TSL):** The TSL marks the transition line from snow cover to bare ice, superimposed ice, or firn on a glacier during the ablation season (Mernild, Pelto, et al., 2013).

At the TSL the mass balance is zero, provided the mass balance was not negative on any part of the glacier during the accumulation season (Mernild, Pelto, et al., 2013).

**Equilibrium-line altitude (ELA):** The ELA is defined as the TSL at the end of the ablation season during the maximum extent of the ablation area, marking the border between accumulation and ablation area (Mernild, Pelto, et al., 2013). Along this line the annual net mass balance is zero (Mernild, Pelto, et al., 2013).

**Accumulation area ratio (AAR):** The AAR is defined as the ratio between the extent of the accumulation area at the end of the melt season and the total glacier area (Mernild, Pelto, et al., 2013). Note that even though the AAR is technically defined as the lowest ratio between the accumulation area and total area, the term is often used for the general idea of the ratio between the two areas, not just the lowest ratio.

**Equilibrium AAR ( $AAR_0$ ):** The AAR that a glacier should have in order to be in dynamic equilibrium with the current climate (Box et al., 2022; Dyurgerov et al., 2009).

**Fractional imbalance ( $\alpha$ ):** The ratio between time-averaged AAR and  $AAR_0$  (Box et al., 2022). It serves as a measure of the imbalance of a glacier with the current climate and is directly proportional to the area change that a glacier must undergo to reach an equilibrium state with the climate (Box et al., 2022). Based on  $\alpha$ , one can also estimate the corresponding volume change of a glacier (Box et al., 2022).

## 2.2 Remote sensing

**Scene:** The term scene simply describes an image taken by a satellite.

**Collection 2:** A republication of the original Landsat Collection 1 archive that has undergone major reprocessing and data improvements, first and foremost an improved geometric accuracy (USGS, 2022b).

**Level-2:** Level-2 imagery describes reflectance and surface temperature imagery generated from raw Landsat imagery (USGS, 2024b). The raw data is filtered to only include scenes with a solar zenith angle below 76° that includes the auxiliary data needed to generate reliable surface reflectance and temperature images (USGS, 2024b).

**Tier 1:** A subset of Level-2 data that has been filtered to only include imagery that passes a threshold value of a horizontal accuracy root mean squared error (RMSE) of less than 12 meters (USGS, 2017). Tier 1 includes only the highest quality data (USGS, 2017).

# Study area

The Mittivakkat glacier complex is located on Ammassalik Island ( $65.68^{\circ}\text{N}$ ,  $37.8^{\circ}\text{W}$ ) in southeast Greenland in the low Arctic or – depending on the definition of Arctic – just south of its border (Machguth et al., 2016; Mernild et al., 2018).

It covers an area of  $26.2 \text{ km}^2$  and extends from around 180 to 880 meters above sea-level (m a.s.l.) (Machguth et al., 2016; Mernild et al., 2018). On average, the glacier ice is 97 meters thick, with larger values towards the center and smaller values at the margins (Mernild, Knudsen, et al., 2013). Based on the area and mean ice thickness in 2011, Mernild, Knudsen, et al. (2013) estimated the total glacier volume at  $2.6 \pm 0.4 \text{ km}^3$ . The mean ice flow velocity lies at 8 meters per year with maximum velocities of up to 22 meters per year towards the center and minimum velocities of 3.5 meters per year towards the glaciers margins, where the drag is strongest (Mernild, Knudsen, et al., 2013).

In this study only the main catchment of the Mittivakkat glacier complex as defined in the Randolph Glacier Inventory (see Chapter 4.3) with an area of  $20.15 \text{ km}^2$ , and an estimated volume<sup>1</sup> of  $1.95 \text{ km}^3$  is considered (Machguth et al., 2016; RGI Consortium, 2017). If not otherwise indicated, Mittivakkat glacier refers to the main catchment only for the remainder of this study (see Figure 3.2).

## 3.1 Surrounding topography

The area surrounding the glacier is characterized by a strong alpine relief with bare bedrock towards higher elevations, loose debris at lower elevations, and fluvial sediments in the pro-glacial valley (see Figure 3.1) (Mernild et al., 2006). The ice in the main catchment flows from east to west and drains into the 10-15 kilometer wide Sermilik fjord that separates the glacier from the ice sheet on the mainland, roughly 50 kilometers to the west (Ernstsen, 2013; Machguth et al., 2016; Mernild et al., 2006). With a surface area of more than  $1,100 \text{ km}^2$ , Sermilik fjord is the largest fjord system in southeast Greenland, draining an area of over  $58,000 \text{ km}^2$  (Mernild, Seidenkrantz, et al., 2012). The freshwater discharge of the fjord is

<sup>1</sup> Volume based on  $20.15 \text{ km}^2$  multiplied with mean ice thickness of 97 m as cited by Mernild, Knudsen, et al. (2013)



**Figure 3.1.:** Southern terminus of Mittivakkat glacier with melt water streams and loose glacier debris.  
Photo taken on July 12th, 2024 by Jasper Heuer.

thought to influence the strength of North Atlantic deep-water formation and consequently the overall strength of the Atlantic Meridional Overturning Circulation (AMOC) which has a strong influence on the local climate as further discussed in Chapter 3.3.3 (Mernild, Seidenkrantz, et al., 2012).

The entire Ammassalik region – which consists of Ammassalik Island and the area surrounding Sermilik fjord – includes hundreds of glaciers, both connected to and independent of the main ice sheet (Mernild, Malmros, et al., 2012). In their study, Mernild, Malmros, et al. (2012) found that the majority of both land- and marine-terminating glaciers have experienced a net retreat since the begin of their study period in 1972 with 5 glaciers having melted away completely since 1986.

## 3.2 Scientific research

The earliest scientific exploration of Mittivakkat glacier dates back to 1933, conducted by the Danish geologist Keld Milthers (Dansk Geologisk Forening, 1961). A little over two decades later, the glacier was selected as a focus point of future Danish Arctic research during the International Geophysical Year of 1957/58 and in 1970 a permanent research station (Sermilik Station) was established to serve as the base for scientific work in the area (IGN, 2013).

In the 1890s, the Danish Meteorological Institute (DMI) also installed a climate station in Tasiilaq, roughly 15 kilometers east of the glacier with 3 other climate stations being installed close to the glacier at a later point: one at a Nunatak along the glacier's northern margin at 515 m a.s.l., one close to the Sermilik research station by the coast at 25 m a.s.l., and one on the glacier itself at 440 m a.s.l. (Cappelen, 2021; Machguth et al., 2016; Mernild et al., 2008).

The position of the research station and the three climate stations at the glacier are shown in Figure 3.2.

Part of the ongoing research efforts at Mittivakkat includes a surface mass balance observation program that was established in 1995 and relies on a network of stakes (see Figure 3.2) to estimate mass changes (Knudsen & Hasholt, 2008; Machguth et al., 2016). The network covers an area of 16.3 km<sup>2</sup> (around 81% of the main catchment of the glacier) and consists of 44 individual stakes in three main cross-glacier lines about 500 meter apart from each other with most of the stakes located near the glacier tongue in the ablation zone to the west and fewer stakes in the accumulation zone at higher elevations towards the east (Machguth et al., 2016; Mernild et al., 2018). There are no stakes located on the southeastern part of the glacier as this area is heavily crevassed and therefore difficult to access, making assumptions about the surface mass balance in this area less certain (Knudsen & Hasholt, 2004; Mernild et al., 2011). The observed surface mass balance should, however, not be significantly biased by this omission as the area follows the same hypsometric distribution as the rest of the glacier and the stake network covers the entire elevation range (Mernild et al., 2018).

## 3.3 Climatology

### 3.3.1 Ammassalik region

The climate in the Ammassalik region is characterized by moderately cold winters, and cool, foggy, and moist summers with an annual mean temperature close to 0°C (Mernild et al., 2008). According to the Köppen-Geiger climate classification system, it lies within the Tundra climate zone (ET), defined as a region where the warmest month has a mean temperature above freezing, but of less than 10°C (Mernild et al., 2006; Wang & Overland, 2004). The primary wind direction is defined by the position of the low pressure systems in the North Atlantic that cause either predominantly easterly or northwesterly winds, depending on whether the region currently lies in front or behind the track of the low pressure system (Mernild et al., 2008). Easterly winds usually bring high precipitation to the eastern coast as moist air masses are pressed into the mountainous terrain of the island (Mernild et al., 2008). On the leeward side of these mountains, the winds generate corresponding warm foehn winds known as *neqqajaaq* (Mernild et al., 2008). The foehn winds resulting from cold air masses flowing down into the region from the ice sheet during northwesterly wind conditions are called *piteraq* and can become extremely strong and dangerous as they make their way through the narrow fjords and valleys (Mernild et al., 2008).

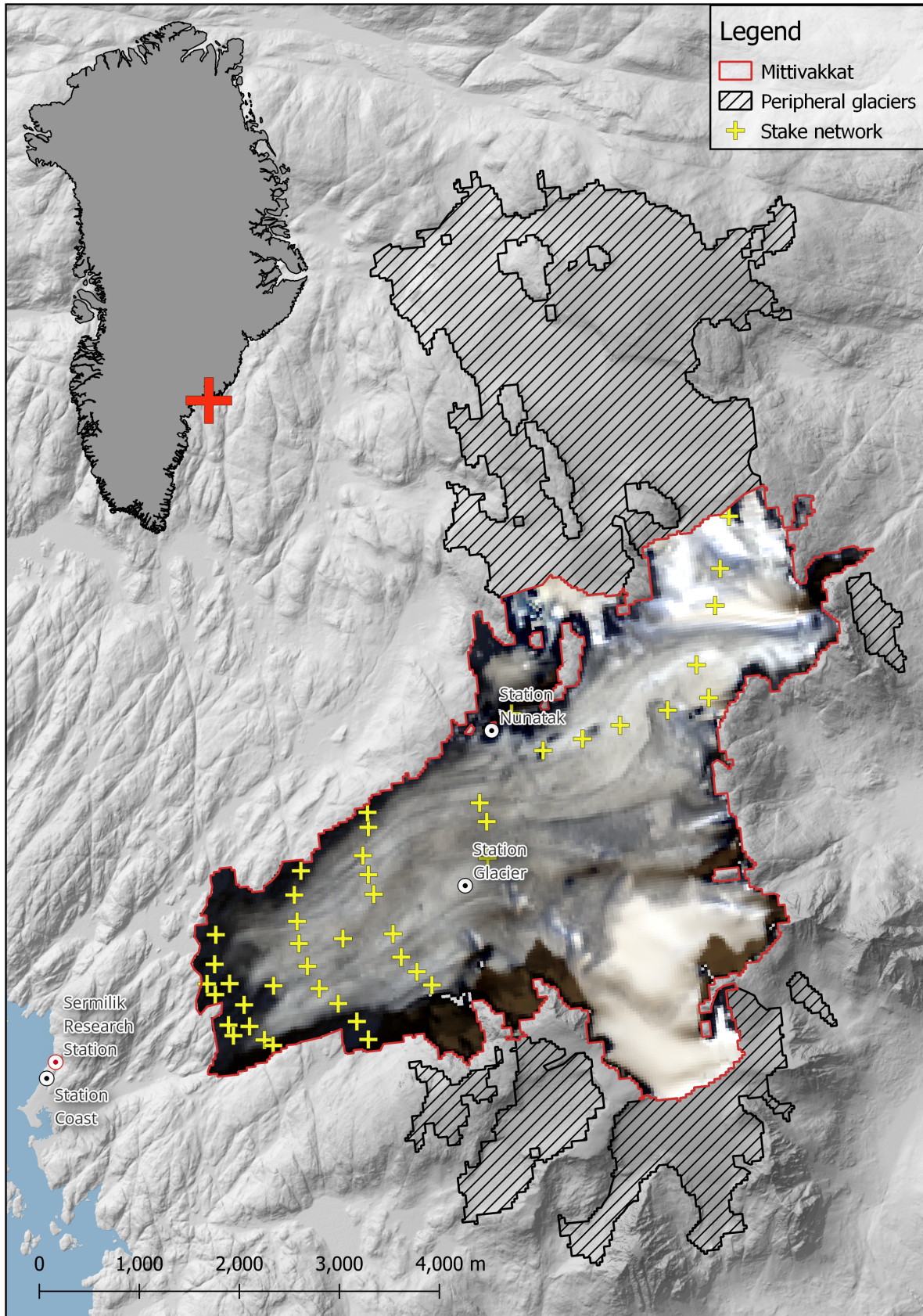


**Figure 3.2.:** Mittivakkat glacier complex with the main catchment outlined in red and filled with a Landsat 8 true color image from the 15th of September 2023. Inset map shows the position of Mittivakkat glacier in Greenland. Station Glacier = PROMICE MIT station.

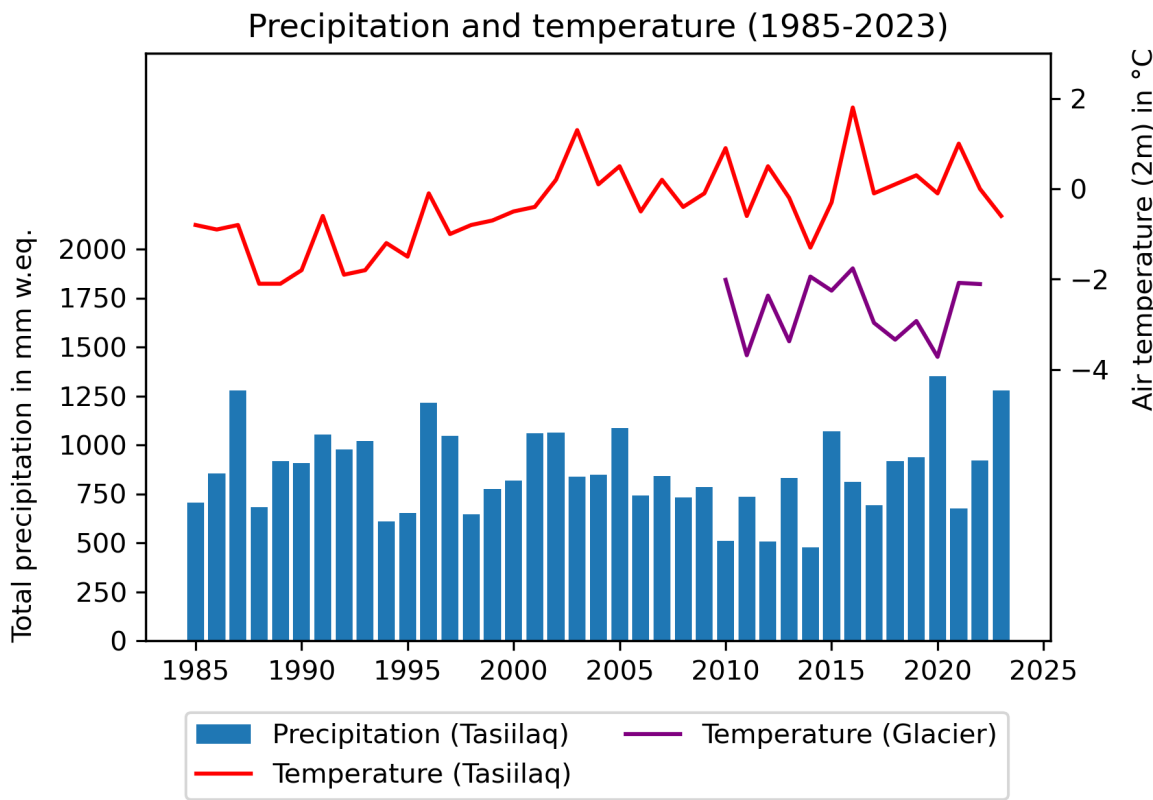


**Figure 3.3.:** Overview of temperature and precipitation over time at the DMI station in Tasiilaq and at station Glacier on Mittivakkat. Data source: DMI (2024) for DMI Tasiilaq, and How et al. (2022) for station Glacier.

### 3.3.2 Mittivakkat glacier

Unfortunately, both the climate stations Nunatak and Coast stopped recording reliable data in the early 2010s, making quantified climate data at Mittivakkat somewhat limited (Ander Bjørk, personal communication, 13th of June 2024)<sup>2</sup>. While the new climate station Glacier (official name: PROMICE MIT) has been set up in 2009, the data from this station reflects a different local climate and therefore cannot easily be used to fill the data gaps at station Nunatak (Fausto et al., 2020). In July 2024, another climate station was installed close to the original station Coast, picking up the climate recording again. Figure 3.3 above displays the temperature and precipitation data from both the DMI station in Tasiilaq and the station Glacier in the study period from 1985 to 2023.

The mean temperature at the DMI station in Tasiilaq lies at 0.15°C between 1985 and 2023, and at -2.66°C for the station Glacier between 2010 and 2022. (DMI, 2024; How et al., 2022). At the station Nunatak, Mernild et al. (2018) cite an average temperature of -2.1°C between 1993 and 2011 and average of 0.8°C at the station Coast for the same period.

<sup>2</sup> Earlier data from these two stations was unfortunately not available at the time of writing this study.

Over the course of the study period, the temperature at the DMI station in Tasiilaq displayed a highly significant positive trend of  $0.05^{\circ}\text{C}$  per year ( $R^2 = 0.387$ ,  $p\text{-value} < 0.001$ ), amounting to a total warming of  $1.95^{\circ}\text{C}$  since 1985. Mernild et al. (2008) cite a notably larger trend of  $0.12^{\circ}\text{C}$  per year for Tasiilaq between 1998 and 2006, but as this trend is based on fewer data points it might simply reflect a short-term fluctuation. At the station Glacier no significant temperature trend was detected which might, however, be due to the shorter available time series. For the station Coast Mernild et al. (2008) cite a trend of  $0.05^{\circ}\text{C}$  per year and a trend of  $0.10^{\circ}\text{C}$  for the station Nunatak between 1998 and 2006, respectively.

The Ammassalik region is one of the wettest regions in Greenland and so it is unsurprising that Mittivakkat glacier experiences a large amount of precipitation with a mean total annual precipitation of 1,851 mm w.eq. between 1999 and 2006 at the station Nunatak and 1,428 mm w.eq. at the station Coast (Mernild et al., 2008). The average in the main catchment area during this period lies at 1,549 mm w.eq., according to Mernild et al. (2008). In Tasiilaq, the mean total annual precipitation in the same period is considerably lower with just 903 mm w.eq. For the whole study period the mean annual total precipitation lies at 868 mm w.eq.

No significant precipitation trend could be detected at the DMI station in Tasiilaq, but on a long time scale from 1932 to 2006, Mernild et al. (2008) found a significant ( $p\text{-value} < 0.01$ ) positive trend in the Mittivakkat main catchment of a total of  $1.9$  mm w.eq. per year, amounting to a total precipitation increase of 148 mm w.eq. ( $R^2 = 0.09$ ). At the station Glacier, no precipitation data is available.

Looking at the long-term climate at the DMI station in Tasiilaq, it becomes apparent that the temperature and precipitation time series follow an anti-phase relationship, as illustrated in Figure 3.4 which shows the temperature and precipitation anomalies and their 10-year moving window averages between 1958 and 2023. While the raw time series show no significant correlation ( $p\text{-value } 0.513$ ), the correlation between the moving window average series is highly significant ( $p\text{-value} < 0.001$ ) with a Pearson correlation coefficient of -0.788, confirming the anti-phase relationship.

### 3.3.3 Climate and large-scale circulations

The climate in the Ammassalik region and at Mittivakkat glacier is predominantly influenced by the Icelandic low pressure system and the warm waters of the Irminger current flowing along the southeastern coast of Greenland (Hansche et al., 2023; Mernild, Seidenkrantz, et al., 2012). In the last 125 years, the region has experienced two cold periods from 1900 to the mid-1920s and from 1960 to the late-1990s with predominantly negative near surface air temperature anomalies (compared to the 1900-2008 baseline) as well as two warm periods

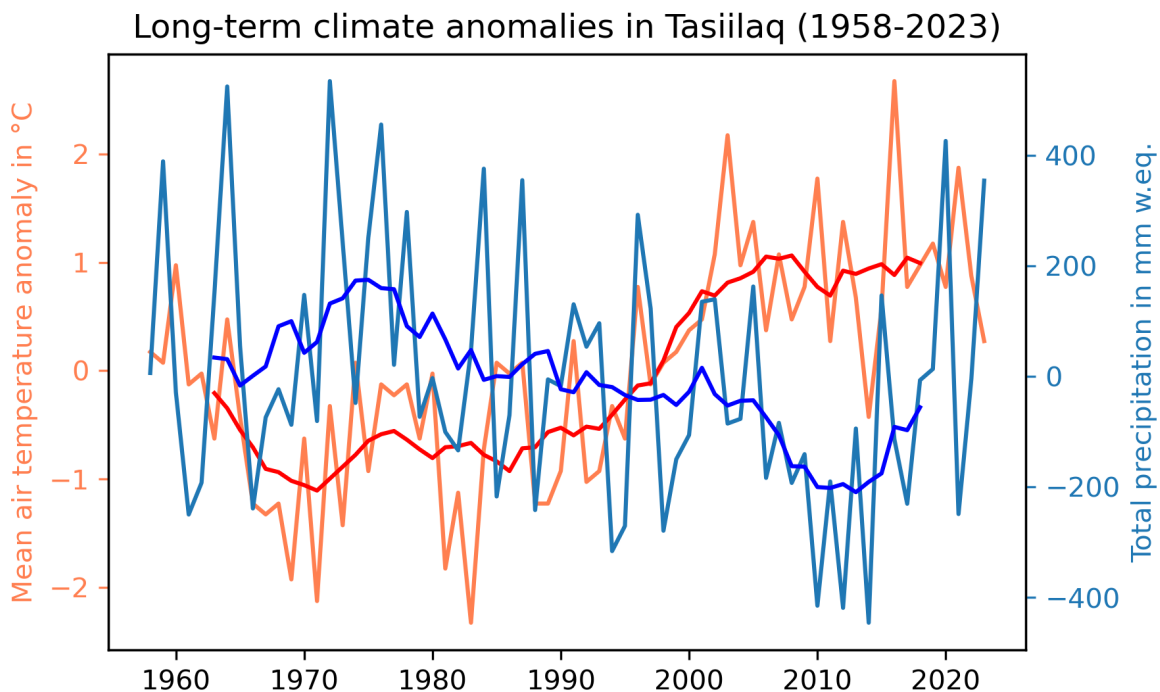


**Figure 3.4.:** Temperature and precipitation anomaly time series (compared to 1958-2023 baseline) with 10-year running mean in dark red (temperature) and dark blue (precipitation). Data source: DMI (2024).

from the mid-1920s to 1960 and from the late 1990s to the present with predominantly positive anomalies (Mernild, Seidenkrantz, et al., 2012).

As a study by Chylek et al. (2009) shows, this is not an isolated regional pattern, but rather a local reflection of the large-scale temperature fluctuations in the entire Arctic. These trends have also been observed on a global scale, but due to Arctic Amplification, they are much more pronounced in the Arctic (Chylek et al., 2009). Arctic Amplification describes the phenomenon that Arctic temperatures are rising at a rate twice or even three times faster than the global mean, with some recent studies citing rates of up to 4 times faster (Rantanen et al., 2022). Between 1910 and 1940, Chylek et al. (2009) even observed a 5.4-fold warming rate compared to the global mean temperatures and an even higher cooling rate between 1940 and 1970 of 9 to 13 times that of the global mean.

While the general cooling and warming trend could be explained by the buildup of atmospheric aerosols up to the 1970s and their subsequent decrease following stricter pollution guidelines and cleaner fuel sources, this would not explain why the temperature changes were up to one order of magnitude stronger in the Arctic than in the rest of the world (Chylek et al., 2009; Jiménez-de-la-Cuesta & Mauritsen, 2019). Chylek et al. (2009) suggest that changes in the Atlantic Meridional Overturning Circulation (AMOC) might be responsible: a cold anomaly of North Atlantic sea surface temperatures and the associated warm anomaly in the subtropics would increase the strength of the cooling trend in the Arctic, while simultaneously weakening

it at lower latitudes, increasing the difference between the rates of cooling. This hypothesis is supported by the strong correlation between the index of the Atlantic Multi-Decadal Oscillation (AMO) and panarctic temperatures, as well as the fact that the largest sea surface temperature changes associated with AMO fluctuations are observed in the North Atlantic (Chylek et al., 2009).

The AMO-related climate patterns also have a direct influence on the glaciers in southeast Greenland: during a negative phase of the AMO index, temperatures are generally lower with high precipitation (= circumstances that favor mass accumulation), while they are higher during a positive phase, when precipitation is lower (= circumstance that favor mass loss) (Mernild et al., 2018). While the correlation between the AMO index and the annual mean temperature at the station Glacier between 2010 and 2022 is not significant (*p-value*: 0.273), the correlation of annual mean DMI Tasiilaq temperatures with the AMO index between 1985 and 2023 is highly significant (*p-value* < 0.001) with a Pearson correlation coefficient of 0.635. This insignificance of the station Glacier correlation might therefore just be due to the low number of data points as the same correlation is highly significant (*p-value* < 0.001) at the monthly scale with a Pearson correlation coefficient of 0.377, supporting the connection between AMO and glacier temperatures cited by Mernild et al. (2018).

No significant correlation was found between the precipitation in Tasiilaq and the AMO index between 1985 and 2023, but on the longer time scale from 1958 to 2023, the correlation is significant (*p-value* < 0.01) with a Pearson correlation coefficient of -0.334, again confirming the relationship cited by Mernild et al. (2018). A comparison of the index of the AMO shown in Figure 3.5 below with the temperature and precipitation time series in Figure 3.4 illustrates the in-phase relationship between the AMO and temperature and the anti-phase relationship between the AMO and precipitation.

At the scale of intra-annual temperature variations, changes in the flow pattern of regional weather systems quantified by the North Atlantic Oscillation (NAO) index are also playing an important role according to Mernild, Seidenkrantz, et al. (2012). This is confirmed by the highly significant correlation (*p-value* < 0.001) between monthly temperatures at station Glacier and the NAO index between 2010 and 2022 with a Pearson correlation coefficient of -0.268, and the significant (*p-value* < 0.01) correlation between monthly DMI temperatures and the NAO between 1985 and 2023 with a Pearson correlation coefficient of -0.393. Neither of these correlations is significant at the annual scale.

There was no significant correlation found between the NAO and DMI precipitation on any time scale, neither for the raw data, nor the 10-year moving average time series.

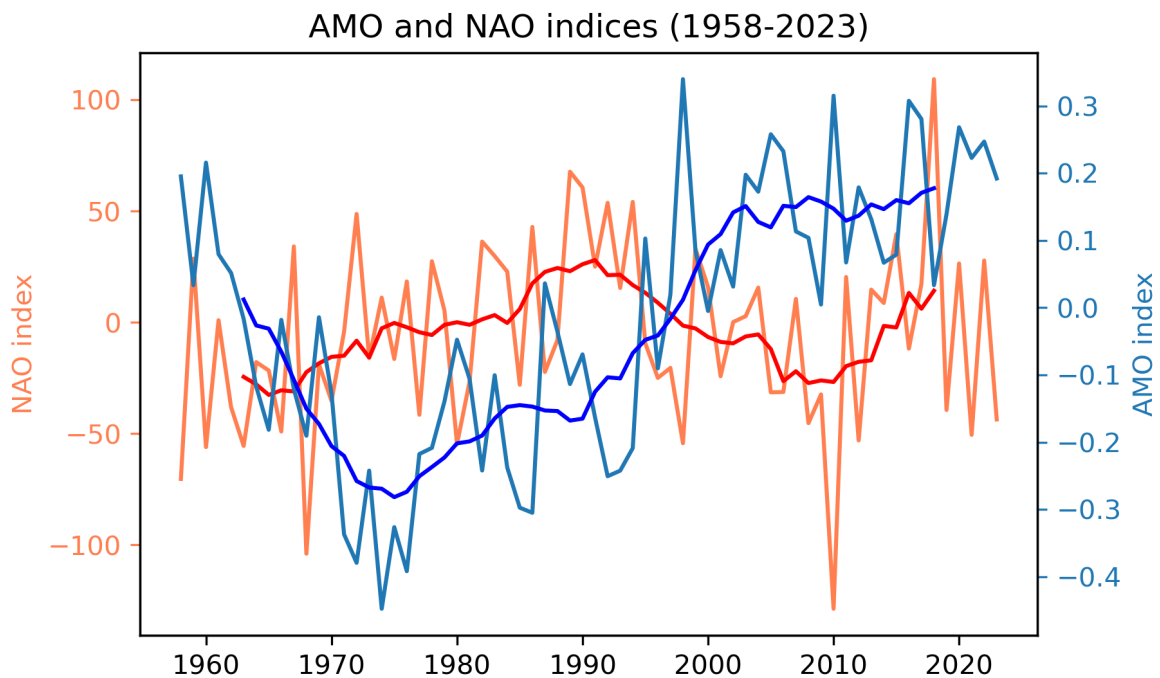


**Figure 3.5.:** AMO and NAO index time series with 10-year running mean in dark red (NAO) and dark blue (AMO). Data source: NOAA (2023, 2024).

### 3.4 Recent changes at Mittivakkat

Like many other glaciers in southeast Greenland, Mittivakkat is thought to have reached its maximum extent towards the end of the Little Ice Age (LIA) in the mid to late 19th century, and since then has been subject to nearly continuous retreat as illustrated in Figure 3.6 (Knudsen & Hasholt, 2008; Mernild et al., 2018). However, as the rate of retreat is influenced not only by the climate but also the local topography and internal glacier dynamics, it does not immediately correspond to the changes in the climatology (Mernild et al., 2011). The maximum retreat rate of 24 meters per year was for instance observed between 1943 and 1972 – a period of panarctic cooling according to Chylek et al. (2009) – and likely was a delayed response to a warm period between 1931 and 1943 (Mernild et al., 2011). In total, the glacier terminus is thought to have retreated by around 1,600 meters since the end of the LIA (Mernild et al., 2011).

Between 1986 and 2011, the mean ice thickness of Mittivakkat has reduced by 15% from  $115 \pm 17$  meters estimated by Knudsen and Hasholt (1999) to  $97 \pm 15$  meters, while area and volume shrank by 30% (from  $31.6 \text{ km}^2$  to  $26.2 \text{ km}^2$ ) and 18% (from  $3.7 \pm 0.5 \text{ km}^3$  to  $2.6 \pm 0.4 \text{ km}^3$ ) respectively (Mernild, Knudsen, et al., 2013; Mernild et al., 2018). Other glaciers in the region are following similar trends, with the average total area loss in the Ammassalik region estimated at  $27 \pm 24\%$  (translating to around 1% per year) in the same time frame (Mernild, Malmros, et al., 2012). The surface mass balance resulted in an elevation decrease of  $37.5 \pm 3.8$  meters in the lower parts of the glacier and  $7.8 \pm 0.8$  meters in the upper parts (Mernild,

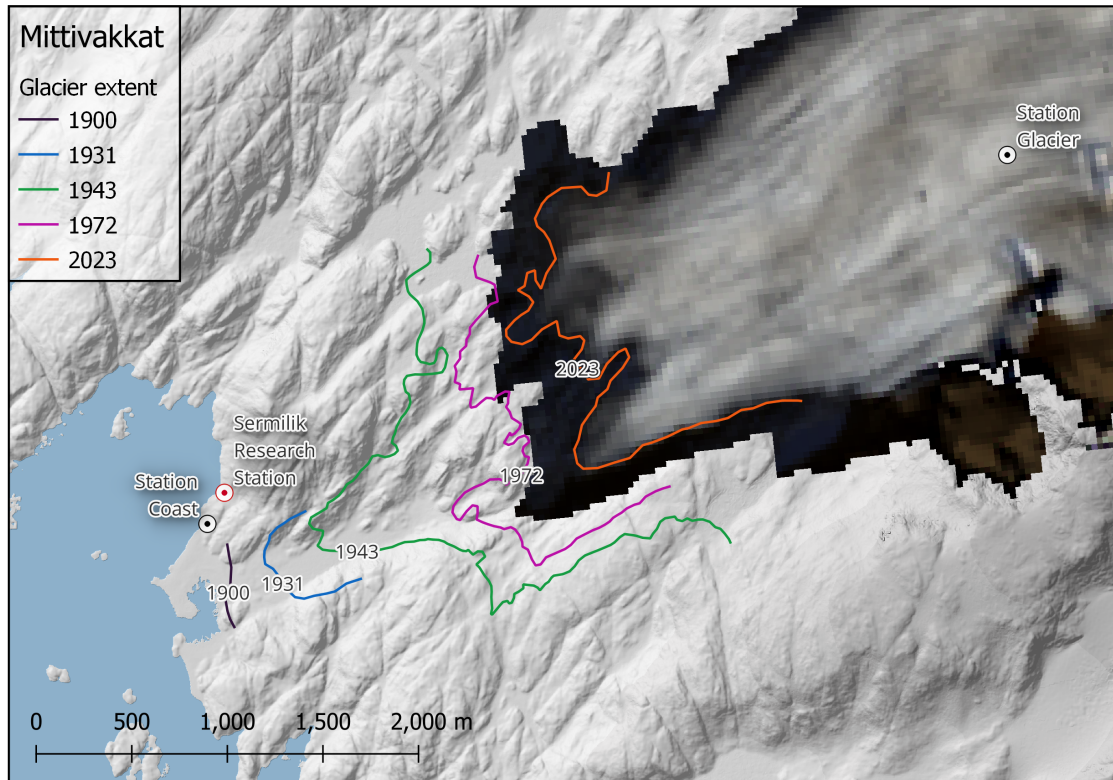


**Figure 3.6.:** Glacier extent over time. The 2023 terminus is based on the reclassification of the Landsat 8 image in Figure 3.2, the remaining terminus lines are taken from Mernild et al. (2011). Maximum extent (LIA corresponding to 1900 terminus) is estimated based on the remains of its age-dated terminal moraine (Anders Bjørk, personal communication, July 12th, 2024). Station Glacier = PROMICE MIT station.

Knudsen, et al., 2013). Vertical strain, however, has compensated for around 50% of these changes, with higher compensation at lower elevations (roughly 60%) and lower compensation at higher elevations (roughly 25%) (Mernild, Knudsen, et al., 2013). In response to the mass loss, basal sliding and ice deformation have reduced, resulting in the annual mean ice velocity dropping by an estimated 30% between 1996 and 2011 (Cuffey & Paterson, 2010; Mernild, Knudsen, et al., 2013). Towards the glacier terminus, where the thinning is most pronounced, the velocity decreased by up to 0.6 meters per year<sup>2</sup> or more than 50% since 1996 (Mernild, Knudsen, et al., 2013). Between 1986 and 2011 the surface slope increased from 5.4% to 5.9%, another indicator of increasing mass loss (Mernild et al., 2018).

Since the mass balance observation program began in 1995/96, the ELA has risen by over 500 meters in 2017 from 350 m a.s.l. to 880 m a.s.l. (Mernild et al., 2018). The mean ELA between 1995 and 2017 is 750 m a.s.l. (Mernild et al., 2018). This ELA rise translates to a decrease of the AAR, with an AAR average of 0.15 up to 2010 and multiple years with glacier-wide ablation (Mernild et al., 2011). Based on its imbalance with the current climate, Mernild et al. (2011) estimated that Mittivakkat glacier will lose about  $75 \pm 8\%$  of its area and  $85 \pm 7\%$  of its volume, even in the absence of any future warming.

# Data

## 4.1 Digital elevation model (DEM)

The elevation data used to determine the ELA comes from the ArcticDEM dataset version 4.1 by Porter et al. (2023). The ArcticDEM is a digital elevation model covering the entire Arctic at a spatial resolution of 2 meters (Porter et al., 2023). It is constructed from a large number of individual digital elevation and surface models computed from high-resolution satellite imagery acquired between 2007 and 2022 (Porter et al., 2023). The elevation for any given pixel is set as the median of all elevation values available for that pixel (Porter et al., 2023).

The DEM is provided by the Polar Geospatial Center of the University of Minnesota and accessed through the ArcticDEM Explorer website at <https://arcticdem.apps.pgc.umn.edu/> (University of Minnesota, 2024). The two mosaics used in this study are 14\_44\_1\_1\_2m\_v4.1 and 14\_44\_2\_1\_2m\_v4.1.

## 4.2 Modèle Atmosphérique Régional (MAR)

The surface mass balance data comes from the regional climate model (RCM) Modèle Atmosphérique Régional (MAR) that was first developed by Fettweis et al. (2005) in order to estimate the surface mass balance of the Greenland ice sheet in the years 1990 and 1991. It was originally forced at its boundaries by the ERA-40 climate reanalysis at intervals of 6 hours, and had a horizontal resolution of 25 kilometers (Fettweis et al., 2005; The National Science Foundation, 2022).

In this study an updated version of the model (version 3.14) is used, specifically the surface mass balance product at a daily resolution from and including 1984 until the end of 2023. The version 3.14 is forced by the more recent climate reanalysis ERA5 and has an improved horizontal resolution of 5 kilometers (see Figure 4.1). The data was accessed from the FTP server of the Laboratoire de Climatologie of Liège Université at <ftp://ftp.climato.be/fettweis/tmp/xiaoli/>.

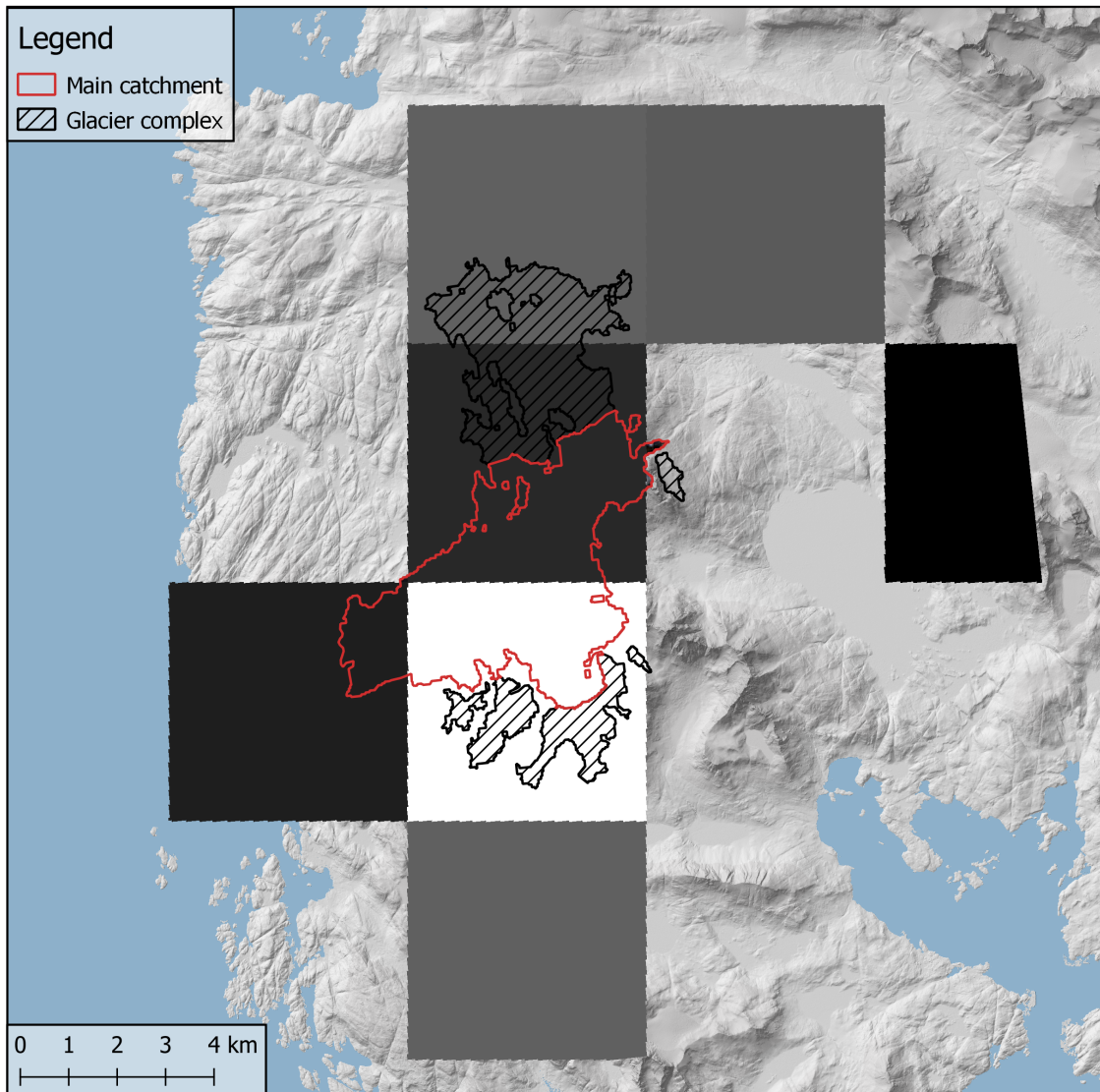


**Figure 4.1.:** Position of MAR tiles over the study area as a reference for the size of the MAR tiles and a visualization of the two small areas with no SMB data at the east and northwest margins of the main catchment. The color of the tiles corresponds to their respective mass balance.

MAR was chosen above other available climate models because it has been shown to perform particularly well over the Greenland ice sheet in a surface mass balance model intercomparison study by Fettweis et al. (2020). The model is fully coupled to a one-dimensional surface-atmosphere energy and mass transfer scheme known as SISVAT (Soil Ice Snow Vegetation Atmosphere Transfer) and its multi-layered snowpack model CROCUS is among other things able to account for melt water production and refreeze, as well as albedo changes due to changing snow qualities such as grain size and form (Brun et al., 1992; The National Science Foundation, 2022). This makes it especially well-suited for the analysis of ice- and snow-covered regions (The National Science Foundation, 2022).

## 4.3 Randolph Glacier Inventory (RGI)

The outline of Mittivakkat glacier that defines the study area comes from the version 6 of the Randolph Glacier Inventory, a database of glacier outlines published by the National Snow and Ice Data Center of the University of Colorado (RGI Consortium, 2017). The outline is based on the 2002 extent of the glacier, but still encompasses the maximum extent of the glacier in the earlier years of the time period investigated in this study (RGI Consortium, 2017). A small number of pixels at the glacier tongue and at the northern edge are cut off, but this loss of data was deemed negligible.

Note that RGI Consortium released the updated version 7 of the glacier inventory in 2023, but as the outline of Mittivakkat glacier is the same in both versions, version 6 was still used (RGI Consortium, 2017).

## 4.4 WGMS Fluctuations of Glaciers (FoG)

The Fluctuations of Glaciers data set is a data set of standardized glacier changes based on remote sensing data and in-situ field observations that it published annually by the World Glacier Monitoring Service (WGMS) (WGMS, 2024). Observations of ELA, AAR, and SMB from 1996 to 2023 from the newest FoG version 2024-1 serve as a base against which to compare the results of this study (WGMS, 2024).

The data for Mittivakkat has been contributed by different researchers, starting with stake measurements by Knudsen and Hasholt (2008) between 1996 and 2006 and Mernild et al. (2011) between 2007 and 2010. From 2011 to 2013, the data is contributed by Machguth et al. (2016) who state having received the data from an unpublished report by Mernild, but do not give details about the observation methodology – presumably these measurements come from the same stake network as previous years. For the years 2014 and 2015 the data comes from the Global Glacier Change Bulletin No. 2, where again no details on the observation methodology are given (WGMS, 2017). Finally, between 2016 and 2023, no data sources are cited in the data base as of the time of writing of this study. Still, it can be assumed that all data comes from the same stake network and methodology.

## 4.5 Landsat imagery

In this study, Landsat satellite imagery is used to classify the surface of Mittivakkat glacier into accumulation and ablation area to estimate the ELA and AAR at the end of each melt season. Landsat imagery was chosen over that of other available Earth-observation satellites

such as those of the Sentinel-2 or Planet programs due to its long temporal range despite the other programs offering higher spatial and temporal resolution data (Käab et al., 2016; Planet, 2024c). Obviously, a combination of multiple satellite imagery sources allow for an increase of the temporal resolution while still keeping the long period of observations of the Landsat archives. Due to the increased complexity of the classification methodology that would follow from this, however, this was deemed to lie outside the scope of this study. The matter is further discussed in chapter 7.2.1.

#### 4.5.1 The Landsat program

The Landsat program is an Earth-observation program initiated and managed by the U.S. Geological Survey (USGS) and the National Aeronautics and Space Administration (NASA) (USGS, 2023). It began in 1972 with the launch of Landsat 1, making it the longest on-going program for the collection of satellite imagery for Earth-observation (USGS, 2023).

The first satellite to capture images at a spatial resolution of 30 meters (= the spatial resolution of the subsequent Landsat missions 5 to 9, and therefore also the spatial resolution used in this study) was Landsat 4 launched in 1982 (NASA, 2021b). In addition to the Multispectral Scanner (MSS) that was already used in the Landsat missions 1-3, Landsat 4 carried the new Thematic Mapper (TM), the first sensor to capture surface reflectance in the blue section of the visible light spectrum (NASA, 2021a). As this wavelength section is used to classify the glacier surface in this study, Landsat 4 imagery would have been suited for the purposes of this thesis both in terms of spatial as well as spectral resolution. However, no images of the study area were available, therefore, this study only uses imagery from the Landsat missions 5 to 9.

The Landsat satellites 5 to 9 all orbit the Earth at an altitude of 705 kilometers in a (near-)polar, sun-synchronous orbit with an inclination of 98.2° (NASA, 2021b, 2021c, 2021e, 2021f, 2021i). Travelling at a speed of over 26,900 kilometers per hour, they orbit the planet in 99 minutes, passing over the equator 14.5 times a day, each time at 10:00 ( $\pm$  15 minutes) local time (NASA, 2021b, 2021c, 2021e, 2021f, 2021i). The orbits of Landsat 7 and Landsat 8 were exactly 8 days out of phase, lowering the combined revisit time (meaning the amount of time passed between two observations of the same place on Earth) from 16 to 8 days starting in 2013 (NASA, 2021i). Since the decommission of Landsat 7, Landsat 9 has taken over its place in orbit and is keeping up the improved temporal resolution (NASA, 2021i).

The Tables 4.1 and 4.2 below show the temporal range of each used satellite as well as some key meta data about the missions.

**Table 4.1.:** Landsat mission data availability according to the U.S. Geological Survey and the temporal range that was used for the analyses in this study (USGS, 2024c).

Mission	Date range	Used date range
Landsat 5	March 1984 - May 2012	1985 - 1998
Landsat 6		<i>Failed at launch</i>
Landsat 7	July 1999 - April 2022	1999 - 2013
Landsat 8	April 2013 - present	2013 - 2023
Landsat 9	October 2021 - present	2021 - 2023

#### 4.5.2 Caveats and limitations

Generally, surface reflectance data is not calculated for Landsat scenes with a solar zenith angle greater than 76°, as low sun angles result in more scattering due to the longer distance that the light travels through the atmosphere, dramatically increasing the degree of uncertainty of the reflectance measurements (Sayler, 2021, 2024). Therefore, the USGS warns of larger uncertainties associated with reflectance retrievals at high latitudes above 65° which includes Mittivakkat glacier (Sayler, 2021, 2024). Moreover, surface reflectance retrievals are complicated in the presence of ice and snow, due to their high reflectivity, further impacting the quality of satellite imagery in the study area (Sayler, 2021, 2024).

In the May of 2003, the ETM+ sensor onboard the Landsat 7 satellite suffered the failure of its scan line corrector component, resulting in long strips of missing data across all subsequently captured scenes (NASA, 2021e). The width of these strips depends on whether they lie close to the center of the scene (resulting in narrow strips) or at the far edge (resulting in wide strips) (NASA, 2021e). Depending on the relative amount of no data pixels in each scene, a large number of Landsat 7 images is not suited for further analysis, reducing the overall availability of data, especially for a few months in 2012/13, when Landsat 5 was already decommissioned and Landsat 8 not yet launched (NASA, 2021c, 2021f; USGS, 2024c).

#### 4.5.3 Cloud masking

As part of the pre-processing of Landsat imagery, cloudy pixels are masked using the CFMask algorithm (version 3.3.1) (Sayler, 2021, 2024; USGS, 2022a). This algorithm uses decision trees to calculate a so-called cloud score for each pixel that serves as a measure of likelihood of the pixel being cloudy (Foga et al., 2017). In this analysis, only pixels with a high confidence in cloudiness – meaning pixels with a value above 22.5 for the dimensionless cloud score – were counted as cloudy pixels (Foga et al., 2017).

**Table 4.2.:** Overview of Landsat mission meta data. Sources: NASA (2021a, 2021c, 2021d, 2021e, 2021f, 2021g, 2021h, 2021i, 2021j).

Mission	Sensor	No. of bands	Spatial resolution	Revisit time
Landsat 5	Thematic Mapper (TM)	7	30m (bands 1-5, 7) 120m (band 6)	16 days
Landsat 7	Enhanced Thematic Mapper Plus (ETM+)	8	30m (bands 1-5, 7) 60m (band 6) 15m (band 8)	16 days
Landsat 8	Operational Land Imager (OLI)	11	30m (bands 1-7, 9) 15m (band 8) 100m (band 10, 11)	16 days
Landsat 9	Operational Land Imager-2 (OLI-2)	11	30m (bands 1-7, 9) 15m (band 8) 100m (band 10, 11)	16 days

Like many other cloud masking algorithms, the CFMask algorithm struggles to correctly identify clouds over bright surfaces such as ice or snow, generally reducing the confidence in the cloud masking over glaciers and ice caps in comparison to other regions (Foga et al., 2017; USGS, 2022a). Still, this algorithm was chosen both due to its high performance compared to other cloud detection algorithms (see comparison study by Foga et al. (2017)) and because it is conveniently accessible in Google Earth Engine and does not require any additional computation. It should be noted that Google Earth Engine also offers an internal cloud masking algorithm for Landsat imagery called *simpleCloudScore* that is easier to implement, but less reliable as it is mostly meant to compare relative cloud likelihood between imagery from two different dates (Google Earth Engine, 2023). Therefore, this approach was not used.

#### 4.5.4 Data sets and access

For this study, atmospherically corrected surface reflectance (SR) Level-2 imagery from the Landsat Collection 2, Tier 1 was used, specifically the blue bands of the respective sensors, each measuring the reflectance in the wavelength spectrum between  $0.45\mu\text{m}$  and  $0.515\mu\text{m}$  (Sayler, 2021, 2024). All Landsat imagery was accessed through Google Earth Engine (Gorelick et al., 2017).

# Methodology

## 5.1 Background

In their book *Glaciers and the changing Earth system – a 2004 snapshot*, Dyurgerov and Meier (2005) describe how the mass balance of a glacier is related to its accumulation area ratio (AAR) and in turn to its equilibrium-line altitude (ELA). As mass balance can generally be thought of as a function of elevation – glaciers tend to accumulate mass at higher elevations and lose mass at lower elevations – the lower the ELA, the larger the AAR and the more likely that the glacier is gaining mass and advancing (Bahr et al., 2009; Dyurgerov et al., 2009). Inversely, the higher the ELA, the smaller the AAR, and the more likely that the glacier is losing mass and retreating (Dyurgerov et al., 2009). It becomes apparent that there must be a certain AAR value at which the glacier is in dynamic equilibrium with the climate, meaning that - accounting for the internal variability of the system - it is on average neither gaining nor losing mass. This AAR value, at which the total glacier mass balance is equal to zero is known as  $AAR_0$  (Dyurgerov et al., 2009). Its exact value depends on many factors, such as glacier shape, topography, and local climate, but is generally expected to lie between 0.4 and 0.8, with the majority of glaciers having an  $AAR_0$  of 0.5 to 0.6 (Bahr et al., 2009; Dyurgerov et al., 2009).

The  $AAR_0$  of a glacier can be determined by regressing the annual AAR values against the mass balance of the respective hydrological years and then calculating the AAR value at which the mass balance is zero as illustrated in Figure 5.1 (Dyurgerov et al., 2009). For the majority of the glaciers investigated in a study by Dyurgerov et al. (2009), the relationship between AAR and mass balance was linear, but there were a few exceptions where a higher-order polynomial regression fit the data best, with both concave-up and concave-down being represented. Dyurgerov et al. (2009) suggest that anomalous increases or decreases in the snow accumulation or a high sensitivity of the mass balance to changes in the precipitation regime could serve as explanations for the unusual AAR-mass balance relationships of these glaciers. When regressing AAR against mass balance, it should be noted, that the physical relationship between the two variables does not necessarily hold true for instances where the AAR is either 1 or 0, as accumulation and ablation could theoretically increase further without any subsequent changes in the AAR, distorting the AAR-mass balance relationship (Dyurgerov et al., 2009). Therefore, these data points should not be included in the AAR-mass balance regression. For small glaciers such as Mittivakkat, where the ELA has reportedly risen above the

### Example AAR-SMB regression

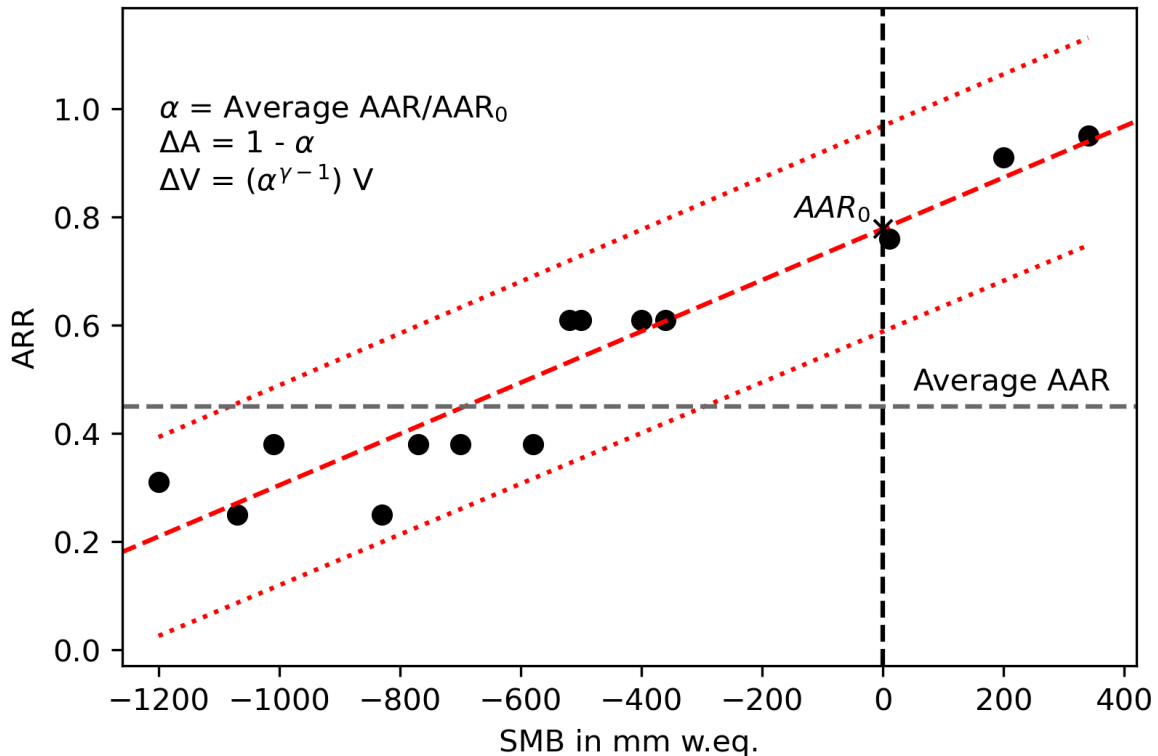


**Figure 5.1.:** Example AAR-SMB regression illustrating the concept of how the  $AAR_0$  is calculated.

maximum height of the glacier multiple times, this is a serious limitation of the methodology, especially if there is little data available to begin with (Dyurgerov et al., 2009).

By comparing the  $AAR_0$  to the time-averaged AAR of a glacier, one can determine whether a glacier is in or out of balance with the current climate, meaning whether it is mostly stable or whether it will likely gain or lose mass in the future. The period over which the AAR is averaged should include enough years to eliminate the effects of interannual variability but be short enough to not reflect the glacier adjusting to the changing climate yet (Bahr et al., 2009). The exact time scale at which glaciers adjust to the climate depends on the glacier at hand, but are generally thought to happen on the time scale of decades to millennia (Bahr et al., 2009). If the ratio between the time-averaged AAR and the  $AAR_0$  (known as the fractional imbalance  $\alpha$ ) is smaller than 1, the glacier is projected to lose mass, if it is larger than 1, it is projected to gain mass (Box et al., 2022; Dyurgerov et al., 2009). Conveniently,  $\alpha$  then also reveals the relative amount of area change needed for the glacier to equilibrate its shape to the current climate: the relative area loss is given as  $1 - \alpha$ , so an  $\alpha$  of 0.25 would indicate a 75% area loss and an  $\alpha$  of 1.25 a 25% area increase (Bahr et al., 2009; Box et al., 2022). The corresponding volume change can be estimated through a power law relationship between area and volume based on glaciological scaling theory given by Bahr et al. (2015) as:

$$\Delta V = (\alpha^{\gamma-1}) V$$

where  $V$  = glacier volume,  $\Delta V$  = volume change,  $\alpha$  = fractional imbalance, and  $\gamma$  = a power law scaling exponent that is dependent on whether the formula is used to calculate the mass loss of a single glacier or an ice cap.

According to Bahr et al. (2015) the scaling exponent  $\gamma$  should be set to a value of 1.35 for glaciers. They do, however, stress that volume-area scaling should be applied to a collection of glaciers and is not meant to be used for individual glaciers on their own (Bahr et al., 2015). If used on only one glacier, the resulting volume change should be treated as an order of magnitude estimate (Bahr et al., 2015).

The foreshadowing of glacier mass changes is possible, due to the fact that the AAR and mass balance adjust to a changing climate at a speed about an order of magnitude faster than the actual ice mass, meaning that a shrinking or growing accumulation area serves as an indication of actual mass loss or gain in the future (Bahr et al., 2009; Box et al., 2022). Only when the average AAR and the  $AAR_0$  are equal, is the glacier in dynamic equilibrium with the climate again(Bahr et al., 2009). This is illustrated further in Figure 5.2.

Overall, this method does not give a time scale at which glacier mass changes are expected to happen, it merely establishes a lower bound for the committed mass change based on the current climate, meaning that any projected glacier mass loss or gain would happen, even if the climate were to remain stable (Box et al., 2022). However, based on an ice sheet model study by Aschwanden et al. (2019), Box et al. (2022) hypothesize that in the case of the Greenlandic ice sheet and peripheral ice caps and glaciers, the majority of the committed mass loss might occur within the next 200 years.

As the climate continues to change, so change the committed mass losses and gains. Sustained warming of the Arctic would therefore further increase the committed mass loss of the local glaciers and only a cooling of the climate could reduce it again.

## 5.2 Workflow

An overview of the entire workflow is given in the flowchart diagram in Figure 5.3 below. The individual steps are explained in detail in the following chapters. The scripts used for the analysis as well as a second flowchart explaining the order in which they are to be executed can be found in Appendix B.

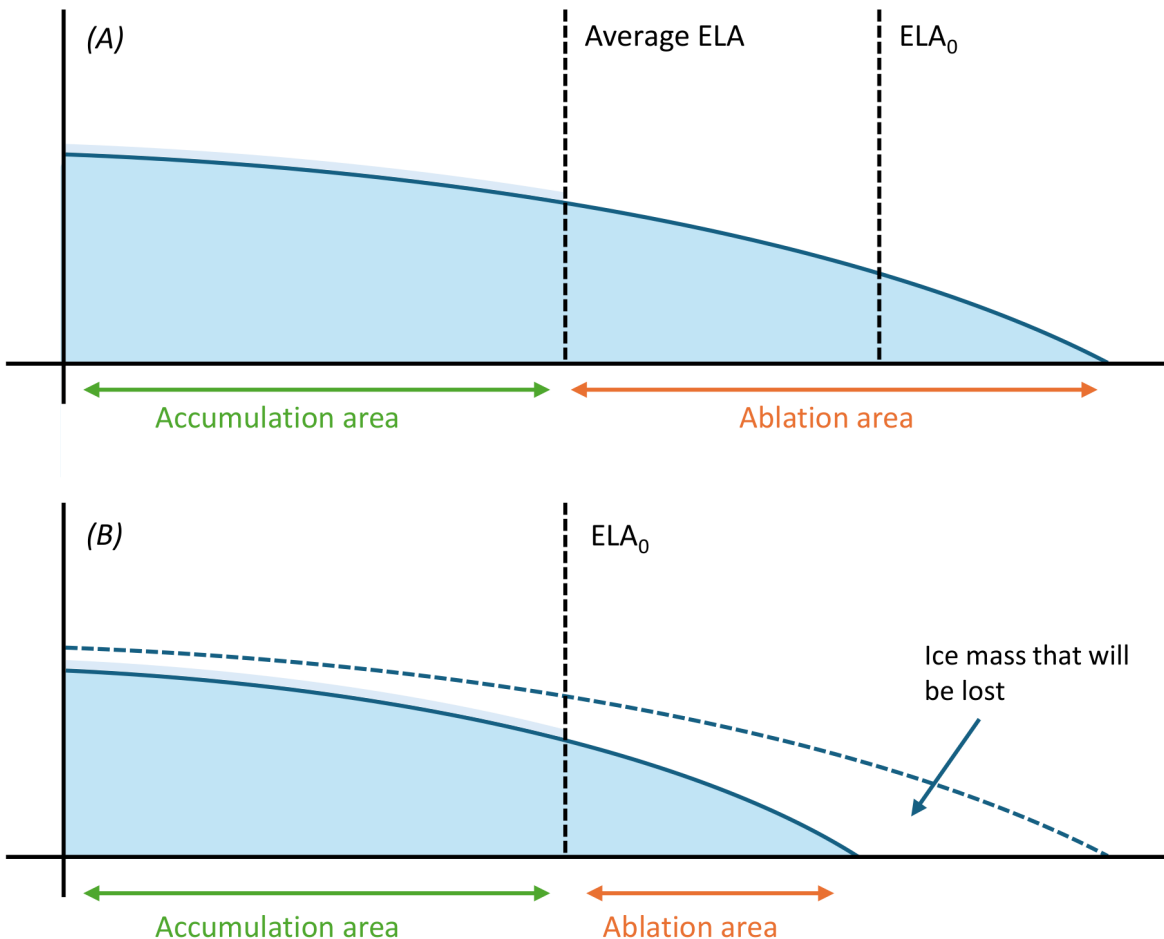


**Figure 5.2:** Area and volume adjustment of a glacier in response to changing climate. (A) shows a glacier out of balance with the climate, where  $\text{ELA}_0$  marks the ELA corresponding to the  $\text{AAR}_0$ . (B) shows the glacier after having undergone the area and volume adjustment needed to again be in dynamic equilibrium with the climate. The average ELA has now become the  $\text{ELA}_0$  and the ablation area notably shrank while the accumulation area remained the same. The figure is based on Box et al. (2022).

### 5.2.1 Retrieval of Landsat imagery

The Landsat imagery used in this study is retrieved through Google Earth Engine (Gorelick et al., 2017). First, all available scenes covering Mittivakkat between and including 1984 and 2023 are filtered to only include those from August and September as these are the two months during which the end of the melt season and with that the maximum bare ice extent and AAR are expected to be observed. Then, the scaling factors given in the Landsat user guides are applied to the retrieved bands (1-5 and 7<sup>1</sup>) to rescale the reflectance values from unsigned 16-bit integers back to the original floating-point number between 0 and 1 (Sayler, 2021, 2024; USGS, 2021). The imagery is then filtered to avoid scenes where clouds are obstructing the

<sup>1</sup> Note that only the blue band (band 1 or 2, depending on the sensor) is used in the final workflow, but more bands were retrieved to 1) create true color images to visually assess the glacier and 2) investigate whether some of the other bands could be used as additional features in the classification algorithm.

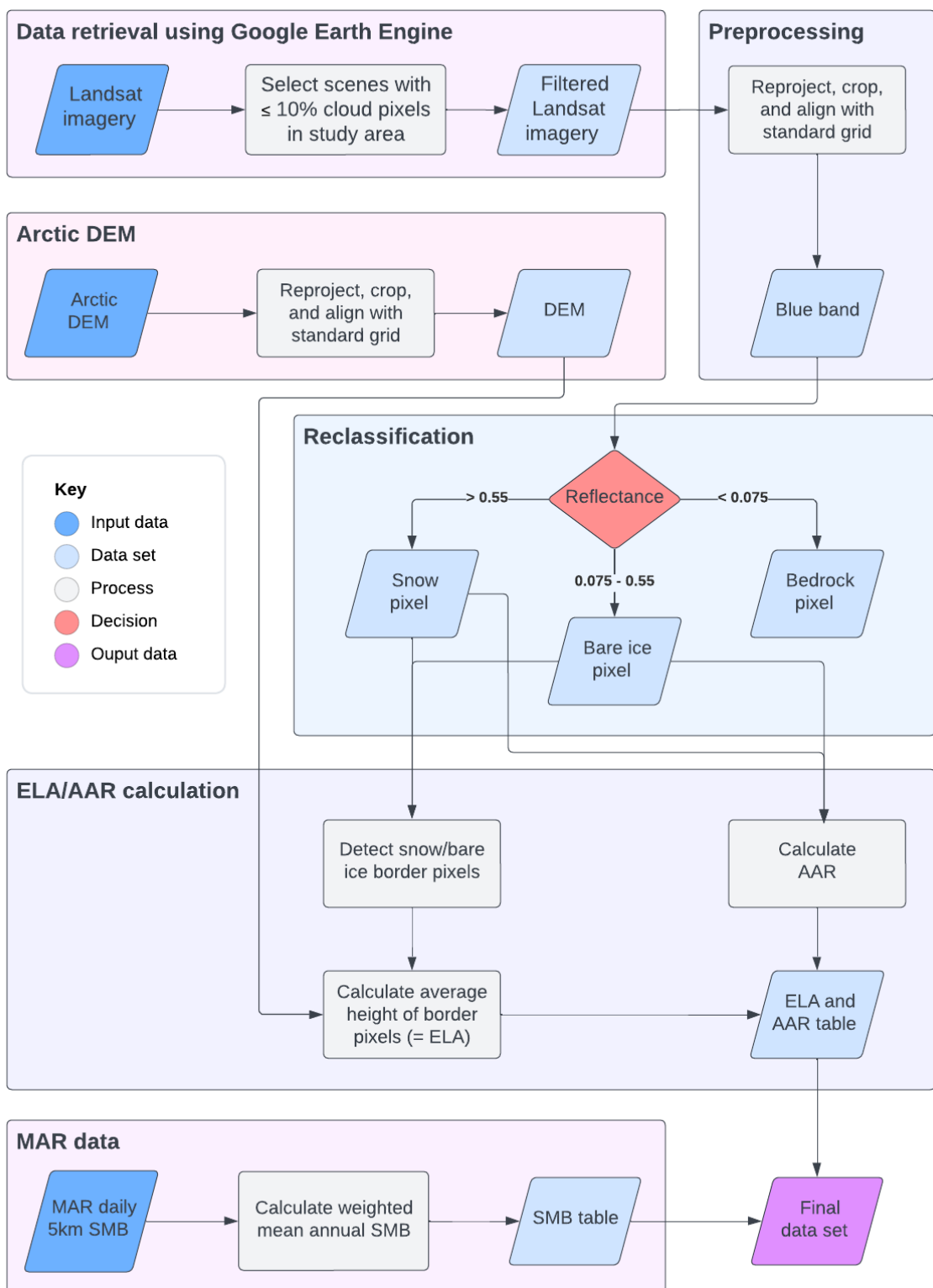


**Figure 5.3.:** Methodology flowchart.

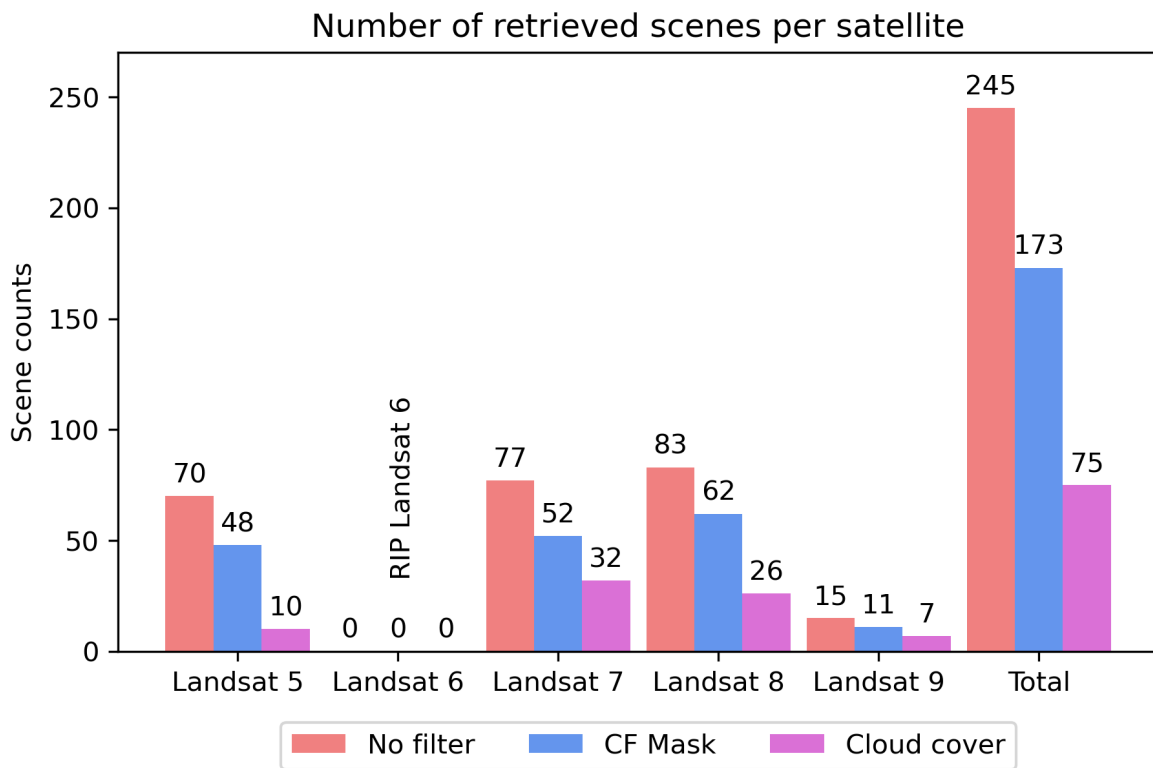


**Figure 5.4.:** Number of retrieved Landsat scenes based on different filter approaches for each satellite.

view of the study area. While each Landsat scene includes a cloud cover value that describes what fraction of the scene is covered by clouds, this value is calculated for the entire scene with an extent of 180 x 185 kilometers which results in numerous instances of false inclusion or omission of scenes when filtered based on this value (NASA, 2021h). To avoid this issue, the relative cloud cover for only the study area is used for cloudiness filtering. It is computed based on the cloudiness of each individual pixel as determined by the CFMask algorithm described in the data chapter above (Sayler, 2021, 2024; USGS, 2022a). All scenes with a cloud cover of 10% or less in the study area are deemed fit for further analysis, cropped to a small rectangular area around Mittivakkat, and then exported as GeoTIFF files (for exact coordinates of rectangular area, see script *create\_mask.py* in Appendix B).

In total 245 Landsat scenes are available for the time period investigated in this study, 173 of which have been retrieved using the methodology described above, more than twice the number of scenes that would have been retrieved if they had been filtered using the cloud cover score available for each Landsat scene at the same 10% cloud cover threshold. The number of scenes for each satellite and filter method are shown in Figure 5.4 above.

As cloud detection over ice and snow surfaces is often unreliable, all scenes were visually assessed for any obvious errors or data issues and deleted from the data set if deemed necessary.

**Table 5.1.:** Scenes preemptively deleted from the data set due to sensor errors or failed cloud detection.

Satellite	Scene	Reason
Landsat 5	01.08.1992	Sensor error over snow surface unrealistically distorting AAR
Landsat 7	21.08.2011	Unmasked cloudy image
Landsat 8	06.09.2014	Unmasked cloudy image
Landsat 8	19.09.2016	Unmasked cloudy image
Landsat 8	18.09.2021	Unmasked cloudy image
Landsat 8	21.09.2022	Unmasked cloudy image

Table 5.1 below gives an overview the deleted scenes. All subsequent computations are then performed using Python version 3.12.3 (Python Software Foundation, 2024).

### 5.2.2 Pre-processing

First, the two ArcticDEM mosaics are merged and then resampled to a pixel resolution of 30 meters with each pixel being assigned the average value of all original pixels that lie within its extent. Then both the DEM and the Landsat data are reprojected to a common grid (corresponding to the extent of Figure 6.2) in the UTM zone 24N (EPSG: 32624) to exactly align the pixels in both data sets. The coordinates of the corner pixels and the projection of the common grid are taken from the grid on which Landsat imagery is projected when accessed through the USGS Earth Explorer website, as this is the grid used for the outline of Mittivakkat glacier in the Randolph Glacier Inventory (USGS, 2024a). Finally, the DEM and Landsat imagery are cropped to the extent of the glacier as defined in the Randolph Glacier Inventory and all images with more than 20% missing data (e.g., due to sensor failures such as discussed Chapter 4.5.2) are excluded from further analysis.

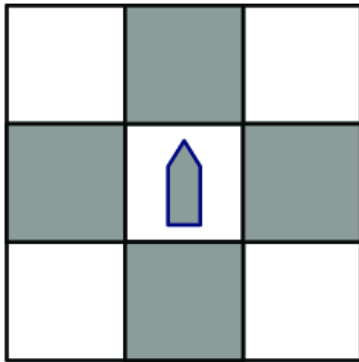
### 5.2.3 Surface classification

The cropped Landsat imagery is classified into the three land cover classes *bedrock*, *bare ice*, and *snow* based on the reflectance value of the blue band (wavelength region between  $0.45\mu\text{m}$  and  $0.515\mu\text{m}$ ). The threshold values for the classes have been determined by manually assessing the histograms of randomly chosen images from all 4 sensors and are shown in Table 5.2 below. The advantages and limitations of this approach are discussed in detail in the Chapter 7.1.1.

### 5.2.4 ELA and AAR calculation

The calculation of the ELA and AAR is then quite straightforward: for each scene, all snow pixels that have at least one bare ice pixel in their k1-Moore neighborhood (see Figure 5.5) are

## Von Neumann neighborhood



## Moore neighborhood

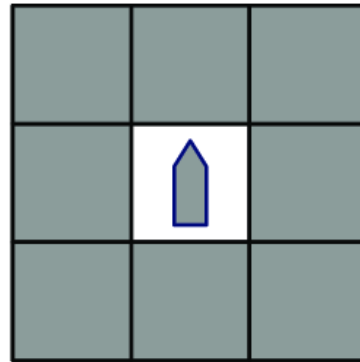


**Figure 5.5.:** k1-Moore neighborhood compared to k1-Von Neumann neighborhood. Source: Lazarowska (2020).

labeled as snowline pixels. The ELA is then determined by calculating the average height of these snowline pixels based on the DEM and the AAR is computed by simply adding up the area of all snow pixels and dividing it by the total area of snow and bare ice pixels. This way, the method automatically accounts for glacier retreat as bedrock pixels are not included in the AAR calculation.

Finally, the scene with the lowest AAR value of each year is chosen, as the AAR of a glacier is defined as the lowest ratio between accumulation and total area. The scenes with the lowest AAR also serve as the dates marking the beginning and end of the respective hydrological years used for the surface mass balance calculation (Box et al., 2022).

### 5.2.5 Surface mass balance calculation

The surface mass balance of Mittivakkat glacier is calculated based on the surface mass balance product of the Modèle Atmosphérique Régional (MAR). First, the daily SMB raster files are cropped, resampled, and reprojected to the same common grid as the DEM and Landsat data as described above. Then the average of the SMB values of all pixels located within the extent of the study area is calculated for each day and then summed up based on the start and end dates

**Table 5.2.:** Reflectance threshold values.

Class	Reflectance threshold
Bedrock	< 0.075
Bare ice	0.075 - 0.55
Snow	> 0.55

of the hydrological years to determine the annual SMB. Due to missing imagery in 1994, 2008, and 2010, the end of the hydrological year can not be determined and is therefore defined as the 15th of September of the respective year.

Finally, the AAR, ELA, SMB, and hydrological year length data is collected in a single table that serves as the basis for all further analysis. The exact values for each variable and year can be found in Table A.1 in Appendix A.

# Results

This section describes the results of this study - here and below referred to as original data - and compares them with the corresponding data provided by the WGMS in FoG dataset - here and below referred to as WGMS data. The basic statistics of the regressions and correlations described here are given in the overview tables in Appendix A. This appendix also includes a table of all data produced in the analysis, so that the statistical relationships between the variables can be further investigated if so desired.

## 6.1 Equilibrium-line altitude (ELA)

### 6.1.1 Original data

Figure 6.1 below shows the evolution of the ELA at Mittivakkat glacier over time. Note that the ELA could not be calculated in 1994, 2008, and 2010, as no usable Landsat imagery could be retrieved for these years.

The mean ELA between 1985 and 2023 lies at 678 m a.s.l., while the highest and lowest ELA of 833 and 577 m a.s.l. are observed in 2012 and 2018, respectively. The location of the mean, low, and high ELA on the glacier surface is shown in Figure 6.2 below. The ELA has a standard deviation of 66 m and displays a large interannual variability.

A linear regression of the ELA against time (see dashed blacked line in Figure 6.1) shows that the ELA is estimated to rise by an average of 2.2 m per year, resulting in a total elevation gain of 85.8 m over the investigated period. While the regression is significant ( $p\text{-value} < 0.05$ ), it only explains 15% of the variance ( $R^2 = 0.150$ ) of the ELA, indicating that there are one or more explanatory variables missing. Except for the two extreme years of 2012 and 2018, all ELA values fall within the 95% confidence interval around the trend line (see black dotted lines in Figure 6.1). The residuals of the regression are normally distributed (according to the Shapiro-Wilk test by Shapiro and Wilk (1965)), do not show signs of autocorrelation (according to the Durbin-Watson statistic by Durbin and Watson (1971)), and are homoscedastic (according to the Breusch-Pagan test by Breusch and Pagan (1979)), so the basic assumptions of a linear regression are met and it can be assumed that the linear regression model is valid. The tests

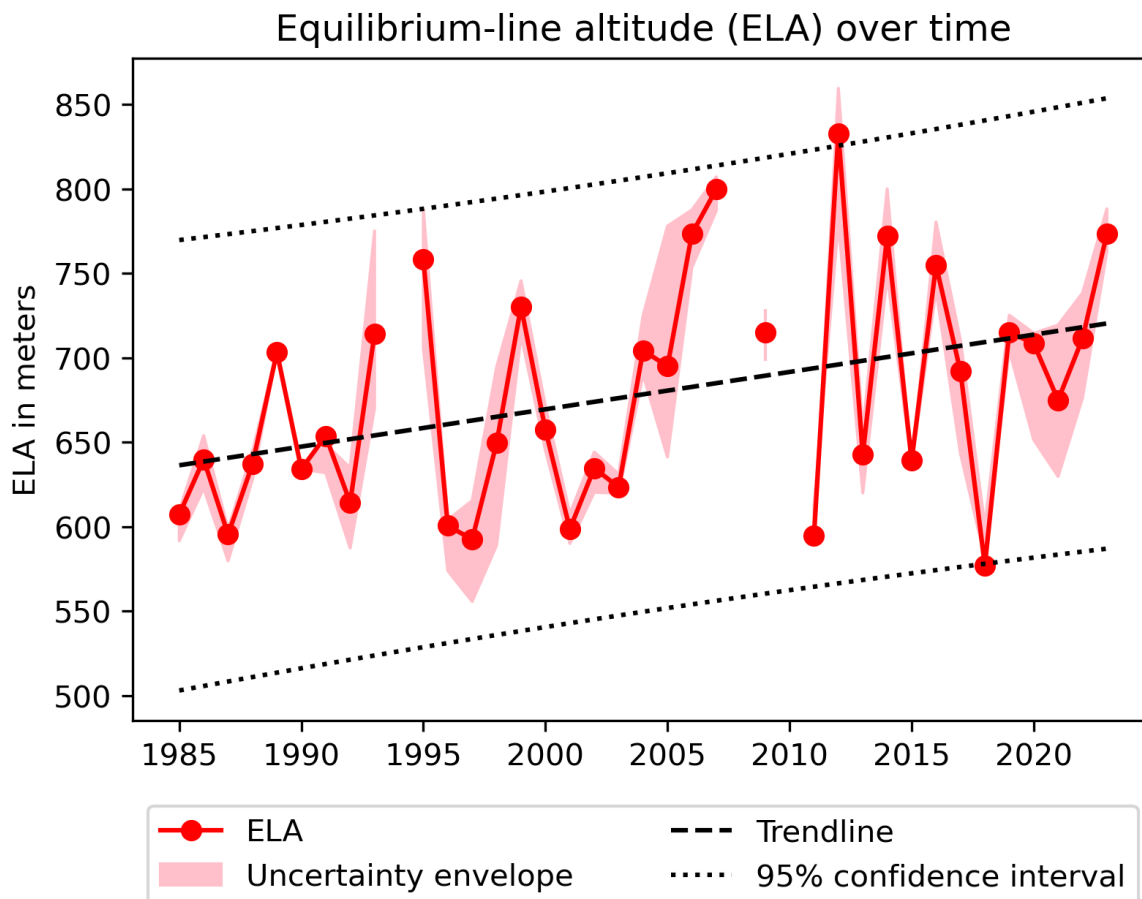


**Figure 6.1.:** ELA over time, including linear regression trend line and uncertainty envelope.

cited here have also been used to determine the validity of all other regressions in this study, if not otherwise indicated.

The light red envelope around the time series in Figure 6.1 represents the variation of the ELA in response to a slight variation of the threshold value between the bare ice and snow classes used in the surface classification. This has been done to quantify the extent to which the ELA might be influenced by an inaccurately determined threshold value. The upper limit of the envelope corresponds to a threshold value of 0.6, skewing the classification in favor of more bare ice pixels, while the lower limit corresponds to a value of 0.5, skewing the classification in favor of snow pixels - the original data time series uses a threshold value of 0.55. The average difference between highest and lowest ELA for each year is 40 m, with the largest uncertainty being observed in 2005 (137 m) and the smallest uncertainty in 1989 and 1990 (0 m, respectively<sup>1</sup>). Including the uncertainty envelope, the highest ELA is 860 m a.s.l. in 2012, and the lowest ELA is 555 m a.s.l. in 1997.

<sup>1</sup> This is likely due to the fact that the reflectance values of the Landsat 5 sensor used in these scenes sometimes "explode" to values > 1 over highly reflective snow surfaces, resulting in no change in snow pixel counts when the threshold value is varied.

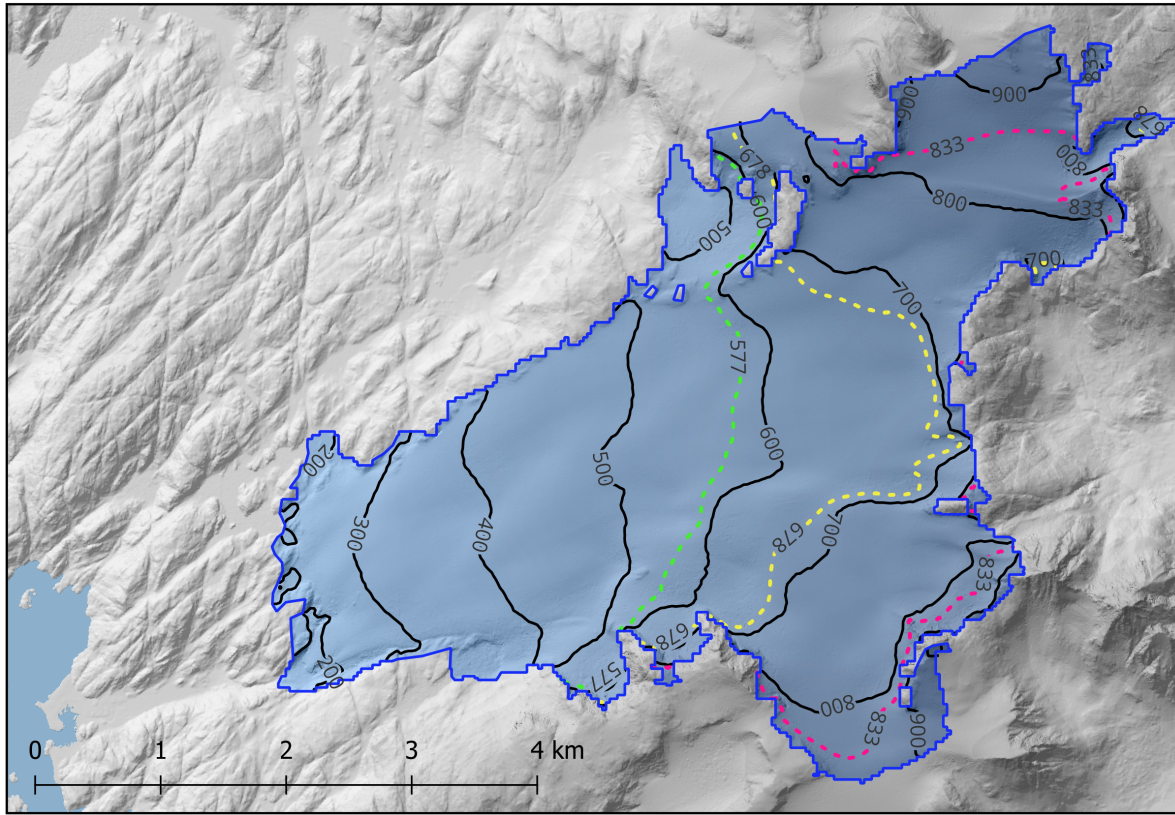


**Figure 6.2.:** Mittivakkat glacier with low, mean, and high ELA contour lines. Elevation in meters a.s.l.

### 6.1.2 Comparison with WGMS data

Figure 6.3 below shows a comparison between the ELA time series from the WGMS data set and the original ELA time series.

The mean ELA between 1996 and 2023 as reported in the WGMS data set is 778.6 m a.s.l., almost 100 m more than the 687.1 m a.s.l. observed in the original time series for the same period. The maximum ELA of 930 m a.s.l. (according to the WGMS data set, 930 m a.s.l. is the maximum elevation of Mittivakkat, meaning that in this case ablation is occurring on the entire glacier) is reported 13 times, but as an AAR of 0 is reported 14 times (see Table A.2), it can be assumed that the ELA must have lied at 930 m a.s.l. in 2019 as well, where it is currently only given as 900 m a.s.l. The minimum ELA of 390 m a.s.l. is reported in 2003. With a standard deviation of 171.3 m, the interannual variability is much larger than for original ELA time series. The average absolute difference between the two time series is 145.5 m.

There is a significant, but weak correlation between the two time series ( $p\text{-value} < 0.1$ ) with a Kendall  $\tau$  correlation coefficient of 0.28 (see Figure 6.4). Removing the years in which the ELA rises above the maximum height of the glacier would result in more significant slightly stronger correlation ( $p\text{-value} < 0.05$ ) with a correlation coefficient of 0.49, but there is no real basis upon which to exclude these extreme values as they represent real observations.

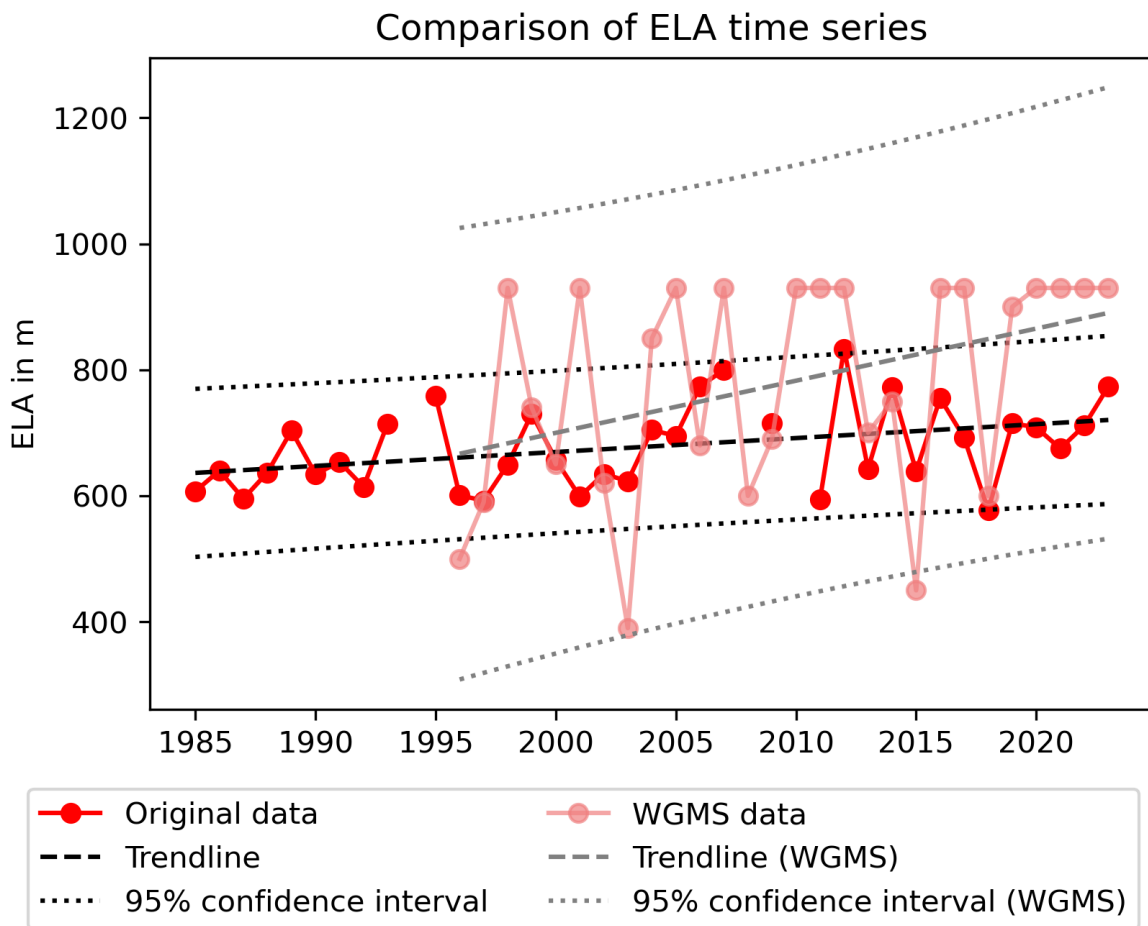


**Figure 6.3.:** Comparison of ELA time series including linear regression trend lines.

The regression of WGMS ELA against time is significant ( $p\text{-value} < 0.05$ ) with an estimated annual ELA rise of 8.3 m, which would result in a total ELA rise of 232 m since 1996, almost three times that projected for the original ELA time series since 1985 and four times that projected since 1996. With 15.3%, it explains almost the same amount of variance ( $R^2 = 0.153$ ) as the original ELA time series regression and except the second lowest ELA in 2015, all values fall within the 95% confidence interval of the regression.

## 6.2 Accumulation area ratio (AAR)

### 6.2.1 Original data

Figure 6.5 below shows the evolution of the AAR at Mittivakkat glacier over time. As for the ELA, no AAR could be calculated for the years 1994, 2008, and 2010, due to missing Landsat imagery.

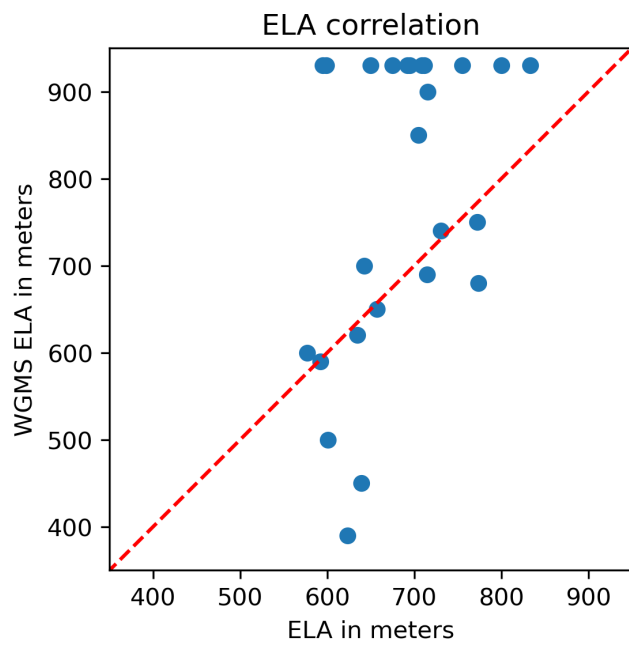


**Figure 6.4.:** Scatterplot of WGMS ELA against original ELA. The dashed red line illustrates a 1:1 correlation for reference.

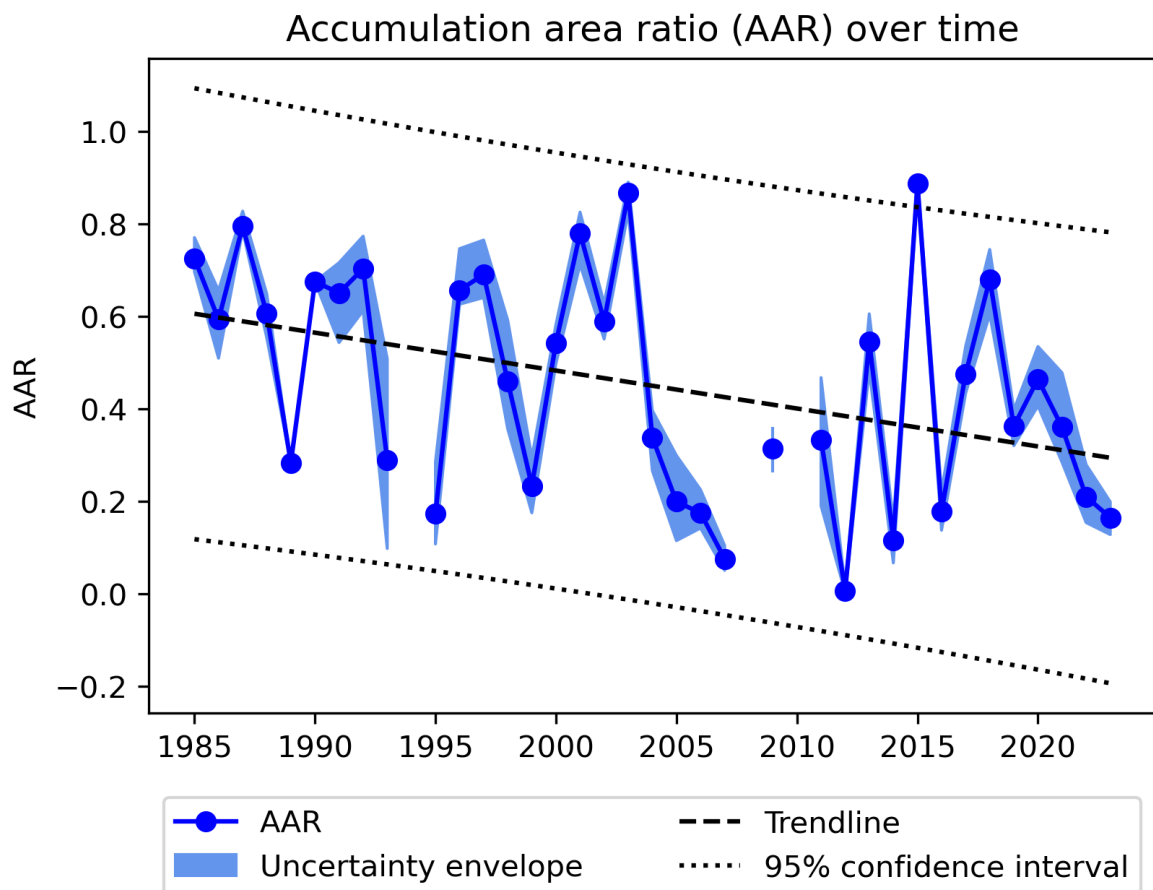


**Figure 6.5.:** AAR over time, including linear regression trend line and uncertainty envelope.

The mean AAR between 1985 and 2023 is 0.45, the maximum AAR of 0.89 is observed in 2015, and the minimum AAR of 0.01 is observed in 2012. The AAR has a standard deviation of 0.24 and shows a large interannual variability, similar to the ELA.

The linear regression of AAR against time is significant ( $p\text{-value} < 0.05$ ), but only explains 15.4% of its variance ( $R^2 = 0.154$ ), again indicating that one or more explanatory variables are missing. The AAR is estimated to shrink by almost 1 percentage point (slope coefficient of -0.0082) every year, which would result in a total AAR reduction of 32.0 percentage points over the investigated time period. Except for the maximum AAR value in 2015, all AAR values fall within the 95% confidence interval of the regression. Like with the ELA regression, the residuals do not show signs of autocorrelation, are homoscedastic, and follow a normal distribution, again fulfilling the basic assumption of a valid linear regression.

The light blue uncertainty envelope around the time series was calculated in the same fashion as for the ELA, with the upper limit corresponding to a threshold value of 0.5, skewing the classification in favor of a larger AAR, and the lower limit corresponding to a threshold value of 0.6, having the opposite effect. The average difference between largest and smallest AAR is 0.12, with the largest difference of 0.42 observed in 1993 and the smallest difference of 0 observed in 1989 and 1990, respectively. Including the uncertainty envelope, the largest AAR is 0.90 in 2015 and the smallest AAR is 0.003 in 2012.

### 6.2.2 Comparison with WGMS data

Figure 6.6 below shows a comparison between the AAR time series from the WGMS data set and the original AAR time series.

The mean AAR between 1996 and 2023 as reported in the WGMS data set is 0.16, less than half of the original AAR mean value of 0.40 in the same time period. The maximum AAR is 0.75 in 2003 and the minimum AAR of 0 is observed a total of 14 times, most notably in each of the last five years. With a standard deviation of 0.22, the WGMS time series has a similar interannual variability as the original one. The average absolute difference between the two time series is 0.25.

The two time series are significantly correlated ( $p\text{-value} < 0.01$ ) with a Kendall  $\tau$  correlation coefficient of 0.42 (see Figure 6.7), and the original AAR is always larger than the one given in the WGMS data set. Again, the correlation is notably weakened by the high number of extreme years with an AAR value of zero. Excluding these values would result in another significant ( $p\text{-value} < 0.01$ ) and much stronger correlation with a correlation coefficient of 0.63, but as with the ELA, there is no basis upon which to exclude these values.

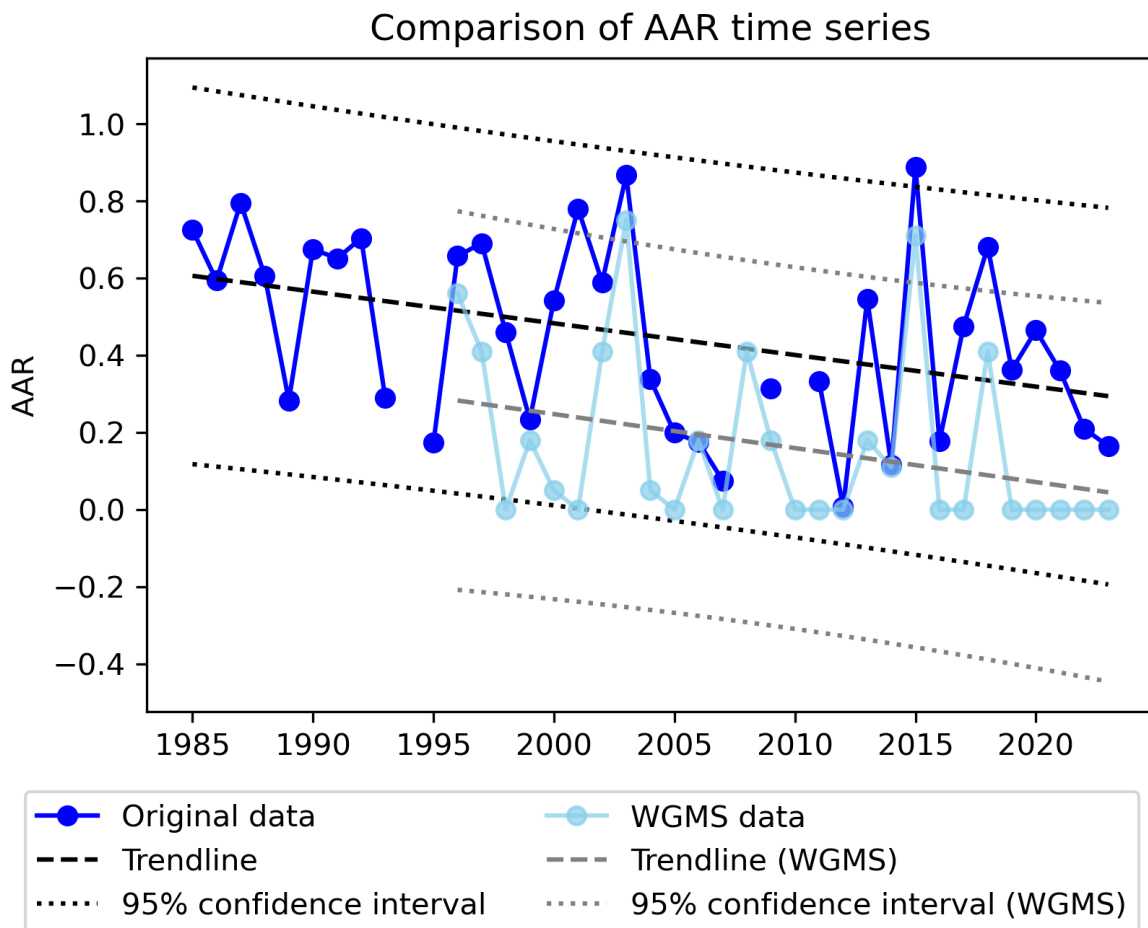


**Figure 6.6.:** Comparison of AAR time series including linear regression trend lines.

The regression of WMGS AAR against time is significant ( $p\text{-value} < 0.1$ ) and explains 9.8% of the variance ( $R^2 = 0.098$ ) of the time series. The slope coefficient of -0.0088 is very similar to that of the original time series. Based on the regression, the WMGS AAR decreased by 25.5 percentage points since 1996, compared to 23.8 percentage points for the original AAR regression in the same period or 32.0 percentage points since 1985.

## 6.3 Surface mass balance (SMB)

### 6.3.1 Original data

Figure 6.8 below shows the evolution of the SMB at Mittivakkat over time. Unlike with the ELA and AAR, the SMB time series has no gaps and is independent of variations of the classification threshold value.

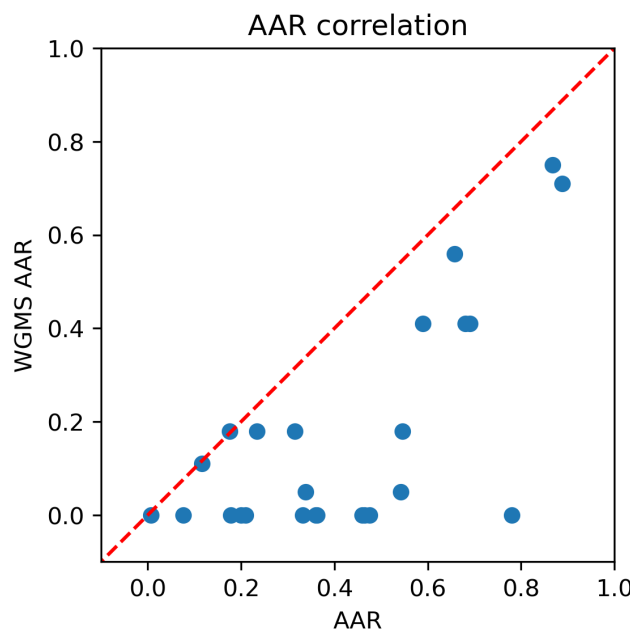


**Figure 6.7.:** Scatterplot of WGMS AAR against original AAR. The dashed red line illustrates a 1:1 correlation for reference.

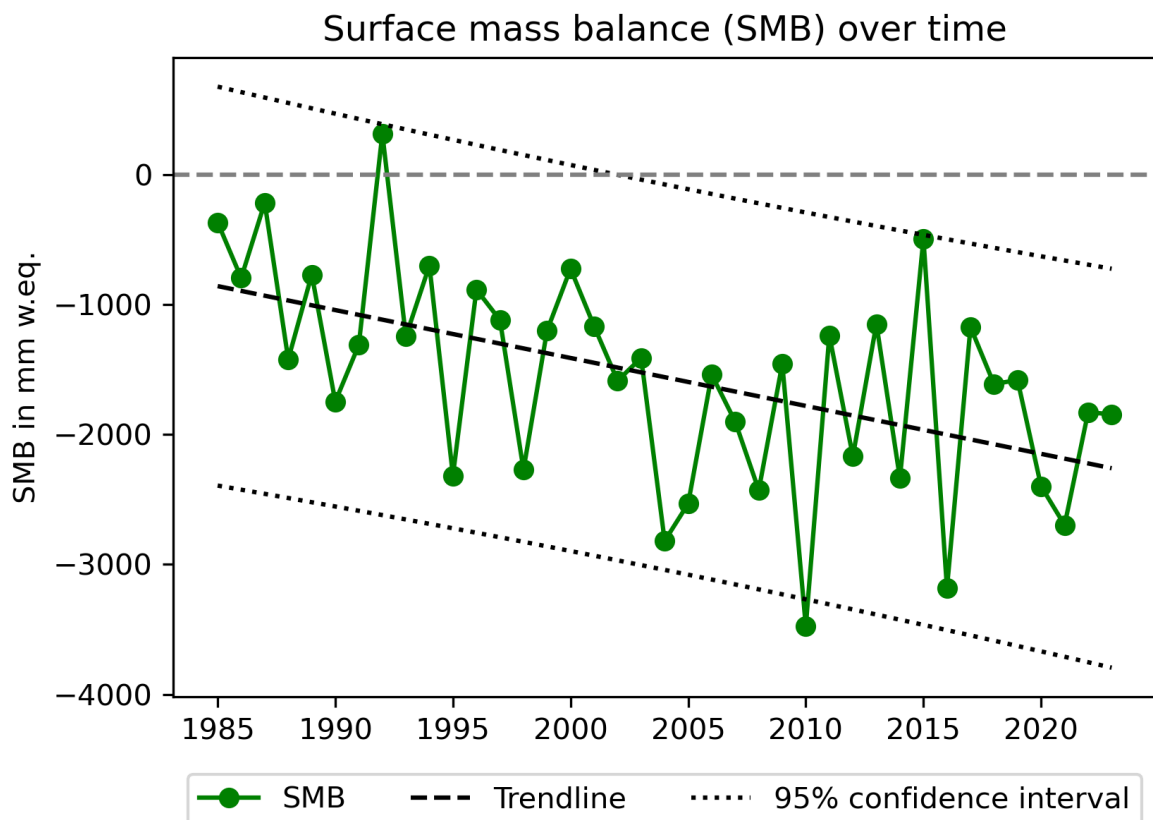


**Figure 6.8.:** SMB over time, including linear regression trend line. The horizontal light grey dashed line marks a SMB of 0 for reference.

The mean SMB between 1985 and 2023 is -1,558.3 mm w.eq., with a maximum mass loss of 3,475.9 mm w.eq. in 2010, and a maximum mass gain of 316.6 mm w.eq. in 1992, the only year with a positive mass balance<sup>2</sup>. The interannual variability of the SMB is large with a standard deviation of 817.6 mm w.eq.

The linear regression of SMB against time is highly significant ( $p\text{-value} < 0.001$ ) and explains 25.8% of the variance ( $R^2 = 0.258$ ) of the mass balance. The estimated annual mass balance loss increases by 36.9 mm w.eq. every year, resulting in a total annual mass loss increase of 1,439.1 mm w.eq. between 1985 and 2023. The total mass loss calculated as the sum of all annual SMB values is 60,775.4 mm w.eq. Except for the maximum mass loss in 2010, all SMB values fall within the 95% confidence interval of the regression. The residuals of the regression are homoscedastic and follow a normal distribution, but also show signs of autocorrelation, questioning the validity of the regression.

### 6.3.2 Comparison with WGMS data

Figure 6.9 below shows a comparison between the SMB time series from the WGMS data set and the original SMB time series.

The mean SMB between 1996 and 2023 as reported by the WGMS is -1,061.7 mm w.eq., roughly 700 mm less than for the original time series in the same time frame. The maximum mass gain of 340 mm w.eq. is observed in 2003, with another mass gain year in 2015. The maximum mass loss of 2,450 mm w.eq. is observed in 2011, more than 1,000 mm less than for the original SMB time series. The total mass loss is 29,728 mm w.eq., amounting to just under 60% of the mass loss calculated from the original data in this period. The standard deviation of 675.4 mm w.eq. is considerably lower than for the original time series, but the WGMS data still displays a large interannual variability. The average difference between the two time series is 830.1 mm w.eq.

With a Pearson correlation coefficient of 0.57, the correlation between the two SMB time series is notably stronger than for the ELA and AAR time series and highly significant ( $p\text{-value} < 0.01$ ) (see Figure 6.10).

The linear regression of WGMS SMB against time is significant ( $p\text{-value} < 0.05$ ) but explains only 16% of the variance ( $R^2 = 0.160$ ) compared to the 25.8% of the original time series. The slope of -33.4 mm w.eq. is again quite similar to that of the original time series and in the observed period the annual mass loss is estimated to have increased by 968.6 mm w.eq. Except the year 2015, all values fall within the 95% confidence interval of the regression.

---

<sup>2</sup> This anomalously high value is likely the result of low snow melt in all of Greenland in response to the eruption of Mount Pinatubo in June/July 1991 (Box, 2002).

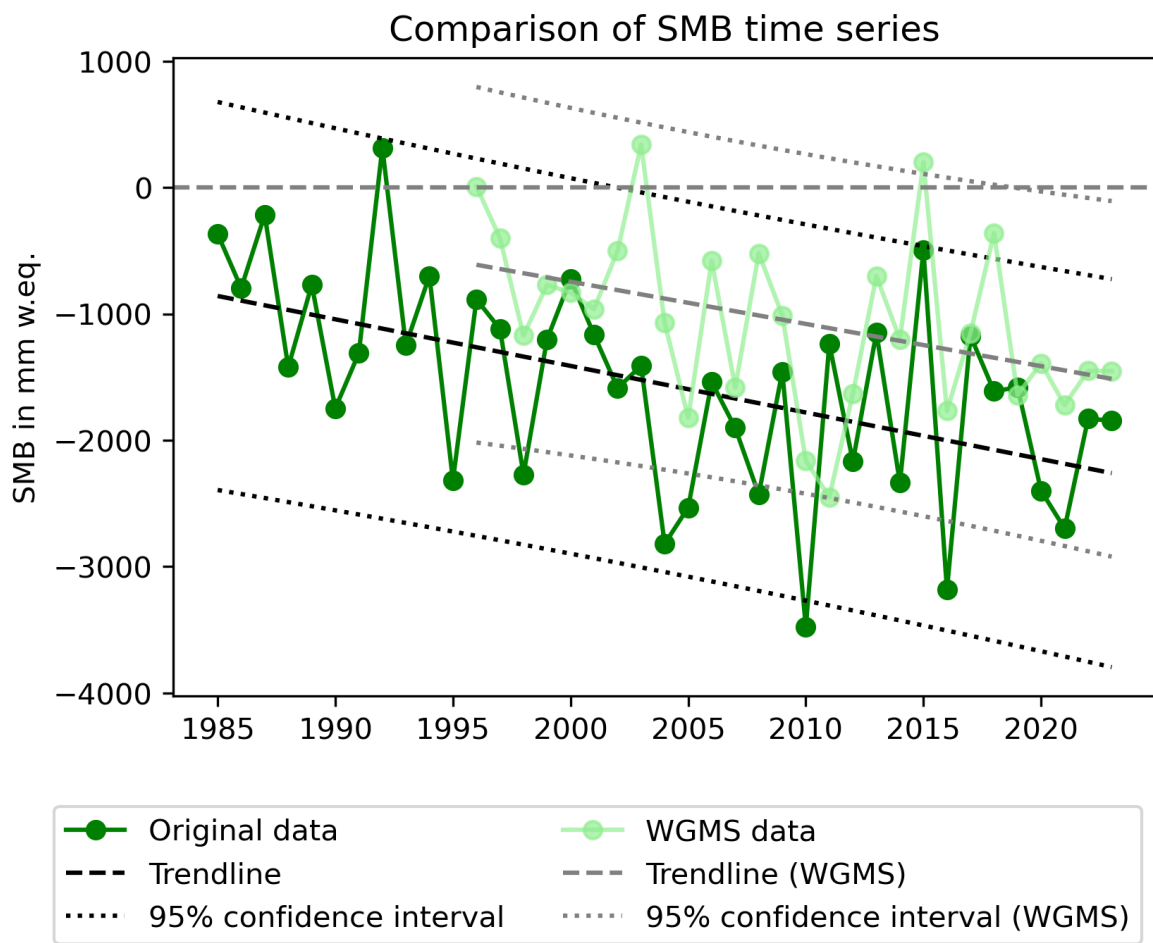


**Figure 6.9.:** Comparison of SMB time series including linear regression trend lines. The horizontal light grey dashed line marks a SMB of 0 for reference.

## 6.4 Glacier area

Figure 6.11 below shows the evolution of accumulation and ablation area sizes over time, as well the evolution of the total glacier area and the AAR for reference.

The area of the accumulation and ablation zones was calculated from the pixel counts of snow and bare ice pixels, respectively, with the total glacier area simply being the sum of the two. The average size of the accumulation area is 8.61 km<sup>2</sup>, with a maximum extent of 17.46 km<sup>2</sup> in 2015 and a minimum extent of just 0.10 km<sup>2</sup> in 2012. The average size of the ablation is 9.99 km<sup>2</sup>, with a maximum of 16.41 km<sup>2</sup> in 1996 and a minimum of 2.21 km<sup>2</sup> in 2015. Based on this, the average total size of the glacier is 18.61 km<sup>2</sup>, with a maximum extent of 20.15 km<sup>2</sup> in 1990 and a minimum extent of 15.19 km<sup>2</sup> in 2023.

The linear regression of total glacier area against time is highly significant ( $p\text{-value} < 0.001$ ) and explain 50.2% of the glacier area variance ( $R^2 = 0.502$ ), with an estimated annual area

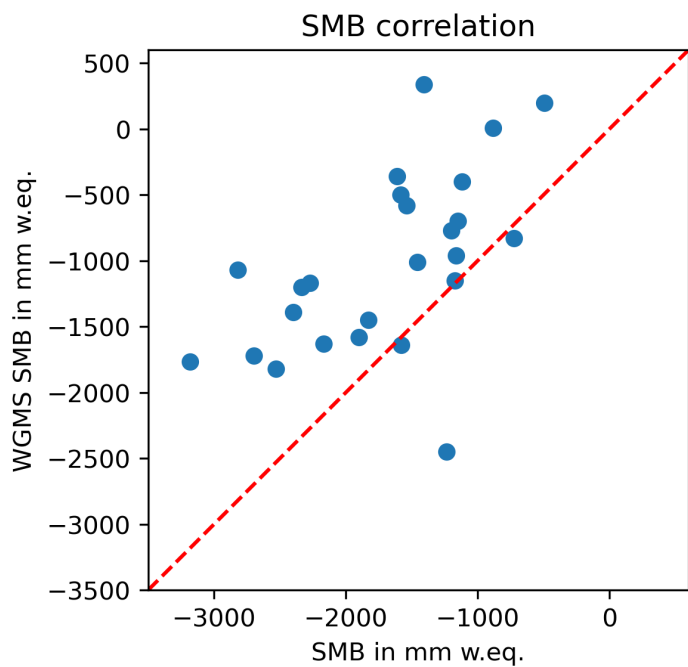


**Figure 6.10.:** Scatterplot of WGMS SMB against original SMB. The dashed red line illustrates a 1:1 correlation for reference.

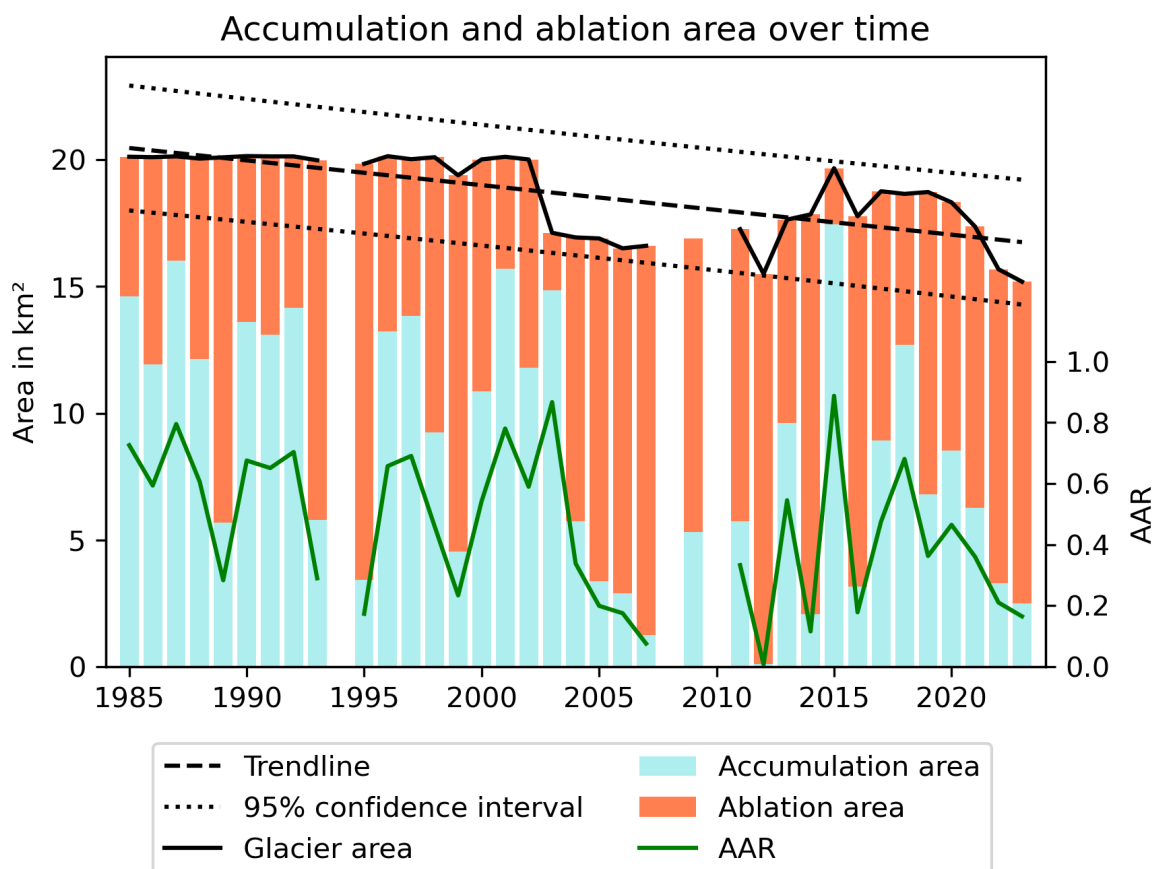
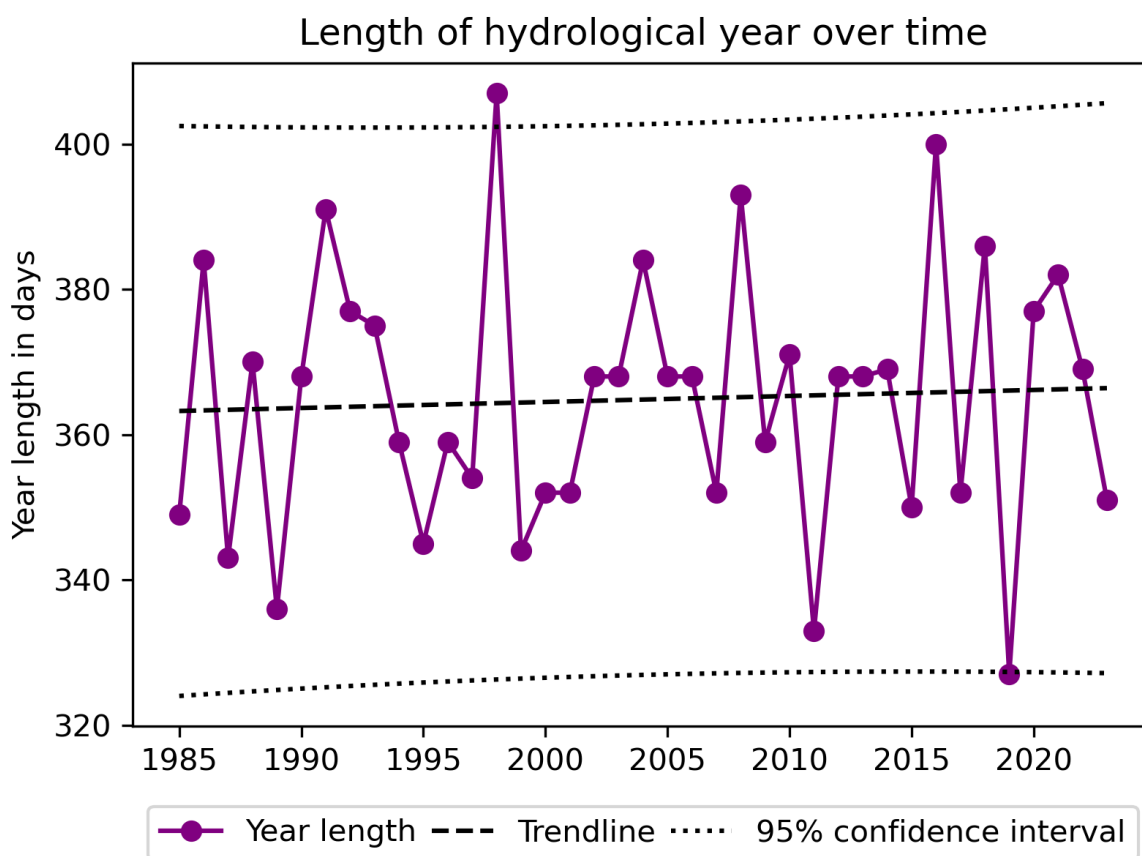


**Figure 6.11.:** Accumulation, ablation, at total glacier area over time.

loss of 0.098 km<sup>2</sup> and a total loss of 3.82 km<sup>2</sup> since 1985. All values fall within the 95% confidence interval of the regression. The residuals are normally distributed, but show signs of autocorrelation and heteroscedasticity, so the basic assumptions of the linear regression are not met, and the validity of the regression is questionable. This is likely a result of the dramatic area loss between 2002 and 2003, and subsequent area gain between 2010 and 2015 which is further discussed in Chapter 7.3.7.

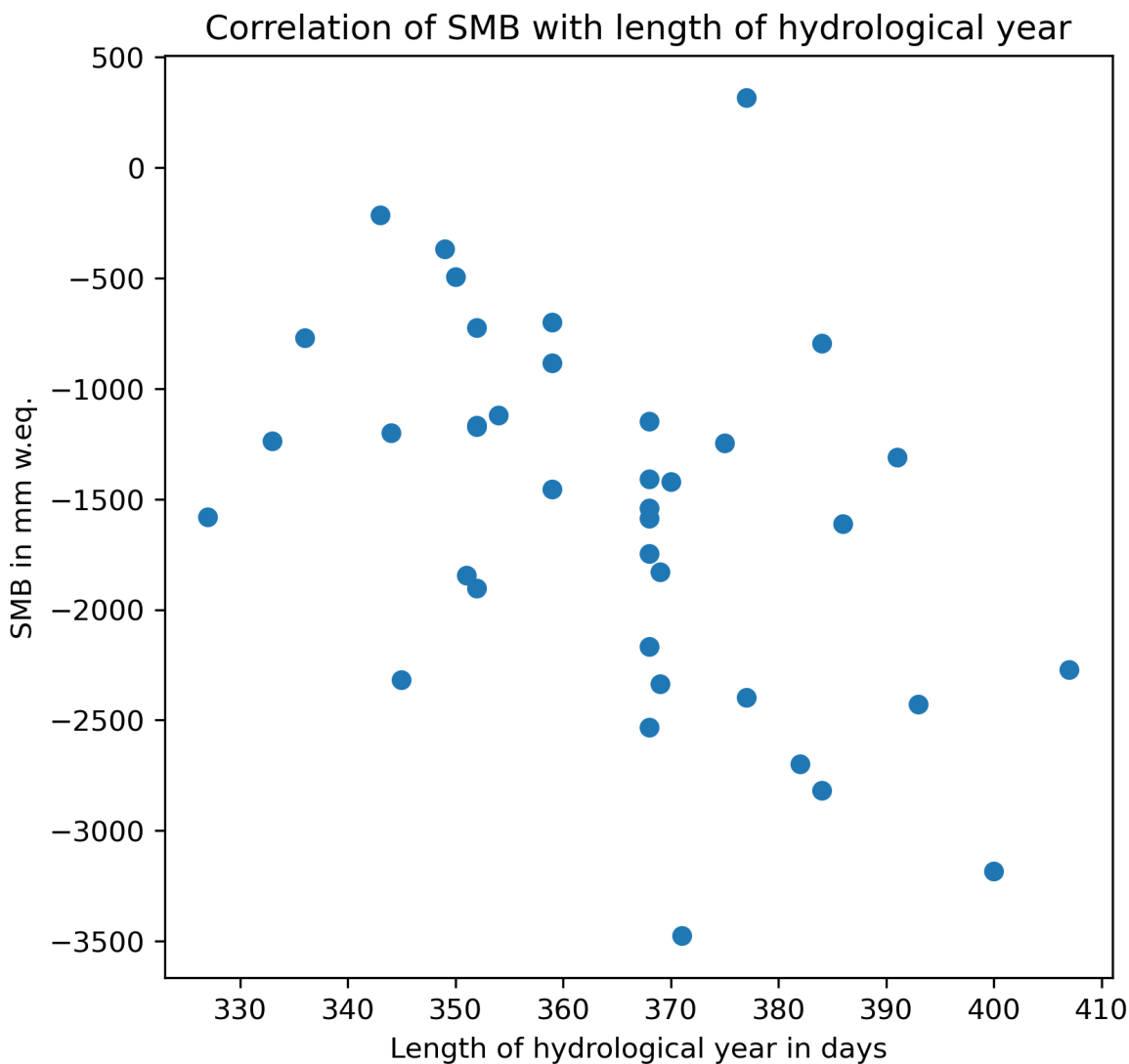
## 6.5 Length of hydrological year

Figure 6.12 below shows the evolution of the length of the hydrological year at Mittivakkat over time.



**Figure 6.12.: Length of hydrological year over time, including linear regression trend line.**

The mean length of the hydrological year between 1985 and 2023 is 364.8 days, almost exactly the same as the assumed mean length of 365 days. The longest hydrological year is 1997/98 with 407 days, while the shortest year is 2018/19 with 327 days. As with the ELA, AAR, and SMB time series the interannual variability of the year length is large, with a standard deviation of 18 days.



**Figure 6.13.:** Scatterplot of SMB against length of the hydrological year.

The linear regression of year length against time is insignificant ( $p\text{-value} = 0.755$ ) and would only explain 0.3% of the variance ( $R^2 = 0.003$ ) of the time series, with an estimated annual year length increase of 0.083 days or roughly 2 hours. Except for the maximum and minimum year lengths in 1997/98 and 2018/19, all values fall within the 95% confidence interval of the regression. The residuals are homoscedastic and follow a normal distribution but show signs of autocorrelation. As the regression is insignificant anyways, its validity is of no concern.

The regression of the melt season end date against time is also insignificant ( $p\text{-value} = 0.790$ ), so there does not seem to be any sign of the melt season extending to later dates in the year. There is, however, a significant ( $p\text{-value} < 0.01$ ) negative correlation between the length of the hydrological year and the SMB with a Pearson correlation coefficient of -0.44. This is to be expected given the way that the surface mass balance is calculated and the fact that – with one exception – the annual SMB is always negative (see Figure 6.13).

## 6.6 AAR-SMB regression

### 6.6.1 Original data

Figure 6.14 below shows the regression of AAR against SMB used to determine the  $AAR_0$  of Mittivakkat glacier in the period from 1985 to 2023.

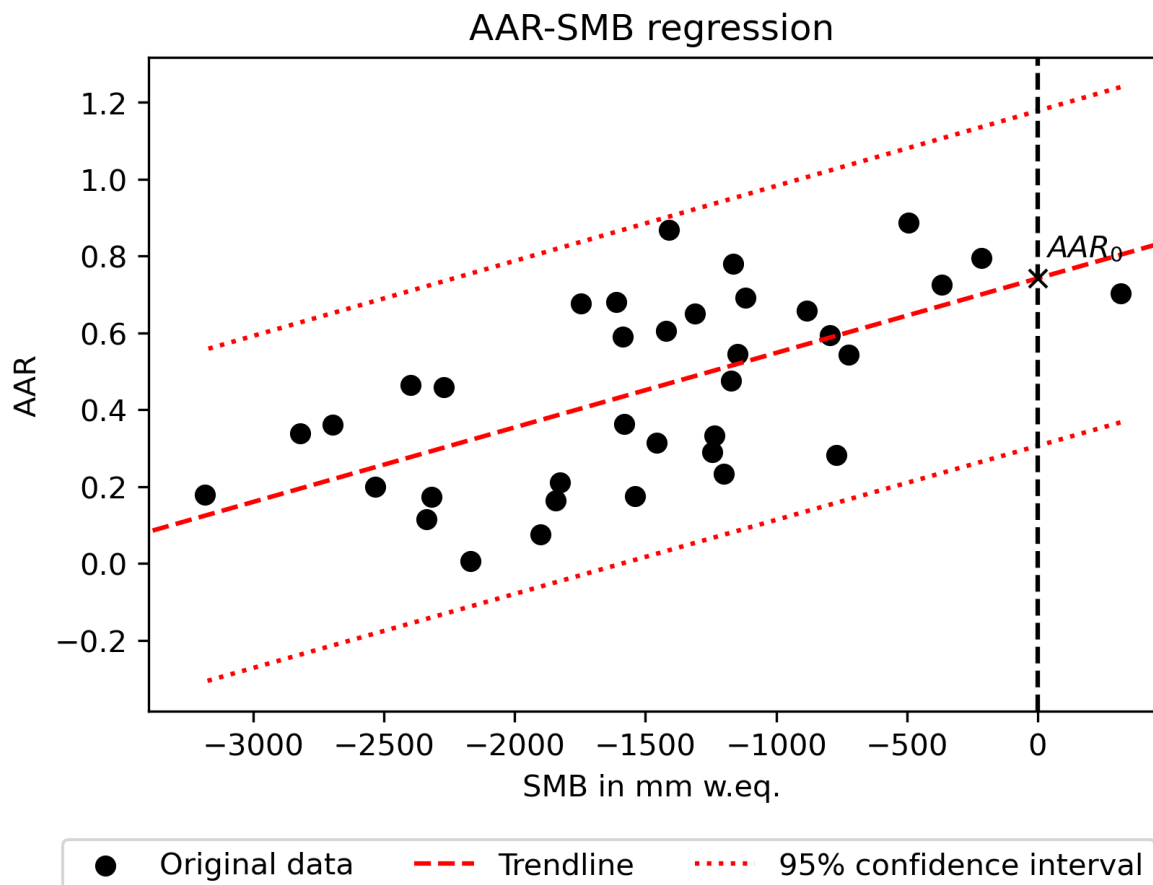


**Figure 6.14.:** Regression of SMB against AAR for original data.

The regression of AAR against SMB is highly significant ( $p\text{-value} < 0.001$ ) and explains 37.2% of the variance ( $R^2 = 0.372$ ) of the data set. The slope coefficient of 1.94E-04 translates to a SMB decrease of 51.5 mm w.eq. for an AAR decrease of 1 percentage point. Assuming an AAR decrease of 32.0 percentage points as calculated in Chapter 6.2.1, the annual SMB would have reduced by 1,648 mm w.eq. since 1985, which is reasonably close to the estimated annual SMB decrease of 1,439.1 mm calculated in Chapter 6.3.1. All data points fall within the 95% confidence interval of the regression and the residuals are homoscedastic, show no signs of autocorrelation, and follow a normal distribution.

The  $AAR_0$  as given by the regression model is 0.74. In relation to the time-averaged AAR value of 0.45, this gives a fractional imbalance of  $\alpha = 0.607$ , meaning that Mittivakkat glacier would

have to lose 39.3% of its area to again reach a dynamic equilibrium state with the current climate (meaning the climate between 1985 and 2023). Assuming a glacier extent of 20.15 km<sup>2</sup>, this amounts to an absolute area loss of 7.92 km<sup>2</sup>. Applying the area-volume power law relationship described in Chapter 5.1 and the volume for Mittivakkat based on Mernild, Knudsen, et al. (2013) gives:

$$\Delta V = (0.607^{1.375-1}) 1.95 \text{ km}^3$$

$$\Delta V = -0.97 \text{ km}^3$$

The total expected volume loss required for Mittivakkat to reach an equilibrium state with the climate again would therefore be 0.97 km<sup>3</sup> or just under half (49.7%) of its current volume. Again, it needs to be stressed that this power law scaling only give a very rough estimate it applied to only a single glacier. In order for the AAR<sub>0</sub> to be 0.74, the ELA needs to be 478.1m a.s.l., compared to the time-averaged ELA of 678.4 m a.s.l. shown in Figure 6.16.

### 6.6.2 Comparison with WGMS data

Figure 6.15 below shows the regression of AAR (WGMS) against SMB (WGMS) used to determine the AAR<sub>0</sub> of Mittivakkat glacier in the period from 1996 to 2023 with the original regression for reference. Note that all years where the AAR was zero have been removed from the data set, as the linear relationship between AAR and SMB does not necessarily hold true when the AAR is either 0 or 1 (Mernild et al., 2011). This is due to the fact that both ablation and accumulation rates can continue to rise when the glacier is losing or gaining mass at every point on its surface without the AAR changing any further.

The regression of WGMS AAR against WGMS SMB is highly significant (*p-value* < 0.001) and explains 90% ( $R^2 = 0.900$ ) of the variance of the data. The slope coefficient is 4.74E-04, meaning that an AAR decrease of 1 percentage point would result in a SMB decrease of 21.1 mm w.eq. Assuming an AAR decrease of 25.5 percentage points since 1996 based on the regression in Chapter 6.2.2, the annual SMB in this period would have decreased by roughly 538.0 mm w.eq. or just over half (52.7%) of the 968.6 mm w.eq. annual SMB decrease projected in Chapter 6.3.2. Like with the original data AAR-SMB regression, all data points fall within the 95% confidence interval, and the residuals of the regression are homoscedastic, show no signs of autocorrelation, and follow a normal distribution.

Based on the WGMS regression the AAR<sub>0</sub> is 0.58. Compared to the time-averaged WGMS AAR of 0.16, this gives a fractional imbalance of  $\alpha = 0.276$ , meaning that Mittivakkat is projected to lose 72.4% of its area to return to a balanced state within the current (1996-2023) climate. In

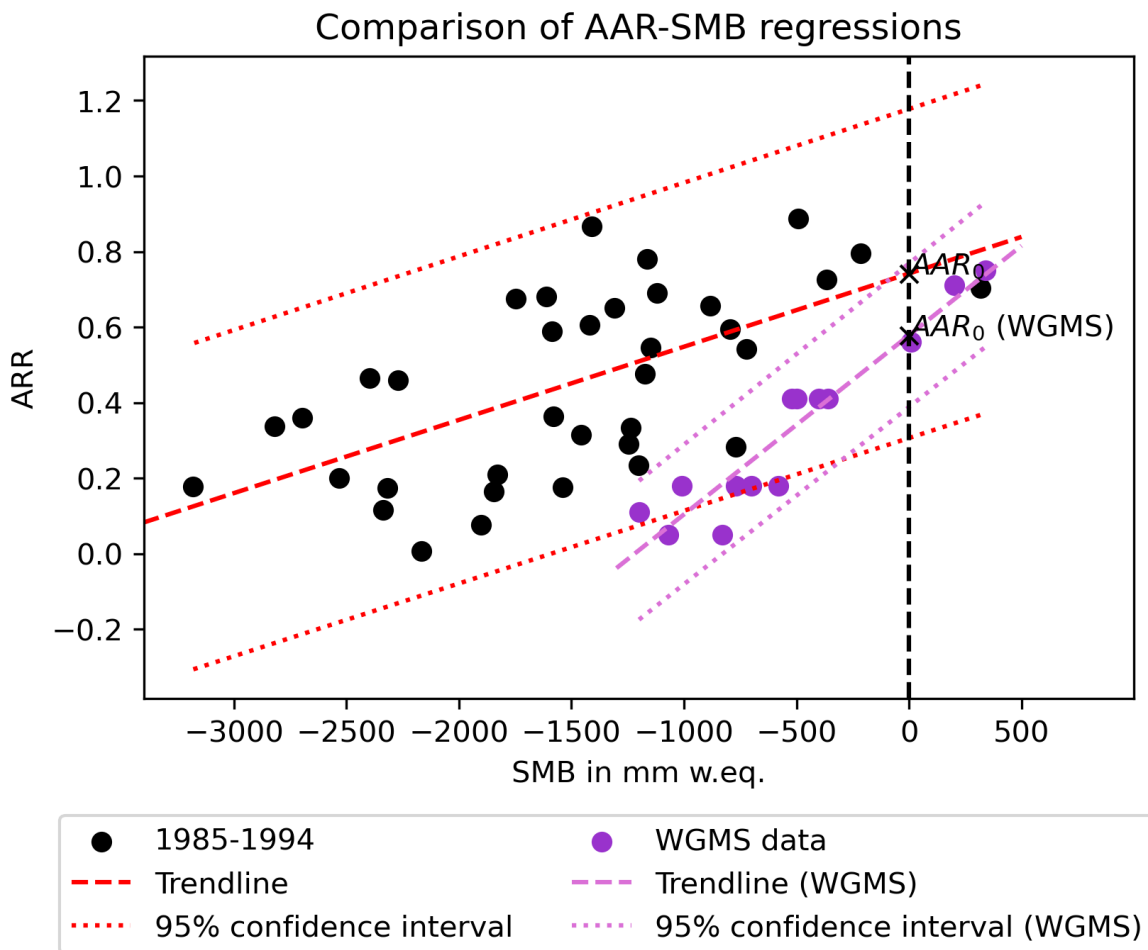


**Figure 6.15.:** Regression of SMB against AAR for WGMS data.

absolute terms, this means that Mittivakkat would have to lose an area of  $14.59 \text{ km}^2$ , assuming an area of  $20.15 \text{ km}^2$ . The associated volume loss is given as:

$$\Delta V = (0.276^{1.375-1}) 1.95 \text{ km}^3$$

$$\Delta V = -1.62 \text{ km}^3$$

This volume loss would amount to 82.9% of its current volume, roughly 1.75 times the expected volume change based on the original AAR-SMB regression. In order for the  $\text{AAR}_0$  to be 0.58, the ELA would have to lie at 584.3 m a.s.l., compared to the time-averaged equilibrium-line altitudes of 678.4 m a.s.l. determined in this study and 778.6 m a.s.l based on the WGMS data set (see Figure 6.16).

Notably, the  $\text{AAR}_0$  of each regression falls within the 95% confidence interval of the respective other regression. While both regressions have a quite large confidence interval, this indicates

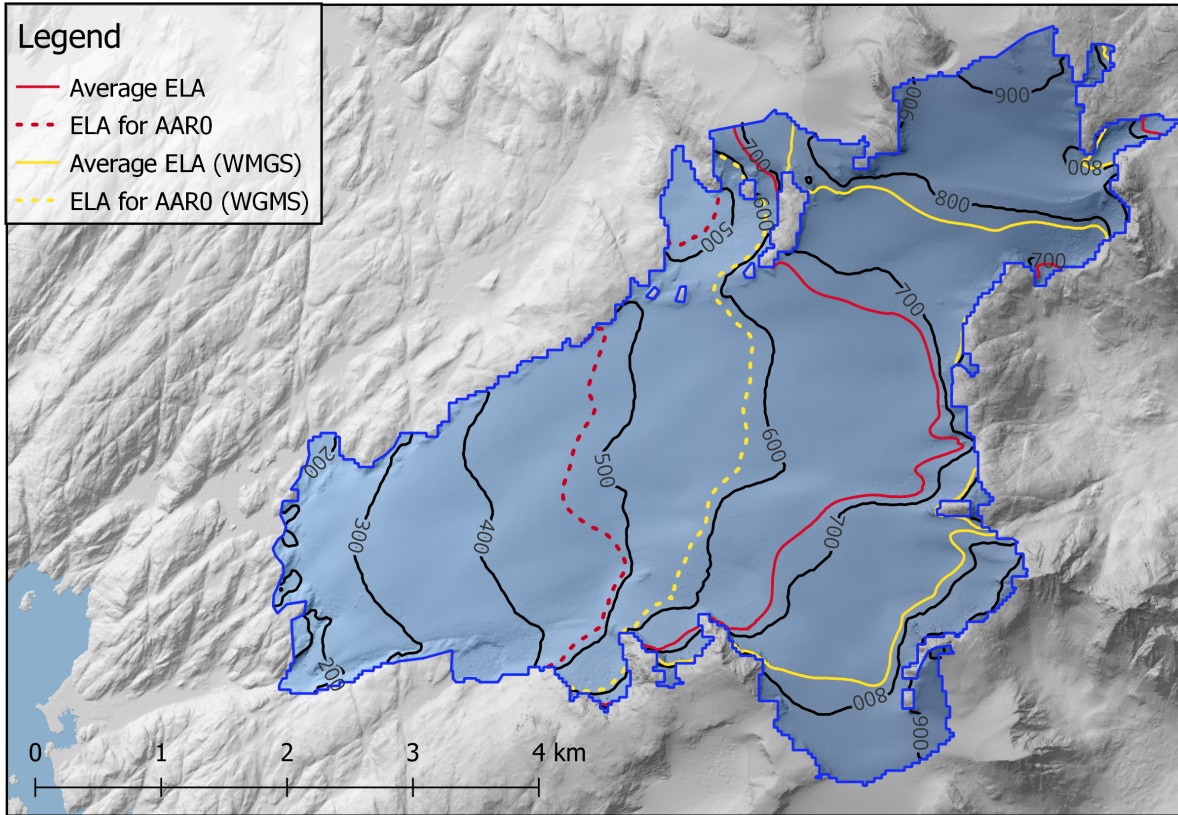


**Figure 6.16.:** Position of time-averaged ELA and ELA required for the glacier to be in equilibrium with the current climate.

a certain level of agreement between the remotely sensed data and the in-situ observations increasing the confidence in the applied methodology.

### 6.6.3 Comparison of SMB-AAR regression periods

According to the findings of Dyurgerov et al. (2009), the AAR<sub>0</sub> is not expected to change for the same glacier, even if it is calculated for different time periods – unless the periods are long enough for the climate to have significantly changed, resulting in a new AAR<sub>0</sub> value. A visual assessment of two original data AAR-SMB regressions – one for the period of 1985-2023, one for the period 1996-2023 – seems to confirm that removing the years before 1996 from that data set, does not have a large impact on the AAR<sub>0</sub> (see Figure 6.17).

It would therefore appear that the difference in slope and AAR<sub>0</sub> between original and WGMS data is not a result of the different periods used in the regression, but simply of the difference in AAR and SMB values for each year.

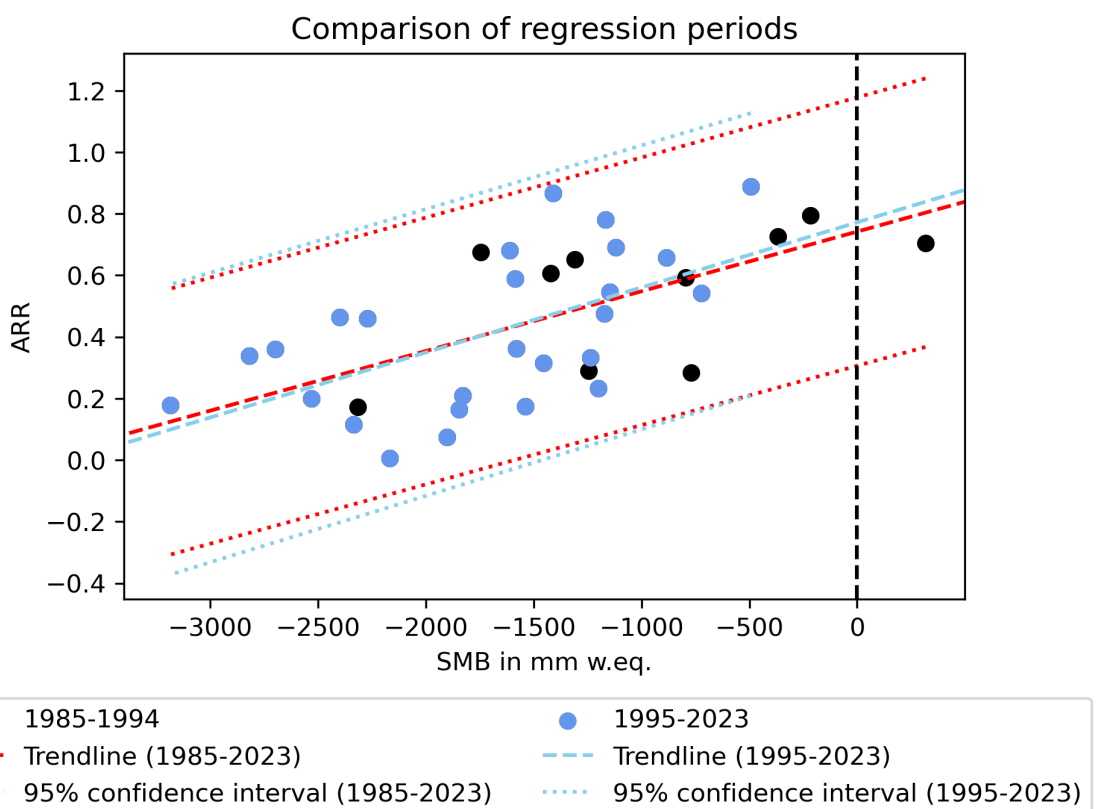


**Figure 6.17.:** Comparison of AAR-SMB regression based on original data.

# Discussion

This chapter discusses both the applied methodology and the results of the study presented in the previous chapter. It furthermore examines whether the chosen input data is well-suited for the goals of this study and gives a brief overview of ways in which the workflow could be improved to produce more reliable results in the future.

## 7.1 Methodology

This chapter investigates the applied methodology, first and foremost the classification algorithm, its caveats and shortcomings, and possible ways to improve it.

### 7.1.1 Classification

While the simple, threshold-based surface classification is both quick and computationally efficient, a side by side comparison of a true color image with its corresponding reclassification reveals that the algorithm is not terribly accurate (see Figure 7.1). This can for instance easily be seen in the small ice areas towards the glacier tongue that are falsely classified as snow patches.

One obvious solution to the issue would be an increase of the threshold value. This approach, however, would quickly result in the misclassification of snow pixels as bare ice, simply reversing the problem. One example for this is the southern-most snow patch where the current threshold seems to be working well, and where an increase of the threshold would result in more misclassification, especially in the shadowed slope within the southern half of the snow patch. Another one would be the second-most northern large snow patch that also illustrates how even a manual classification might not be straightforward as the darker snow areas are difficult to distinguish from brighter ice patches. A fully manual surface classification would also obviously be tedious and disagree with the goal of a fully automated tool chain.

While – for most of the scenes – most of the misclassified areas are quite small, this is still a major issue as the accumulation area (and with that the ELA) is technically only defined by

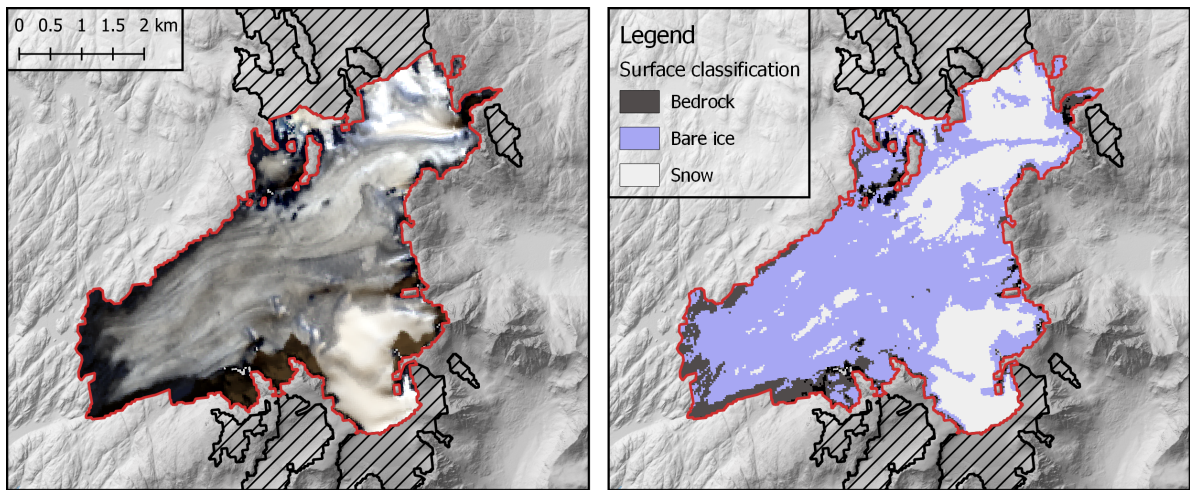


**Figure 7.1.:** Comparison of true color image (left) and corresponding classification (right) for Landsat 8 scene from the 15th of September 2023.

the larger areas of snow in the higher elevations of a glacier. Smaller snow patches should not be considered at all. In Figure 7.1, this would therefore mean that only the northern- and southern-most snow areas, and possibly parts of the second northern-most snowy area should be used to define the ELA. As the ELA is calculated as the average height of all snow pixels that are bordering a bare ice pixel, bare ice pixels that are misclassified as snow considerably distort the final ELA, especially if they are located in small patches at low elevations near the glacier tongue. Due to the small size of these snow patches, the number of edge pixels in relation to their area is much larger than for the larger snow areas, and they add a disproportionately large number of outliers to the data. This large number of outliers then stands in the way of an easy statistical solution, such as calculating the ELA as the median instead of the mean of the pixel elevations.

Instead, one would have to exclude these small snow patches from the data, regardless of whether they consist of misclassified bare ice or true snow pixels. An elevation threshold might offer a straightforward solution, but there are some issues with this approach: 1) the patches occur at every altitude on the glacier, so an elevation threshold would only be effective in masking out patches at low elevations, and 2) the height of the ELA fluctuates quite dramatically, so one would run the risk of distorting the data in years with a low ELA. An alternative could be a patch size-based threshold. While one would have to manually calibrate it for every glacier, it seems to be a more robust solution. Still, one could accidentally mask out the accumulation area in years with a very small AAR – a problem that would likely only become more acute as glacier melt advances.

The only real solution seems to lie in an improvement of the classification accuracy in combination with some manual exclusion of unwanted snow patches. As the main goal of this study is to develop a fully automated tool chain, this is obviously not the ultimately desired solution, but it would likely greatly improve the quality of ELA/AAR data, and one might be able to

further improve this approach later on – maybe with a relative size threshold value that is tied to the total area of the glacier<sup>1</sup>.

There are multiple ways in which the surface classification could be improved, first and foremost through the use of one of the more advanced classifiers discussed below. Instead of just using the reflectance of one band, these classifiers draw information from multiple spectral bands or even other pixel-level information, such as elevation or slope data to accurately classify the glacier surface. They do, however, require a set of labeled pixels (= pixels that have been manually assigned a class), the so-called training data, based on which they develop the “rules” used to classify unlabeled pixels. This makes these algorithms more computationally demanding and preparation-intensive than the approach taken in this study.

According to a meta-analysis of the most commonly used remote sensing pixel classification algorithms by Khatami et al. (2016), the most accurate classification algorithm is the Support Vector Machines (SVM) algorithm. This algorithm separates the input data into a predefined number of classes by fitting a so-called optimal separating hyperplane through the input feature space (Mountrakis et al., 2011). In this context, the term features refers to the pixel-level input data, such as the reflectance value at a specific wavelength or the elevation from a DEM. While the creation of a suitable training data set is obviously time- and work-intensive, the SVM algorithms are generally able to produce reliable results with a smaller amount of training data than other comparable algorithms. Moreover, they do not make assumptions about the statistical distribution of the input data, making them more versatile than for instance the formally widely used maximum likelihood classifiers (Khatami et al., 2016; Mountrakis et al., 2011). They are, however, more computationally demanding than other algorithms and requires high quality training data, as even a small number of misclassified pixels in the training data set can considerably reduce the overall accuracy of the classification (Mountrakis et al., 2011).

Another classification algorithm worth considering is the Random Forest (RF) algorithm that classifies pixels using multiple individual decision trees (Belgiu & Drăguț, 2016). While it was slightly outperformed by the SVM in the comparison study by Khatami et al. (2016), it has several advantages that make it an attractive alternative. For once, it does not require as many hyper-parameters to be set as the SVM, making it more easy to use and it also is reported to perform better for data sets with a large number of dimensions, meaning a large number of spectral bands or other input features (Belgiu & Drăguț, 2016). It is also less sensitive to mislabeled pixels in the input training data set and less computationally demanding although it does require an overall larger amount of training data (Belgiu & Drăguț, 2016; Khatami et al., 2016). Compared to the SVM it is also less prone to overfitting (Belgiu & Drăguț, 2016).

---

<sup>1</sup> Besides, the manual exclusion of unwanted snow patches sounds like a great job for one of the many international students at IGN looking to receive SU and I would love to think that my thesis put a fellow Climate Change student into work – think about it?

Lastly, more and more deep-learning based classification algorithms are being used in remote sensing as well, as they can often rival or even outperform SVM classifiers in terms of overall accuracy (Heydari & Mountrakis, 2019). One of the most used and best performing algorithms is the Convolutional Neural Network (CNN) which is based on the concept of iterative extraction of increasingly complex patterns out of an input data set (Heydari & Mountrakis, 2019). Like the SVM, however, CNNs are computationally demanding, especially with increasing complexity of the network and need more time than the SVM and RF during the training phase – this limitation will likely become less and less important in the future, however, as processing power increases (Heydari & Mountrakis, 2019).

When using one of the more advanced classifiers described above, one way to further improve the classification accuracy is the addition of more features into the input feature space. In this case, the elevation data might be useful, but there is another way to increase the number of input features without the need for more data sets: through the use of moving window kernels, different so-called texture statistics can be computed for a small region of the input satellite imagery (Khatami et al., 2016; Trias-Sanz et al., 2008). These statistics include for instance homogeneity, dissimilarity, or standard deviation of the pixel region and can help an algorithm to discern between two regions that otherwise appear very similar (Feng et al., 2015). One example could be the difference between grassland and forest, where the smooth texture of the grassland (likely low standard deviation) stands out again the rougher texture of the forest (likely higher standard variation) despite their otherwise similar spectral properties. In the case of classifying a glacier surface, the smooth and uniform surface of snow could be likely be easily distinguished from the bare ice surface with its characteristic flow lines and crevasses.

### 7.1.2 Landsat imagery retrieval

Google Earth Engine is built on a client-server programming model, where operations are recorded by so-called client-side proxy objects and then sent to a server where the actual computations are done (Gorelick et al., 2017). This means that Google Earth Engine is not built to be used with otherwise commonly used statements, like conditionals and for-loops, both of which are still used in the script for the Landsat imagery retrieval (Gorelick et al., 2017). This results in the script crashing often, making the retrieval process a bit tedious and at times frustrating. Still, the great increase in total retrieved imagery shown in Figure 5.4 makes up for the imperfect retrieval approach.

During the image filtering in Google Earth Engine a cloud cover of 10% is set as the threshold above which scenes are no longer exported. Later, in the Python-based section of the tool chain, however, a no-data threshold of 20% is applied, possibly resulting in instances where scenes are not exported from Google Earth Engine due to a cloud cover of more than 10% but less than 20%, even though they might have been suited for further analysis. Given that no Landsat

scenes were retrieved in 2008 and 2010, this waste of potentially usable scenes needs to be addressed.

## 7.2 Data

This chapter investigates the uncertainties associated with the chosen input data and their implications for the outcome of the ELA, AAR, and SMB time series and discusses possible alternative data sources.

### 7.2.1 Landsat data

While the spatial resolution of the Landsat imagery seems to be sufficiently high to allow for an accurate estimate of the ELA and AAR, the temporal resolution is far too low for the purpose of determining the exact date at which the ablation season ends.

The revisit time for Landsat imagery after the launch of Landsat 7 in 1999 has decreased from 16 to 8 days as the orbits of Landsat 5 and 7 were exactly 8 days out of phase, as later the orbits of Landsat 7 and 8, and now Landsat 8 and 9 as well (NASA, 2021i; Kristi Sayler, personal communication, 20th of June 2024). Due to the limited down-link capacity of Landsat 5 and 7, however, no imagery was taken over Greenland after the launches of Landsat 7 and 8, respectively, resulting in a low 16-day revisit time over Greenland up until the launch of Landsat 9 in 2021 (NASA, 2021i; Kristi Sayler, personal communication, 20th of June 2024). While there is no way to investigate, how many days lie between the AAR calculated from the Landsat imagery and the true AAR date, they could theoretically be up to 16 days apart, during which a large amount of melt might still take place – the low temporal resolution therefore introduces a positive bias to the AAR calculation and a negative bias for the ELA calculation.

An alternative to Landsat could be the PlanetScope program which consists of a constellation of 130 satellites, and provides daily imagery at a much higher spatial resolution of approximately 3 meters per pixel (Planet, 2024a). It does, however, only provide imagery starting July 2014, which likely is too short of a period to accurately estimate the  $AAR_0$  as is discussed in chapter 7.3.6 (Planet, 2024a). At a slightly lower resolution of 5 meters per pixel, the RapidEye program offers daily imagery from 2009 until 2020 which – in combination with PlanetScope – would result in a time series of 15 years, one year more than the WGMS series after the removal of the AAR-extreme years that could not be used (Planet, 2024b). These two satellite programs, however, only cover a limited section of the wavelength spectrum with only 5 bands for RapidEye and 4 bands for PlanetScope (8 bands starting in 2020) (ESA, 2024; Planet, 2024a). A higher spectral resolution and wider wavelength spectrum is offered by the Sentinel-2 program that consists of 2 satellites with a combined temporal resolution of 5 days

in Greenland starting in 2017 (Copernicus, 2024a, 2024b). The imagery from all of these programs could be used in combination with the others as well as with the Landsat imagery to combine the advantages of the higher temporal, spatial, and spectral resolution with the longer date range of the Landsat archive.

### 7.2.2 MAR surface mass balance

With a horizontal resolution of 5 kilometers, a single pixel of the MAR v3.14 surface mass balance data already covers an area larger than that of Mittivakkat (see Figure 4.1). Even though the methodology applied in this study only requires the total annual mass balance of a glacier to work, it is obvious that the mass balance at different points of the glacier must vary considerably, at least between the accumulation and ablation areas. Higher resolution surface mass balance data would therefore not just likely increase the accuracy of the overall annual mass balance by better resolving the complex topography of Mittivakkat, but also allow for a more detailed, elevation-binned analysis of the mass balance of the glacier.

So far, there do not seem to be any surface mass balance models available that have a much higher spatial resolution. Through the potential dependence of the surface mass balance of a glacier at a certain point with its elevation, however, it is possible to statistically downscale the surface mass balance to a higher resolution as described for the Regional Atmospheric Climate Model 2 (RACMO 2) by Noël et al. (2016). The methodology of Noël et al. (2016) has also already been applied to the version 3.11 of MAR by (Tedesco et al., 2023) to downscale it from a resolution of 6 km to 100 meters. This downscaled version of MAR is, however, currently not yet available (Ander Bjørk, personal communication, 13th of May, 2024).

### 7.2.3 Digital elevation model

As stated in Chapter 3.4, Mittivakkat has thinned by around 18 meters between 1986 and 2011, a trend which likely has continued since then (Mernild, Knudsen, et al., 2013). Assuming a constant rate of thinning, the same point on Mittivakkat glacier would have seen a thinning of around 28 meters over the course of the study period, while the DEM has remained static for the entire time. As the DEM is constructed from elevation data from 2007 to 2022, it should therefore be expected that the ELA has been underestimated in the early years of the study period, and possibly overestimated in more recent years (Porter et al., 2023).

Compared to the uncertainties and inaccuracies that result from issues such as misclassification and the low temporal resolution of the Landsat data, this is likely not a large source of error, but it is still worth mentioning. In the future it would be best to either use multiple DEMs that represent the elevation at different times or at least try to accommodate for the biases based on the average thinning rates cited in the literature.

## 7.3 Results

This chapter discusses the ELA, AAR, and SMB time series produced in this study as well as their correlation with the local climate of the Ammassalik region. It furthermore investigates the implications of the SMB-AAR regressions and assesses the glacier area and hydrological year length time series.

### 7.3.1 Equilibrium-line altitude (ELA)

The significant positive trend of the ELA confirms that Mittivakkat glacier is melting away, even though the  $R^2$  of the linear regression is quite low. This is likely the result of the high internal variability of the ELA, which makes sense given the fact that it is influenced by multiple factors such as precipitation, temperature, and wind direction. These factors might either cancel each other out, for instance in a high precipitation year with unusually warm summer temperatures where a large amount of snow is accumulated in the winter but then also melts away again in the summer or enhance each other, as might be the case in a high precipitation year, with particularly cool summer temperatures and little snow melt during the ablation season. The fact that temperature and precipitation in the region have an anti-phase relationship as discussed in Chapter 3.3.3 likely only increases the amplitude of ELA fluctuations, as warm years tend to coincide with dry years and vice versa, creating climatological conditions that favor an either particularly high or particularly low accumulation, respectively.

Like in the original time series, the WGMS data also shows a positive trend, albeit a much stronger one. It also has a larger internal variability than the original data with glacier-wide ablation being reported 14 times between 1996 and 2023, something which is never observed in the original time series. One reason for this could be the low temporal resolution of the Landsat data as already discussed in Chapter 7.2.1, another one might be that the WGMS ELA is based on individual stake measurements that do not cover the entirety of the glacier. There could therefore have been years during which a small and remote section of the glacier was still accumulating mass which then was only detected on the satellite imagery and not surveyed in the field. On average, the WGMS ELA is more than 100 meters higher than the original ELA, which could again be a consequence of the low temporal resolution or the fact that the classification algorithm tends to underestimate the ELA height due to misclassified pixels as discussed in Chapter 7.1.1.

### 7.3.2 Accumulation area ratio (AAR)

As for the ELA, the detected negative trend confirms that Mittivakkat glacier is losing mass, even though the high internal variability of the time series is resulting in a low  $R^2$  here as well.

The large fluctuations are likely again the result of the interplay of temperature, precipitation, and wind as already discussed for the ELA in the section above – after all, the two variables are coupled and should in theory have a strictly negative monotonic relationship.

As for the original data, the WGMS time series also shows a negative trend with a very similar slope coefficient. On average, however, the WGMS AAR is 25 percentage points lower than the original AAR, with the mean WGMS AAR being less than half of the original one. This difference is possibly again a result of the classification algorithm misclassifying ice and snow pixels and causing a positive bias in the accumulation area size for the original AAR as discussed in Chapter 7.2.1. As the original AAR is calculated based on the total snow covered area at the end of the ablation season, compared to the WGMS AAR being calculated as the glacier area above the maximum ELA, the methodology used in this study might introduce another positive bias to the AAR calculation as small snow patches below the ELA are included in the accumulation area as well. The low temporal resolution of the Landsat data then likely has the same effect as for the ELA as discussed in Chapter 7.2.1.

### 7.3.3 Surface mass balance (SMB)

Again, the linear regression of SMB against time supports the notion that Mittivakkat glacier is shrinking, and again the SMB displays a large internal variability, likely for the same reasons as the ELA and AAR time series.

Like for the AAR, the slope coefficients for the original and WGMS trends are quite similar, but the average annual loss is almost 500 mm w.eq. larger for the original data compared to the WMGS data. The average absolute difference of 830 mm w.eq. between the two time series lies considerably above the estimated random error for SMB time series calculated from the direct glaciological method of  $\pm 340$  mm w.eq. cited by Zemp et al. (2013), indicating that one or both of the time series have a large bias. As the two time series are calculated based on different start and end dates for each hydrological year (see Table A.1 for original time series dates, WGMS dates unfortunately not reported), a comparison between the two is also filled with inherent uncertainty. One might be able to further investigate how the SMB data sets differ from each other by comparing the SMB at different elevations to determine whether there is a clear elevation-dependent over- or underestimation.

### 7.3.4 ELA, AAR, and SMB in relation to the climate

The ELA is highest in 2012, both for the original and the WGMS time series, even though in the case of the latter one, this year is only one of many maximum ELA years. Consequently, the AAR is also smallest in this year for both time series, which is again unsurprising, given the

relationship between the two variables. The maximum mass loss, however, is not seen in 2012, but either in 2010 for the original data or in 2011 for the WGMS data.

The lowest ELA is observed in 2018 and 2003 for both the original and the WGMS time series and the largest AAR is seen in the years 2003 and 2015, again for both time series. 2015 is also a year of unusually low mass loss for both the original and the WGMS SMB time series, and in 2003 the WGMS mass balance is even reaching its maximum SMB value, whereas it remains at an average value in the original time series.

Based on the relationships between climate and mass balance discussed in Chapter 3.3.3, it would be expected that the years 2010-2012 were high melt years with low precipitation and warm temperatures, and the years 2003 and 2015 were low melt years, with low temperatures and high precipitation. Looking at the temperature and precipitation in Tasiilaq shown in Figure 3.3 it becomes apparent that the period between 2010 and 2012 was indeed characterized by below average precipitation and at least in 2010 and 2012 above average annual temperatures. As for the low melt years, the precipitation in 2003 was not particularly high, but it was the second hottest year in the study period, while the year 2015 had an above average amount of precipitation and average temperatures.

The correlations between ELA, AAR, and SMB and the climate shown in Table 7.1 below generally support the relationships described above, but most correlations are insignificant at the chosen significance level of  $\alpha = 0.05$ . It also seems as though the ELA and AAR are more strongly and significantly correlated with precipitation than with temperature, while at least the original SMB is highly significantly correlated with the temperature. This might indicate that the surface mass balance is more dependent of the annual mean temperature, while the ELA and AAR are more dependent on the amount of precipitation. Overall, the original data is slightly more strongly and significantly correlated with the climate data than the WGMS data.

As the climate at Mittivakkat is influenced by the large-scale weather systems in the North Atlantic discussed in Chapter 3.3.3, the natural next step is to investigate the correlation between the ELA, AAR, and SMB, and the indices of the AMO and NAO directly. The outcomes of this correlation analysis are shown in Table 7.2 below and indicate a clear connection between the ELA, AAR, and SMB for both the original and the WGMS time series and the AMO. The directions of the correlations are the same as for the temperature correlations – unsurprising, given the significant correlation between the two – but are notably stronger and more significant. The correlations with the NAO, on the other hand, are all insignificant, except the one with the original SMB, and share the same direction as the correlations with the precipitation.

**Table 7.1.:** Correlation between ELA, AAR, and SMB and temperature and precipitation at the DMI climate station in Tasiilaq. The correlation coefficient for ELA, AAR, SMB, and SMB (WGMS) is the Pearson correlation coefficient, the correlation coefficient for ELA (WGMS) and AAR (WGMS) is the Kendall  $\tau$  correlation coefficient. Correlations significant at the  $\alpha = 0.05$  significance level are marked in bold font. The time period for the original data is 1985 to 2023 and 1996 to 2023 for the WMGS data.

Time series	Precipitation		Temperature		p-value
	Correlation coefficient	p-value	Correlation coefficient	p-value	
ELA	-0.322	0.0554		0.164	0.3381
AAR	<b>0.382</b>	<b>0.0217</b>		-0.125	0.4675
SMB	0.305	0.0587		<b>-0.522</b>	<b>6E-04</b>
ELA (WGMS)	-0.158	0.2683		0.139	0.3354
AAR (WGMS)	0.143	0.3278		-0.142	0.3372
SMB (WGMS)	0.289	0.1351		-0.196	0.3176

**Table 7.2.:** Correlation between ELA, AAR, and SMB and indices of the AMO and NAO. The correlation coefficient for ELA, AAR, SMB, and SMB (WGMS) is the Pearson correlation coefficient, the correlation coefficient for ELA (WGMS) and AAR (WGMS) is the Kendall  $\tau$  correlation coefficient. Correlations significant at the  $\alpha = 0.05$  significance level are marked in bold font. The time period for the original data is 1985 to 2023 and 1996 to 2023 for the WMGS data.

Time series	AMO Index		NAO Index		p-value
	Correlation coefficient	p-value	Correlation coefficient	p-value	
ELA	<b>-0.400</b>	<b>0.0157</b>		-0.273	0.1072
AAR	<b>-0.395</b>	<b>0.0175</b>		0.257	0.1298
SMB	<b>-0.700</b>	<b>7.03E-07</b>		<b>0.467</b>	<b>0.0027</b>
ELA (WGMS)	<b>0.497</b>	<b>5E-04</b>		-0.170	0.2338
AAR (WGMS)	<b>-0.466</b>	<b>1.4E-03</b>		0.180	0.2173
SMB (WGMS)	<b>-0.477</b>	<b>0.0103</b>		0.363	0.0578

It would therefore appear that the ELA and AAR, as well as the SMB are all strongly influenced by the fluctuations of sea surface temperatures in the North Atlantic as quantified by the AMO index. A positive AMO index corresponds to warmer temperatures and less precipitation, causing the ELA to rise and the AAR and SMB to fall. This relationship holds true for both the original data and the WGMS data and the correlations are comparable in both strength and significance. Surprisingly, the correlations with the AMO directly are in both cases stronger and more significant than with the temperature and precipitation at the DMI station in Tasiilaq, indicating that the climatological differences between Tasiilaq and Mittivakkat might be too large to infer one from the other. This is further supported by the fact that most of the correlations of ELA, AAR, and SMB with the climate data in Tasiilaq are insignificant. Still, a correlation of longer or smoothed time series might paint a different picture.

Contrary to the AMO, the correlations with the NAO index indicate the ELA, AAR, and SMB are not strongly affected by the climate changes quantified by this index. As has already been discussed in Chapter 3.3.3, however, the influence of the NAO is thought to be stronger on the intra- instead of the interannual scale. It would therefore be interesting to investigate the correlations between the different variables on a monthly scale in the future.

### 7.3.5 AAR-SMB regression

While still lying within the bounds of the spread of  $AAR_0$ -values found by Dyurgerov et al. (2009) (0.4 to 0.8), the  $AAR_0$  of 0.74 calculated based on the original data AAR-SMB regression is quite high. This is likely the result of the larger average AAR resulting from the way it is calculated in this study, with small snow patches being included in the accumulation area, biasing it towards larger AAR values.

Compared to this the WGMS  $AAR_0$  of 0.578 is virtually the same as the mean  $AAR_0$  of  $0.579 \pm 0.001$  calculated for a global data set of glacier AAR and mass balance by Dyurgerov et al. (2009). This, together with the fact that the WGMS regression is more significant than the original one and explains 90% of the variance of the data ( $R^2 = 0.90$ ) compared to the 37.2% ( $R^2 = 0.372$ ) of the original data, indicates that the WGMS data and regression more accurately capture the real-world conditions at Mittivakkat glacier. The remarkably high  $R^2$  for the WGMS data might partly be the result of the 14 extreme data points with an AAR of 0 having been removed from the data set, but even when including these, the WGMS regression results in a high  $R^2$  of 0.768 and an  $AAR_0$  of 0.477, which is again closer to the most common  $AAR_0$  value window of 0.5 to 0.6 calculated by Dyurgerov et al. (2009) than the original data. The difference between the original and WGMS  $AAR_0$  is likely also not a result of the different study periods, as illustrated by Figure 6.17, showing that removing the year 1985-1995 results in an even slightly larger  $AAR_0$  of 0.772 for the original data.

The area and volume losses calculated from the two different data sets also vary considerably. The original data regression projects an area loss of 37.5% and a volume loss of 47.6%, whereas the WGMS data regression paints a much darker picture in which Mittivakkat is projected to lose 72.4% of its area and 82.9% of its volume in order to be in equilibrium with the climate again. Even the short-period original regression from 1996-2023 would only lead to projected area and volume losses of 41.7% and 52.4%, respectively, far below the losses based on the WGMS data. With these values, the WGMS projections fall right within the area and mass loss brackets cited by Mernild et al. (2011). This is not surprising, given that the data used by Mernild et al. (2011) is part of the WGMS data set used in this study, but it does confirm that the AAR-SMB relationship has remained stable over the last 13 years. Still, it is important to remember that especially the volume estimate comes with a large degree of uncertainty, as the glaciological area-volume scaling is meant to be applied to a collection of glaciers. This

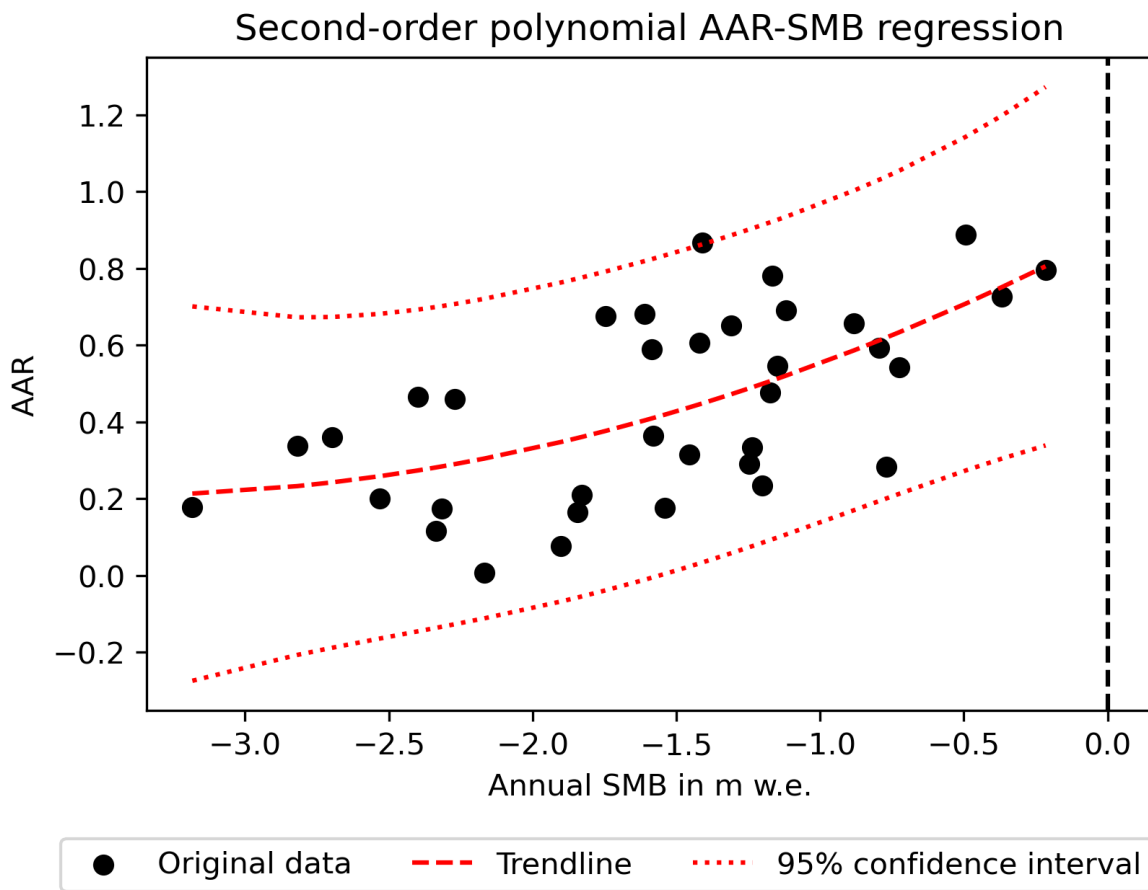


**Figure 7.2:** AAR-SMB second-order polynomial regression for original data.

is why the area and volume adjustment are given without decimal places in the abstract and conclusion chapters. A more robust estimate could be achieved by adjusting the exponential scaling factor  $\gamma$  to the actual area-volume relationship at Mittivakkat.

As mentioned in Chapter 5.1, most glaciers have a linear relationship between the AAR and SMB. Even though the scatterplot of AAR against SMB does seem to indicate a linear relationship for both the original and the WGMS data, a second-order polynomial regression was fitted to the original data to assess this regression model as well. While the regression was also highly significant ( $p\text{-value} < 0.001$ ) with a higher  $R^2$  of 0.377, the corresponding  $AAR_0$  of 0.89 seemed unrealistically high compared to the values cited by Dyurgerov et al. (2009). More importantly, the difference between the two  $AAR_0$  values is smaller than 3 standard deviations of the original data AAR, which is the threshold defined by Dyurgerov et al. (2009) to choose a higher-order polynomial regression over a linear regression. The second-order polynomial regression is shown in Figure 7.2 above.

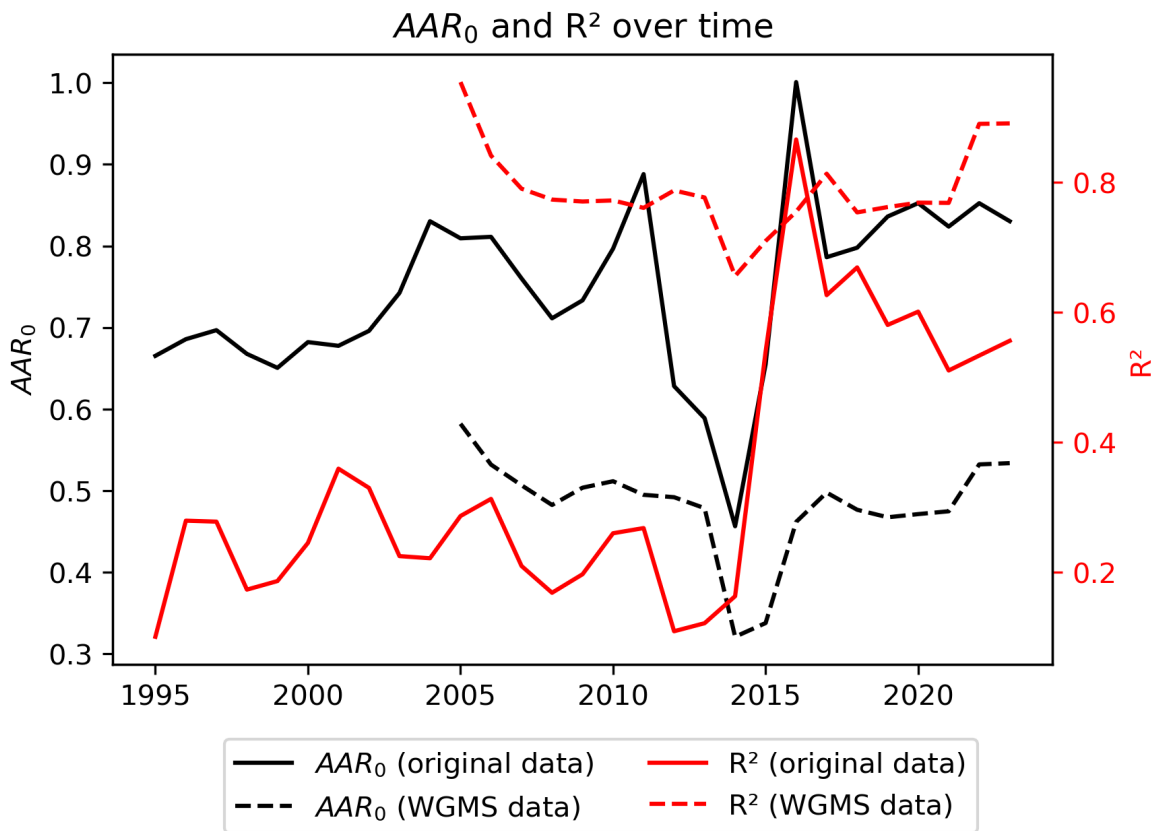


**Figure 7.3.:** Fluctuations of AAR<sub>0</sub> and R<sup>2</sup> from AAR-SMB regressions using a 10-year moving window. The x-axis shows the last year included in each period.

### 7.3.6 AAR<sub>0</sub> fluctuations

As discussed in Chapter 6.6.3 and in the section right above, the difference between the different AAR-SMB regressions likely comes from the differences in annual AAR and SMB values and not from differences in the length of the study periods. Still, the difference in the number of data points might play an important role in changing the outcome of the regression, especially in very short time series as is the case for most of the Greenlandic glaciers with recorded mass balance observation. This chapter therefore investigates the sensitivity of the AAR<sub>0</sub> to a smaller subset of years and its evolution over time. Figure 7.3 above shows the fluctuations of the AAR<sub>0</sub> and the R<sup>2</sup> of the corresponding AAR-SMB regressions when calculated based on a 10-year moving window.

The figure clearly illustrates that the AAR<sub>0</sub> changes dramatically depending on the period used in the regression. The original AAR<sub>0</sub> for instance, jumps from its minimum value of 0.45 in 2014, to its maximum value of 1.00 in 2016 even though the two periods overlap by 8 years. Similarly, the AAR<sub>0</sub> calculated from the WGMS data set varies notably, albeit less extremely: from a maximum of 0.58 in 2005 to a minimum of 0.32 in 2014. The R<sup>2</sup> value also fluctuates, loosely following the two AAR<sub>0</sub> graphs, with high AAR<sub>0</sub> values coinciding with higher R<sup>2</sup> values

and vice versa. With the exception of the extreme values in 2016, the original regression  $R^2$  values are considerably lower than those of the WGMS regressions (original data  $R^2$  mean: 0.34; WGMS data  $R^2$  mean: 0.79), while the original  $AAR_0$  is always larger than that of the WGMS data (original data mean: 0.75; WGMS data mean: 0.48).

While both  $AAR_0$  time series seem to follow a similar temporal pattern – most notably they both show a steep drop towards a minimum value in 2014 and rise again shortly after – they are not significantly correlated ( $p\text{-value} = 0.49$ ). It therefore seems questionable whether the similarities in the time series originate from climate-related fluctuations of the SMB and AAR that are reflected in both data sets as they also might be purely coincidental.

Figures 7.4 and 7.5 below show the AAR-SMB regression for the highest and lowest  $AAR_0$  value for both the original and the WGMS data. Especially the two original regressions show that one or two outliers can completely change the outcome of the regression. It seems that over a period of 10 years the interannual variability is too large to allow for a reliable calculation of the  $AAR_0$ . Whether this issue calls the reliability of the also fairly short WGMS time series (14 years) into question, however, is hard to estimate as even the two most extreme WGMS AAR-SMB regressions are more significant than the full original time series. In the future one should investigate how the  $AAR_0$  fluctuations change based on different moving window sizes in order to determine how long a time series is required for a reliable and representative AAR-SMB regression.

### 7.3.7 Glacier area

While the concept of calculating the glacier area from pixel counts theoretically makes sense, the obvious problem in this case is that it does not account for no-data pixels, distorting the calculated area to a degree at which it becomes unusable. The sharp area drop-off in 2003, for instance, is easily explained by the fact that this is the year in which the Landsat 7 scan line corrector of the ETM+ sensor failed, causing wide gaps of no-data pixels. While this is not an issue before 2003 and after 2013, when Landsat 8 was launched, the masking of clouds also results in an apparent area loss that is not related to any real-world area changes.

Assuming a continuation of the trend cited in Mernild, Knudsen, et al. (2013) from 31.6 km<sup>2</sup> in 1986 to 26.2 km<sup>2</sup> in 2011 (= 0.216 km<sup>2</sup> area loss per year) the current area of the entire glacier complex would be 23.4 km<sup>2</sup>. Scaled to only the main catchment area assuming a uniform mass loss this would result in a current main catchment area of 18.00 km<sup>2</sup>, compared to the 20.15 km<sup>2</sup> in 2011 cited by Mernild, Knudsen, et al. (2013) and 15.19 km<sup>2</sup> based on the pixel count glacier area in 2023. This goes to show that while satellite imagery can be a valuable tool to map glacier area changes, it would either have to be done manually or with a more sophisticated methodology, that takes cloudy pixels and data gaps into account.

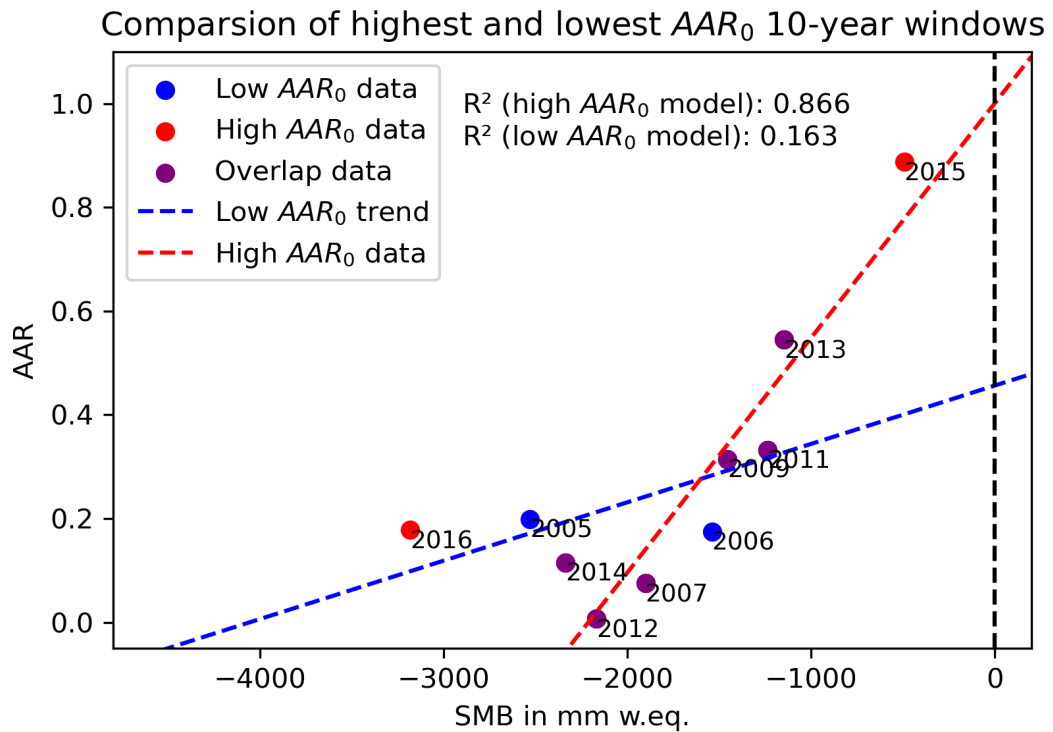


**Figure 7.4.:** AAR-SMB regressions for the highest and lowest  $AAR_0$  of the 10-year moving window analysis for the original data.

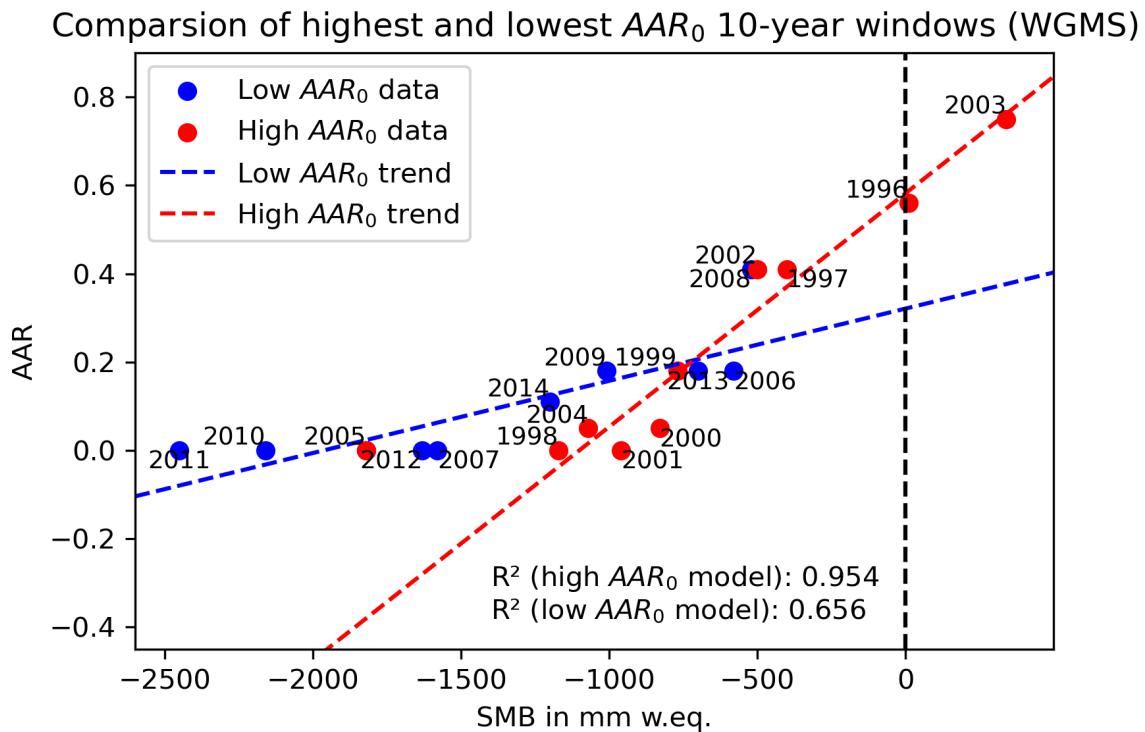


**Figure 7.5.:** AAR-SMB regressions for the highest and lowest  $AAR_0$  of the 10-year moving window analysis for WGMS data.

### 7.3.8 Length of hydrological year

Neither the hydrological year length nor the end of the ablation season show any significant trend. While this is to be expected with the hydrological year – in fact it is hard to imagine how a trend would be at all possible – it seems reasonable to expect a longer and longer ablation season, given the rising temperatures and increasing annual mass loss. Based on the original data this does, however, not seem to be the case. This might be due to two main issues: 1) only the end date of the ablation season is determined, so the season could simply begin earlier in the year and increase in length this way and 2) the end dates of the ablation season are subject to a large uncertainty due to the low temporal resolution of the Landsat data, as further discussed in Chapter 7.2.1.

As already mentioned, no dates for beginning or end of the ablation season or hydrological year are reported in the WGMS data set, but a study by Mernild et al. (2008) found a significant positive trend ( $R^2 = 0.70$ ,  $p\text{-value} < 0.01$ ) of the ablation season length at the station Nunatak from 101 continuous thawing days in 1994 to 151 continuous thawing days in 2006, confirming the expectation that the ablation season is getting longer. Like with the other investigated time series, a higher temporal resolution would be required for reliable results.

## Conclusion

The goal of this study was to develop an automated Python-based tool chain to estimate the committed mass loss of a glacier based on satellite imagery and climate reanalysis surface mass balance data. The tool chain was then to be tested by investigating the committed mass loss of Mittivakkat glacier and comparing it to in-situ observations published by the WGMS.

Overall, the tool chain works as intended and is able to calculate the committed mass loss of Mittivakkat based on the input data. The AAR-SMB regression is significant and the corresponding  $AAR_0$  lies at 0.74, resulting in a fractional imbalance  $\alpha$  of 0.61 based on the time-average AAR of 0.45. Therefore, Mittivakkat is projected to have to lose 39% of its area and 50% of its volume in order to reach an equilibrium with the current climate again.

While the  $AAR_0$  computed with the tool chain described in this study does fall within the interval of realistic  $AAR_0$  values from 0.4 to 0.8 found by Dyurgerov et al. (2009), it is still remarkably high, especially compared to the WGMS data. According to the in-situ observations, the  $AAR_0$  lies at 0.58 with a much lower corresponding fractional imbalance  $\alpha$  of 0.28 based on the time-average WGMS AAR of 0.16. According to the WGMS, Mittivakkat is therefore projected to lose 72% of its area and 83% of its volume – considerably more than estimated in this study.

As the AAR-SMB regression for the WMGS data is more significant and explains a much larger portion of the variance of the data, the WGMS data seems to be more reliable. Given the different sources of uncertainty associated with the methodology applied in this study, this is not surprising. First and foremost, the algorithm used to classify the glacier surface into snow-covered and bare ice pixels is quite obviously not accurate enough. Instead of a simple threshold value, it would be better to use a more advanced classifier such as a Random Forest or Support Vector Machine classifier, or a convolutional neural network. Which of these classifiers is best suited for this application will ultimately depend on the availability of training data and the number of glaciers that is supposed to be investigated – or better the amount of data that must be processed. Another large source of uncertainty is the temporal resolution of the satellite imagery used in the study. Unfortunately, the revisit time of the different Landsat satellites is too long to accurately determine the exact date of the end of the ablation season and with that the corresponding ELA and AAR. There are, however, other satellite-based earth

observation programs that provide more high-resolution data, such as PlanetScope, RapidEye, and Sentinel-2. While these programs lack the long-term archive of Landsat, they offer up to daily temporal resolution, and by combining the data from for instance the RapidEye archive and the on-going PlanetScope program it would be possible to get a time series of 15 years – one year more than currently available for the WGMS regression. It would be especially interesting to compare the results of this analysis with those based on the same analysis with high-resolution satellite imagery and determine whether they differ significantly from each other. Both the low temporal resolution and inaccurate classification likely introduce a positive bias to the AAR calculation, resulting in larger AAR values and with that a larger  $AAR_0$ . This might help to explain why the  $AAR_0$  based on the original data is bigger than that of the WGMS data.

Other ways of increasing the accuracy and reliability of the results include 1) the use of multiple digital elevation models over time to account for glacier thinning when calculating the ELA, 2) downscaling the surface mass balance reanalysis data based on the local relationship between SMB and elevation, and 3) the addition of another algorithm to the tool chain that masks out small snow patches that are not to be included in the calculation of the ELA and AAR.

Despite the large differences between the two data sets, they both project a substantial mass loss for Mittivakkat that is already committed. Even in the absence of future warming, Mittivakkat will shrink to a much smaller size, resulting in serious consequences for both the local ecosystems and the local population in Tasiilaq. As the town's hydropower plant is largely dependent on melt water run-off from Mittivakkat, the energy infrastructure must adept in the long run, as the amount of melt water eventually decreases as the glacier melts away. In addition to this, many of Tasiilaq's inhabitants are working in the tourism industry and continued melt will make the glacier a more risky and likely less attractive tourist destination – not to mention the more and more complicated and unpredictable logistics involved in transport in the area, as the sea ice gets less stable, and the glaciers become more crevassed.

The mass loss trend at Mittivakkat glacier is not an isolated phenomenon. As stated by Mernild, Malmros, et al. (2012), most of the glaciers in the region have been continuously retreating since the 1970s. The fact that 12% of the total projected sea-level rise until 2100 is thought to be contributed by the Greenlandic peripheral glaciers alone, underscores the importance of accurately determining the committed mass loss of these glaciers to quickly adept to the changing climate (Rounce et al., 2023). With only 5 of the estimated 20,000 glaciers having on-going mass balance observation programs, the usefulness of a fully remote methodology for the estimation of the committed mass is obvious.

If the tool chain presented in this thesis is improved in the ways outlined above – most importantly more accurate classification and a higher temporal resolution of the input satellite imagery – it can make a valuable contribution to on-going glacier melt monitoring efforts in

both Greenland and other remote areas and set a solid base of information for policy-making and adaptation strategy planning for the future.

**Acknowledgements:** First and foremost, I would like to thank my supervisors Jason E. Box of GEUS and Rasmus Fensholt of IGN for their guidance, advice, and support over the course of this thesis. Then I would like to thank Anders A. Bjørk for letting me accompany him on a field work trip to the Sermilik research station to see Mittivakkat glacier with my own eyes and for answering all my questions about Mittivakkat, Tasiilaq, and Greenland. Moreover, I would like to thank Signe Hillerup Larsen, for her advice on how to test the sensitivity of the ELA and AAR calculation and for letting me participate in her research projects as well as Anders Svensson for his guidance while trying to pick my study focus that ultimately led me to this thesis. I would also like to thank Bjarne Grønnow for his insights on the cultural significance of glaciers in Greenland, Gyula Mate Kovács for helping me solve the coding issues I had with Google Earth Engine, Xavier Fettweis for the provision of the MAR data sets, and Kristi Sayler for answering my questions about the Landsat program.

**Layout:** The layout of this thesis is based on the  $\text{\LaTeX}$  template *A  $\text{\LaTeX}$  Style for Thesis at UCPH* by Mikkel Roald-Arbøl, available on the [Overleaf website](#). It is in turn based on the *Clean Thesis* style developed by Ricardo Langner available [here](#). I would like to thank both Mikkel and Ricardo for their work on this beautiful style.

**Data availability:** The data generated in this study can be retrieved from a public GitHub repository [here](#). The repository also includes the Python and Google Earth Engine scripts and a short documentation file that should enable anyone to repeat the analysis conducted in this study as well as all produced figures.

## Bibliography

- Allison, E. A. (2015). The spiritual significance of glaciers in an age of climate change. *WIREs Climate Change*, 6(5), 493–508. <https://doi.org/10.1002/wcc.354>
- Aschwanden, A., Fahnestock, M. A., Truffer, M., Brinkerhoff, D. J., Hock, R., Khroulev, C., Mottram, R., & Khan, S. A. (2019). Contribution of the Greenland Ice Sheet to sea level over the next millennium. *Science Advances*, 5(6), eaav9396. <https://doi.org/10.1126/sciadv.aav9396>
- Bahr, D. B., Dyurgerov, M., & Meier, M. F. (2009). Sea-level rise from glaciers and ice caps: A lower bound. *Geophysical Research Letters*, 36(3). <https://doi.org/10.1029/2008GL036309>
- Bahr, D. B., Pfeffer, W. T., & Kaser, G. (2015). A review of volume-area scaling of glaciers. *Reviews of Geophysics*, 53(1), 95–140. <https://doi.org/10.1002/2014RG000470>
- Belgiu, M., & Drăguț, L. (2016). Random forest in remote sensing: A review of applications and future directions. *ISPRS Journal of Photogrammetry and Remote Sensing*, 114, 24–31. <https://doi.org/10.1016/j.isprsjprs.2016.01.011>
- Bhatia, M. P., Kujawinski, E. B., Das, S. B., Breier, C. F., Henderson, P. B., & Charette, M. A. (2013). Greenland meltwater as a significant and potentially bioavailable source of iron to the ocean. *Nature Geoscience*, 6(4), 274–278. <https://doi.org/10.1038/ngeo1746>
- Box, J. E. (2002). Survey of greenland instrumental temperature records: 1873–2001. *International Journal of Climatology*, 22(15), 1829–1847. <https://doi.org/10.1002/joc.852>
- Box, J. E., Hubbard, A., Bahr, D. B., Colgan, W. T., Fettweis, X., Mankoff, K. D., Wehrlé, A., Noël, B., van den Broeke, M. R., Wouters, B., Bjørk, A. A., & Fausto, R. S. (2022). Greenland ice sheet climate disequilibrium and committed sea-level rise. *Nature Climate Change*, 12(9), 808–813. <https://doi.org/10.1038/s41558-022-01441-2>
- Breusch, T. S., & Pagan, A. R. (1979). A Simple Test for Heteroscedasticity and Random Coefficient Variation. *Econometrica*, 47(5), 1287–1294. <https://doi.org/10.2307/1911963>
- Brun, E., David, P., Sudul, M., & Brunot, G. (1992). A numerical model to simulate snow-cover stratigraphy for operational avalanche forecasting. *Journal of Glaciology*, 38(128), 13–22. <https://doi.org/10.3189/S0022143000009552>
- Cappelen, J. (2021). *Greenland – DMI Historical Climate Data Collection 1784-2020*. Danmarks Meteorologiske Institut.

- Chow, D. (2019). *An island imperiled: Climate change threatens Greenland — and its way of life*. NBC News. Retrieved July 19, 2024, from <https://www.nbcnews.com/mach/science/island-imperiled-climate-change-threatens-greenland-its-way-life-ncna1054921>
- Chylek, P., Folland, C. K., Lesins, G., Dubey, M. K., & Wang, M. (2009). Arctic air temperature change amplification and the Atlantic Multidecadal Oscillation. *Geophysical Research Letters*, 36(14). <https://doi.org/10.1029/2009GL038777>
- Copernicus. (2024a). *S2 Mission*. SentiWiki. Retrieved July 31, 2024, from <https://sentiwiki.copernicus.eu/web/s2-mission>
- Copernicus. (2024b). *S2 Products*. SentiWiki. Retrieved July 31, 2024, from <https://sentiwiki.copernicus.eu/web/s2-products>
- Cuffey, K. M., & Paterson, W. S. B. (2010). *The physics of glaciers* (4th ed.). Academic Press.
- Dansk Geologisk Forening. (1961). *Bulletin of the Geological Society of Denmark* (No. 14-4). Dansk Geologisk Forening. Copenhagen.
- Desmet, K., Kopp, R. E., Kulp, S. A., Nagy, D. K., Oppenheimer, M., Rossi-Hansberg, E., & Strauss, B. H. (2021). Evaluating the Economic Cost of Coastal Flooding. *American Economic Journal: Macroeconomics*, 13(2), 444–486.
- DMI. (2024). *Vejrarkiv Tasiilaq*. Lokationarkiv. Retrieved June 21, 2024, from <https://www.dmi.dk/lokationarkiv/show/GL/3424607/Tasiilaq?cHash=1ce21d79cc0770af5dfedbde4878433>
- Durbin, J., & Watson, G. S. (1971). Testing for Serial Correlation in Least Squares Regression. III. *Biometrika*, 58(1), 1–19. <https://doi.org/10.2307/2334313>
- Dyurgerov, M., & Meier, M. F. (2005). *Glaciers and the changing Earth system: A 2004 snapshot*. Institute of Arctic and Alpine Research, University of Colorado, Boulder.
- Dyurgerov, M., Meier, M. F., & Bahr, D. B. (2009). A new index of glacier area change: A tool for glacier monitoring. *Journal of Glaciology*, 55(192), 710–716. <https://doi.org/10.3189/002214309789471030>
- Ellekrog, O. (2023). *Was researching sediment transport – ended up getting cheap electricity for all of Greenland*. Polar Journal. Retrieved July 19, 2024, from <https://polarjournal.ch/en/2023/08/12/was-researching-sediment-transport-ended-up-getting-cheap-electricity-for-all-of-greenland/>
- Ernstsen, V. B. (2013, November 15). *The Sermilik Scientific Research Station*. Department of Geosciences and Natural resource Management. Retrieved June 11, 2024, from <https://ign.ku.dk/english/about/field-stations/sermilik-station/>
- ESA. (2024). *RapidEye - Earth Online*. RapidEye. Retrieved July 31, 2024, from <https://earth.esa.int/eogateway/missions/rapideye>
- Fausto, R. S., Abermann, J., & Ahlstrøm, A. P. (2020). Annual Surface Mass Balance Records (2009–2019) From an Automatic Weather Station on Mittivakkat Glacier, SE Greenland. *Frontiers in Earth Science*, 8. <https://doi.org/10.3389/feart.2020.00251>
- Feng, Q., Liu, J., & Gong, J. (2015). UAV Remote Sensing for Urban Vegetation Mapping Using Random Forest and Texture Analysis. *Remote Sensing*, 7(1), 1074–1094. <https://doi.org/10.3390/rs70101074>

- Fettweis, X., Gallée, H., Lefebvre, F., & van Ypersele, J.-P. (2005). Greenland surface mass balance simulated by a regional climate model and comparison with satellite-derived data in 1990–1991. *Climate Dynamics*, 24(6), 623–640. <https://doi.org/10.1007/s00382-005-0010-y>
- Fettweis, X., Hofer, S., Krebs-Kanzow, U., Amory, C., Aoki, T., Berends, C. J., Born, A., Box, J. E., Delhasse, A., Fujita, K., Gierz, P., Goelzer, H., Hanna, E., Hashimoto, A., Huybrechts, P., Kapsch, M.-L., King, M. D., Kittel, C., Lang, C., ... Zolles, T. (2020). GrSMBMIP: Intercomparison of the modelled 1980–2012 surface mass balance over the Greenland Ice Sheet. *The Cryosphere*, 14(11), 3935–3958. <https://doi.org/10.5194/tc-14-3935-2020>
- Foga, S., Scaramuzza, P. L., Guo, S., Zhu, Z., Dilley, R. D., Beckmann, T., Schmidt, G. L., Dwyer, J. L., Joseph Hughes, M., & Laue, B. (2017). Cloud detection algorithm comparison and validation for operational Landsat data products. *Remote Sensing of Environment*, 194, 379–390. <https://doi.org/10.1016/j.rse.2017.03.026>
- GEUS. (2018). *Hydropower*. Energy Resources. Retrieved July 19, 2024, from <https://eng.geus.dk/energy-resources/hydropower>
- Google Earth Engine. (2023). *Ee.Algorithms.Landsat.simpleCloudScore* | Google Earth Engine. Google for Developers. Retrieved June 19, 2024, from <https://developers.google.com/earth-engine/apidocs/ee-algorithms-landsat-simplecloudscore>
- Gorelick, N., Hancher, M., Dixon, M., Ilyushchenko, S., Thau, D., & Moore, R. (2017). Google Earth Engine: Planetary-scale geospatial analysis for everyone. *Remote Sensing of Environment*, 202, 18–27. <https://doi.org/10.1016/j.rse.2017.06.031>
- Grønnow, B. (2009). Blessings and Horrors of the Interior: Ethno-Historical Studies of Inuit Perceptions Concerning the Inland Region of West Greenland. *Arctic Anthropology*, 46(1-2), 191–201. <https://doi.org/10.1353/arc.0.0027>
- Gutiérrez, M. H., Galand, P. E., Moffat, C., & Pantoja, S. (2015). Melting glacier impacts community structure of Bacteria, Archaea and Fungi in a Chilean Patagonia fjord. *Environmental Microbiology*, 17(10), 3882–3897. <https://doi.org/10.1111/1462-2920.12872>
- Hagg, W. (2022). *Glaciology and Glacial Geomorphology*. Springer. <https://doi.org/10.1007/978-3-662-64714-1>
- Hansche, I., Shahi, S., Abermann, J., & Schöner, W. (2023). The vertical atmospheric structure of the partially glacierised Mittivakkat valley, southeast Greenland. *Journal of Glaciology*, 69(277), 1097–1108. <https://doi.org/10.1017/jog.2022.120>
- Hauer, M. E., Fussell, E., Mueller, V., Burkett, M., Call, M., Abel, K., McLeman, R., & Wrathall, D. (2020). Sea-level rise and human migration. *Nature Reviews Earth & Environment*, 1(1), 28–39. <https://doi.org/10.1038/s43017-019-0002-9>
- Heydari, S. S., & Mountrakis, G. (2019). Meta-analysis of deep neural networks in remote sensing: A comparative study of mono-temporal classification to support vector machines. *ISPRS Journal of Photogrammetry and Remote Sensing*, 152, 192–210. <https://doi.org/10.1016/j.isprsjprs.2019.04.016>

- How, P., Abermann, J., Ahlstrøm, A., Andersen, S., Box, J. E., Citterio, M., Colgan, W., Fausto., R., Karlsson, N., Jakobsen, J., Langley, K., Larsen, S., Lund, M., Mankoff, K., Pedersen, A., Rutishauser, A., Shield, C., Solgaard, A., Van As, D., ... Wright, P. (2022). *PROMICE and GC-Net automated weather station data in Greenland*. GEUS Dataverse. <https://doi.org/10.22008/FK2/IW73UU>
- Hugonnet, R., McNabb, R., Berthier, E., Menounos, B., Nuth, C., Girod, L., Farinotti, D., Huss, M., Dussaillant, I., Brun, F., & Kääb, A. (2021). Accelerated global glacier mass loss in the early twenty-first century. *Nature*, 592(7856), 726–731. <https://doi.org/10.1038/s41586-021-03436-z>
- Huss, M., Bookhagen, B., Huggel, C., Jacobsen, D., Bradley, R., Clague, J., Vuille, M., Buytaert, W., Cayan, D., Greenwood, G., Mark, B., Milner, A., Weingartner, R., & Winder, M. (2017). Toward mountains without permanent snow and ice. *Earth's Future*, 5(5), 418–435. <https://doi.org/10.1002/2016EF000514>
- IGN. (2013, November 18). *History and facilities*. Sermilik Research Station. Retrieved June 11, 2024, from <https://ign.ku.dk/english/about/field-stations/sermilik-station/history-and-facilities/>
- Immerzeel, W. W., Lutz, A. F., Andrade, M., Bahl, A., Biemans, H., Bolch, T., Hyde, S., Brumby, S., Davies, B. J., Elmore, A. C., Emmer, A., Feng, M., Fernández, A., Haritashya, U., Kargel, J. S., Koppes, M., Kraaijenbrink, P. D. A., Kulkarni, A. V., Mayewski, P. A., ... Baillie, J. E. M. (2020). Importance and vulnerability of the world's water towers. *Nature*, 577(7790), 364–369. <https://doi.org/10.1038/s41586-019-1822-y>
- Jacobsen, D., Milner, A. M., Brown, L. E., & Dangles, O. (2012). Biodiversity under threat in glacier-fed river systems. *Nature Climate Change*, 2(5), 361–364. <https://doi.org/10.1038/nclimate1435>
- Jiménez-de-la-Cuesta, D., & Mauritzen, T. (2019). Emergent constraints on Earth's transient and equilibrium response to doubled CO<sub>2</sub> from post-1970s global warming. *Nature Geoscience*, 12(11), 902–905. <https://doi.org/10.1038/s41561-019-0463-y>
- Kääb, A., Winsvold, S. H., Altena, B., Nuth, C., Nagler, T., & Wuite, J. (2016). Glacier Remote Sensing Using Sentinel-2. Part I: Radiometric and Geometric Performance, and Application to Ice Velocity. *Remote Sensing*, 8(7), 598. <https://doi.org/10.3390/rs8070598>
- Kargel, J. S., Ahlstrøm, A. P., Alley, R. B., Bamber, J. L., Benham, T. J., Box, J. E., Chen, C., Christoffersen, P., Citterio, M., Cogley, J. G., Jiskoot, H., Leonard, G. J., Morin, P., Scambos, T., Sheldon, T., & Willis, I. (2012). Brief communication <br> Greenland's shrinking ice cover: "fast times" but not that fast. *The Cryosphere*, 6(3), 533–537. <https://doi.org/10.5194/tc-6-533-2012>
- Khatami, R., Mountrakis, G., & Stehman, S. V. (2016). A meta-analysis of remote sensing research on supervised pixel-based land-cover image classification processes: General guidelines for practitioners and future research. *Remote Sensing of Environment*, 177, 89–100. <https://doi.org/10.1016/j.rse.2016.02.028>

- Knudsen, N. T., & Hasholt, B. (1999). Radio-echo Sounding at the Mittivakkat Gletscher, Southeast Greenland. *Arctic, Antarctic, and Alpine Research*, 31(3), 321–328. <https://doi.org/10.1080/15230430.1999.12003315>
- Knudsen, N. T., & Hasholt, B. (2004). Mass balance observations at Mittivakkat Gletscher, Southeast Greenland 1995–2002. *Hydrology Research*, 35(4-5), 381–390. <https://doi.org/10.2166/nh.2004.0029>
- Knudsen, N. T., & Hasholt, B. (2008). Mass balance observations at Mittivakkat Glacier, Ammassalik Island, Southeast Greenland 1995–2006. *Geografisk Tidsskrift-Danish Journal of Geography*, 108(1), 111–120. <https://doi.org/10.1080/00167223.2008.10649577>
- Kondo, K., Sakakibara, D., Fukumoto, S., & Sugiyama, S. (2019). Meltwater discharge and flooding of the outlet stream of Qaanaaq Glacier, northwestern Greenland. *Geophysical Research Letters*, 21, 1.
- Lazarowska, A. (2020). Comparison of discrete artificial potential field algorithm and wave-front algorithm for autonomous ship trajectory planning. *IEEE Access*, 8, 221013–221026. <https://doi.org/10.1109/ACCESS.2020.3043539>
- Lydersen, C., Assmy, P., Falk-Petersen, S., Kohler, J., Kovacs, K. M., Reigstad, M., Steen, H., Strøm, H., Sundfjord, A., Varpe, Ø., Walczowski, W., Weslawski, J. M., & Zajaczkowski, M. (2014). The importance of tidewater glaciers for marine mammals and seabirds in Svalbard, Norway. *Journal of Marine Systems*, 129, 452–471. <https://doi.org/10.1016/j.jmarsys.2013.09.006>
- Machguth, H., Thomsen, H. H., Weidick, A., Ahlstrøm, A. P., Abermann, J., Andersen, M. L., Andersen, S. B., Bjørk, A. A., Box, J. E., Braithwaite, R. J., Bøggild, C. E., Citterio, M., Clement, P., Colgan, W., Fausto, R. S., Gleie, K., Gubler, S., Hasholt, B., Hynek, B., ... Wal, R. S. W. V. D. (2016). Greenland surface mass-balance observations from the ice-sheet ablation area and local glaciers. *Journal of Glaciology*, 62(235), 861–887. <https://doi.org/10.1017/jog.2016.75>
- Marzeion, B., Hock, R., Anderson, B., Bliss, A., Champollion, N., Fujita, K., Huss, M., Immerzeel, W. W., Kraaijenbrink, P., Malles, J.-H., Maussion, F., Radić, V., Rounce, D. R., Sakai, A., Shannon, S., van de Wal, R., & Zekollari, H. (2020). Partitioning the Uncertainty of Ensemble Projections of Global Glacier Mass Change. *Earth's Future*, 8(7), e2019EF001470. <https://doi.org/10.1029/2019EF001470>
- Mernild, S. H., Knudsen, N. T., Lipscomb, W. H., Yde, J. C., Malmros, J. K., Hasholt, B., & Jakobsen, B. H. (2011). Increasing mass loss from Greenland's Mittivakkat Gletscher. *The Cryosphere*, 5(2), 341–348. <https://doi.org/10.5194/tc-5-341-2011>
- Mernild, S. H., Malmros, J. K., Yde, J. C., & Knudsen, N. T. (2012). Multi-decadal marine- and land-terminating glacier recession in the Ammassalik region, southeast Greenland. *The Cryosphere*, 6(3), 625–639. <https://doi.org/10.5194/tc-6-625-2012>
- Mernild, S. H., Beckerman, A. P., Knudsen, N. T., Hasholt, B., & Yde, J. C. (2018). Statistical EOF analysis of spatiotemporal glacier mass-balance variability: A case study of Mittivakkat Gletscher, SE Greenland. *Geografisk Tidsskrift-Danish Journal of Geography*.

- Mernild, S. H., Hansen, B. U., Jakobsen, B. H., & Hasholt, B. (2008). Climatic conditions at the Mittivakkat Glacier catchment (1994–2006), Ammassalik Island, SE Greenland, and in a 109-year perspective (1898–2006). *Geografisk Tidsskrift-Danish Journal of Geography*, 108(1), 51–72. <https://doi.org/10.1080/00167223.2008.10649574>
- Mernild, S. H., Knudsen, N. T., Hoffman, M. J., Yde, J. C., Hanna, E., Lipscomb, W. H., Malmros, J. K., & Fausto, R. S. (2013). Volume and velocity changes at Mittivakkat Gletscher, southeast Greenland. *Journal of Glaciology*, 59(216), 660–670. <https://doi.org/10.3189/2013JoG13J017>
- Mernild, S. H., Liston, G. E., Hasholt, B., & Knudsen, N. T. (2006). Snow Distribution and Melt Modeling for Mittivakkat Glacier, Ammassalik Island, Southeast Greenland. *Journal of Hydrometeorology*, 7(4), 808–824. <https://doi.org/10.1175/JHM522.1>
- Mernild, S. H., Pelto, M., Malmros, J. K., Yde, J. C., Knudsen, N. T., & Hanna, E. (2013). Identification of snow ablation rate, ELA, AAR and net mass balance using transient snowline variations on two Arctic glaciers. *Journal of Glaciology*, 59(216), 649–659. <https://doi.org/10.3189/2013JoG12J221>
- Mernild, S. H., Seidenkrantz, M.-S., Chylek, P., Liston, G. E., & Hasholt, B. (2012). Climate-driven fluctuations in freshwater flux to Sermilik Fjord, East Greenland, during the last 4000 years. *The Holocene*, 22(2), 155–164. <https://doi.org/10.1177/0959683611431215>
- Milner, A. M., Khamis, K., Battin, T. J., Brittain, J. E., Barrand, N. E., Füreder, L., Cauvy-Fraunié, S., Gíslason, G. M., Jacobsen, D., Hannah, D. M., Hodson, A. J., Hood, E., Lencioni, V., Ólafsson, J. S., Robinson, C. T., Tranter, M., & Brown, L. E. (2017). Glacier shrinkage driving global changes in downstream systems. *Proceedings of the National Academy of Sciences*, 114(37), 9770–9778. <https://doi.org/10.1073/pnas.1619807114>
- Mouginot, J., Rignot, E., Bjørk, A. A., van den Broeke, M., Millan, R., Morlighem, M., Noël, B., Scheuchl, B., & Wood, M. (2019). Forty-six years of Greenland Ice Sheet mass balance from 1972 to 2018. *Proceedings of the National Academy of Sciences*, 116(19), 9239–9244. <https://doi.org/10.1073/pnas.1904242116>
- Mountrakis, G., Im, J., & Ogole, C. (2011). Support vector machines in remote sensing: A review. *ISPRS Journal of Photogrammetry and Remote Sensing*, 66(3), 247–259. <https://doi.org/10.1016/j.isprsjprs.2010.11.001>
- Musilova, M., Tranter, M., Wadham, J., Telling, J., Tedstone, A., & Anesio, A. M. (2017). Microbially driven export of labile organic carbon from the Greenland ice sheet. *Nature Geoscience*, 10(5), 360–365. <https://doi.org/10.1038/ngeo2920>
- NASA. (2021a, November 30). *Enhanced Thematic Mapper Plus (ETM+)*. Landsat Science. Retrieved June 10, 2024, from <https://landsat.gsfc.nasa.gov/etm-plus/>
- NASA. (2021b, November 30). *Landsat 4*. Landsat Science. Retrieved June 19, 2024, from <https://landsat.gsfc.nasa.gov/satellites/landsat-4/>
- NASA. (2021c, November 30). *Landsat 5*. Landsat Science. Retrieved June 10, 2024, from <https://landsat.gsfc.nasa.gov/satellites/landsat-5/>
- NASA. (2021d, November 30). *Landsat 6*. Landsat Science. Retrieved June 10, 2024, from <https://landsat.gsfc.nasa.gov/satellites/landsat-6/>

- NASA. (2021e, November 30). *Landsat 7*. Landsat Science. Retrieved June 10, 2024, from <https://landsat.gsfc.nasa.gov/satellites/landsat-7/>
- NASA. (2021f, November 30). *Landsat 8*. Landsat Science. Retrieved June 10, 2024, from <https://landsat.gsfc.nasa.gov/satellites/landsat-8/>
- NASA. (2021g, November 30). *Landsat 8 Bands*. Landsat Science. Retrieved June 10, 2024, from <https://landsat.gsfc.nasa.gov/satellites/landsat-8/landsat-8-bands/>
- NASA. (2021h, November 30). *Landsat 8 Mission Details*. Landsat Science. Retrieved June 27, 2024, from <https://landsat.gsfc.nasa.gov/satellites/landsat-8/landsat-8-mission-details/>
- NASA. (2021i, November 30). *Landsat 9*. Landsat Science. Retrieved June 10, 2024, from <https://landsat.gsfc.nasa.gov/satellites/landsat-9/>
- NASA. (2021j, November 30). *Thematic Mapper (TM)*. Landsat Science. Retrieved June 10, 2024, from <https://landsat.gsfc.nasa.gov/thematic-mapper/>
- NASA. (2024). *What's the difference between glacier or ice sheet surface mass balance and total mass balance?* NASA Science. Retrieved July 7, 2024, from <https://science.nasa.gov/climate-change/faq/whats-the-difference-between-glacier-or-ice-sheet-surface-mass-balance-and-total-mass-balance>
- Nicholls, R. J., Marinova, N., Lowe, J. A., Brown, S., Vellinga, P., de Gusmão, D., Hinkel, J., & Tol, R. S. J. (2011). Sea-level rise and its possible impacts given a 'beyond 4°C world' in the twenty-first century. *Philosophical Transactions of the Royal Society A: Mathematical, Physical and Engineering Sciences*, 369(1934), 161–181. <https://doi.org/10.1098/rsta.2010.0291>
- NOAA. (2023). *Atlantic Multidecadal Oscillation (AMO)*. OOPC - The state of the ocean climate. Retrieved June 12, 2024, from <https://stateoftheocean.osmc.noaa.gov/atm/amo.php>
- NOAA. (2024). *North Atlantic Oscillation (NAO)*. Climate Monitoring. Retrieved June 12, 2024, from <https://www.ncei.noaa.gov/access/monitoring/nao/>
- Noël, B., van de Berg, W. J., Machguth, H., Lhermitte, S., Howat, I., Fettweis, X., & van den Broeke, M. R. (2016). A daily, 1 km resolution data set of downscaled Greenland ice sheet surface mass balance (1958–2015). *The Cryosphere*, 10(5), 2361–2377. <https://doi.org/10.5194/tc-10-2361-2016>
- Overeem, I., Hudson, B. D., Syvitski, J. P. M., Mikkelsen, A. B., Hasholt, B., van den Broeke, M. R., Noël, B. P. Y., & Morlighem, M. (2017). Substantial export of suspended sediment to the global oceans from glacial erosion in Greenland. *Nature Geoscience*, 10(11), 859–863. <https://doi.org/10.1038/ngeo3046>
- Planet. (2024a, March 18). *PlanetScope*. Planet Developers. Retrieved July 31, 2024, from <https://developers.planet.com/docs/data/planetscope/>
- Planet. (2024b, July 12). *RapidEye*. Planet Developers. Retrieved July 31, 2024, from <https://developers.planet.com/docs/data/rapideye/>
- Planet. (2024c). *Satellite Imagery and Monitoring*. Planet Monitoring. Retrieved June 20, 2024, from <https://www.planet.com/products/satellite-monitoring/>

- Porter, C., Howat, I., Noh, M.-J., Husby, E., Khuvis, S., Danish, E., Tomko, K., Gardiner, J., Negrete, A., Yadav, B., Klassen, J., Kelleher, C., Cloutier, M., Bakker, J., Enos, J., Arnold, G., Bauer, G., & Morin, P. (2023, August 7). *ArcticDEM - Mosaics, Version 4.1*. Harvard Dataverse. <https://doi.org/10.7910/DVN/3VDC4W>
- Python Software Foundation. (2024). *Python Release 3.12.3*. Python.org. Retrieved June 28, 2024, from <https://www.python.org/downloads/release/python-3123/>
- Rantanen, M., Karpechko, A. Y., Lipponen, A., Nordling, K., Hyvärinen, O., Ruosteenoja, K., Vihma, T., & Laaksonen, A. (2022). The Arctic has warmed nearly four times faster than the globe since 1979. *Communications Earth & Environment*, 3(1), 1–10. <https://doi.org/10.1038/s43247-022-00498-3>
- Rastner, P., Bolch, T., Mölg, N., Machguth, H., Le Bris, R., & Paul, F. (2012). The first complete inventory of the local glaciers and ice caps on Greenland. *The Cryosphere*, 6(6), 1483–1495. <https://doi.org/10.5194/tc-6-1483-2012>
- RGI Consortium. (2017). *Randolph Glacier Inventory - A Dataset of Global Glacier Outlines, Version 6* (Version 6). Boulder, Colorado, USA, National Snow and Ice Data Center. <https://doi.org/10.7265/4m1f-gd79>
- Rounce, D. R., Hock, R., Maussion, F., Hugonnet, R., Kochtitzky, W., Huss, M., Berthier, E., Brinkerhoff, D., Compagno, L., Copland, L., Farinotti, D., Menounos, B., & McNabb, R. W. (2023). Global glacier change in the 21st century: Every increase in temperature matters. *Science*, 379(6627), 78–83. <https://doi.org/10.1126/science.abo1324>
- Sayler, K. (2021). *Landsat 4-7 Collection 2 (C2) Level 2 Science Product (L2SP) Guide Version 4.0*. USGS. Sioux Falls, South Dakota.
- Sayler, K. (2024). *Landsat 8-9 Collection 2 (C2) Level 2 Science Product (L2SP) Guide Version 6.0*. USGS. Sioux Falls, South Dakota.
- Shapiro, S. S., & Wilk, M. B. (1965). An analysis of variance test for normality (complete samples). *Biometrika*, 52(3-4), 591–611. <https://doi.org/10.1093/biomet/52.3-4.591>
- Sugiyama, S., Kanna, N., Sakakibara, D., Ando, T., Asaji, I., Kondo, K., Wang, Y., Fujishi, Y., Fukumoto, S., Podolskiy, E., Fukamachi, Y., Takahashi, M., Matoba, S., Iizuka, Y., Greve, R., Furuya, M., Tateyama, K., Watanabe, T., Yamasaki, S., ... Oshima, T. (2021). Rapidly changing glaciers, ocean and coastal environments, and their impact on human society in the Qaanaaq region, northwestern Greenland. *Polar Science*, 27, 100632. <https://doi.org/10.1016/j.polar.2020.100632>
- Tedesco, M., Colosio, P., Fettweis, X., & Cervone, G. (2023). A computationally efficient statistically downscaled 100m resolution Greenland product from the regional climate model MAR. *The Cryosphere*, 17(12), 5061–5074. <https://doi.org/10.5194/tc-17-5061-2023>
- The National Science Foundation. (2022, January). *Modèle Atmosphérique Régional (MAR) version 3.11 regional climate model output, 1979-2019, Greenland domain, 10 kilometer (km) horizontal resolution*. National Science Foundation (NSF) Public Access. Retrieved June 18, 2024, from <https://par.nsf.gov/biblio/10488581-modele-atmospherique->

- regional-mar-version-regional-climate-model-output-greenland-domain-kilometer-km-horizontal-resolution
- Trias-Sanz, R., Stamon, G., & Louchet, J. (2008). Using colour, texture, and hierarchical segmentation for high-resolution remote sensing. *ISPRS Journal of Photogrammetry and Remote Sensing*, 63(2), 156–168. <https://doi.org/10.1016/j.isprsjprs.2007.08.005>
- UNESCO International Union for Conservation of Nature and Natural Resources. (2022). *World Heritage Glaciers - Sentinels of climate change*. United Nations Educational, Scientific, and Cultural Organization. Gland, Switzerland.
- University of Minnesota. (2024). *ArcticDEM*. Polar Geospatial Center. Retrieved June 19, 2024, from <https://www.pgc.umn.edu/data/arcticdem/>
- USGS (Ed.). (2017). *Landsat Collections — What are Tiers?* [Video].
- USGS. (2021). *How do I use a scale factor with Landsat Level-2 science products?* Science Technology. Retrieved June 28, 2024, from <https://www.usgs.gov/faqs/how-do-i-use-a-scale-factor-landsat-level-2-science-products>
- USGS. (2022a). *CFMask Algorithm*. Landsat Missions. Retrieved June 7, 2024, from <https://www.usgs.gov/landsat-missions/cfmask-algorithm>
- USGS. (2022b). *Landsat Collection 2*. Landsat Missions. Retrieved July 8, 2024, from <https://www.usgs.gov/landsat-missions/landsat-collection-2>
- USGS. (2023). *What is the Landsat satellite program and why is it important?* USGS FAQ. Retrieved June 19, 2024, from <https://www.usgs.gov/faqs/what-landsat-satellite-program-and-why-it-important>
- USGS. (2024a). *EarthExplorer Search*. EarthExplorer. Retrieved June 28, 2024, from <https://earthexplorer.usgs.gov/>
- USGS. (2024b). *Landsat Collection 2 Level-2 Science Products*. Landsat Missions. Retrieved July 8, 2024, from <https://www.usgs.gov/landsat-missions/landsat-collection-2-level-2-science-products>
- USGS. (2024c). *Landsat Collection 2 Surface Reflectance*. Landsat Missions. Retrieved June 10, 2024, from <https://www.usgs.gov/landsat-missions/landsat-collection-2-surface-reflectance>
- Wang, M., & Overland, J. E. (2004). Detecting Arctic Climate Change Using Köppen Climate Classification. *Climatic Change*, 67(1), 43–62. <https://doi.org/10.1007/s10584-004-4786-2>
- Wang, S.-J., & Zhou, L.-Y. (2019). Integrated impacts of climate change on glacier tourism. *Advances in Climate Change Research*, 10(2), 71–79. <https://doi.org/10.1016/j.accre.2019.06.006>
- WGMS. (2017). *Global Glacier Change Bulletin (2014-2015)* (Zemp, M., S. U. Nussbaumer, I. Gärtner-Roer, J. Huber, H. Machguth, F. Paul, & M. Hoelze, Eds.; No. 2). World Glacier Monitoring Service (WGMS). Zurich.
- WGMS. (2024). *Fluctuations of Glaciers Database* (Version 2024-01). Switzerland, World Glacier Monitoring Service. <https://doi.org/10.5904/wgms-fog-2024-01>

Zemp, M., Thibert, E., Huss, M., Stumm, D., Rolstad Denby, C., Nuth, C., Nussbaumer, S. U., Moholdt, G., Mercer, A., Mayer, C., Joerg, P. C., Jansson, P., Hynek, B., Fischer, A., Escher-Vetter, H., Elvehøy, H., & Andreassen, L. M. (2013). Uncertainties and re-analysis of glacier mass balance measurements. *The Cryosphere*, 7, 1227–1245. <https://doi.org/10.5194/tcd-7-789-2013>

# A

## Data

This appendix gives an overview of the ELA, AAR, and SMB data calculated in this study as well as the corresponding data cited by the WGMS (2024) in Tables A.1 and A.2. Tables A.3, A.4, A.5 and A.6 include data on the statistical significance and coefficients of the discussed regressions and Tables A.7, A.8, A.9 and A.10 give an overview of the correlations between the various investigated time series.

**Table A.1.:** Original data overview table.

Year	ELA (m a.s.l.)	AAR	SMB (mm w.eq.)	Hydrological year (days)	Accumulation area (km <sup>2</sup> )	Ablation area (km <sup>2</sup> )
1985	607.2	0.726	-366.7	349	14.60	5.52
1986	639.8	0.594	-794.6	384	11.93	8.17
1987	595.3	0.795	-215.6	343	16.02	4.12
1988	637.0	0.606	-1420.6	370	12.15	7.90
1989	703.4	0.283	-768.7	336	5.69	14.41
1990	634.1	0.676	-1746.5	368	13.61	6.54
1991	653.7	0.651	-1310.0	391	13.11	7.03
1992	614.2	0.704	316.6	377	14.17	5.97
1993	714.4	0.290	-1245.4	375	5.79	14.20
1994			-699.1	359		
1995	758.2	0.173	-2316.7	345	3.44	16.41
1996	600.5	0.657	-883.6	359	13.24	6.90
1997	592.4	0.691	-1118.7	354	13.83	6.20
1998	649.5	0.460	-2271.2	407	9.24	10.86
1999	730.4	0.233	-1200.5	344	4.53	14.86
2000	657.3	0.543	-723.4	352	10.86	9.15
2001	598.6	0.780	-1165.6	352	15.70	4.42
2002	634.6	0.590	-1585.9	368	11.80	8.21
2003	623.3	0.867	-1409.6	368	14.84	2.28
2004	704.4	0.338	-2819.0	384	5.72	11.21
2005	695.0	0.199	-2532.0	368	3.37	13.53
2006	773.5	0.175	-1539.3	368	2.89	13.62
2007	799.9	0.075	-1901.5	352	1.25	15.35
2008			-2428.5	393		
2009	715.0	0.315	-1456.1	359	5.32	11.58
2010			-3475.9	371		
2011	594.5	0.333	-1235.6	333	5.74	11.52
2012	833.0	0.007	-2167.7	368	0.10	15.40
2013	642.7	0.545	-1148.4	368	9.62	8.02
2014	772.2	0.115	-2336.5	369	2.06	15.79
2015	639.1	0.888	-492.9	350	17.46	2.21
2016	754.9	0.178	-3183.6	400	3.17	14.61
2017	691.9	0.476	-1172.6	352	8.92	9.84
2018	577.0	0.681	-1611.4	386	12.70	5.96
2019	715.2	0.363	-1580.0	327	6.79	11.94
2020	708.5	0.465	-2398.5	377	8.51	9.81
2021	675.0	0.360	-2697.3	382	6.26	11.11
2022	711.4	0.210	-1828.1	369	3.29	12.39
2023	773.5	0.165	-1844.7	351	2.50	12.69
<b>Mean</b>	<b>678.4</b>	<b>0.450</b>	<b>-1558.3</b>	<b>365</b>	<b>8.62</b>	<b>9.99</b>

**Table A.2.:** WGMS data overview table.

Year	ELA (m a.s.l.)	AAR	SMB (mm w.eq.)
1996	500	0.56	10
1997	590	0.41	-400
1998	930	0	-1170
1999	740	0.18	-770
2000	650	0.05	-830
2001	930	0	-960
2002	620	0.41	-500
2003	390	0.75	340
2004	850	0.05	-1070
2005	930	0	-1820
2006	680	0.18	-580
2007	930	0	-1580
2008	600	0.41	-520
2009	690	0.18	-1010
2010	930	0	-2160
2011	930	0	-2450
2012	930	0	-1630
2013	700	0.18	-700
2014	750	0.11	-1200
2015	450	0.71	200
2017	930	0	-1150
2018	600	0.41	-360
2019	900	0	-1640
2020	930	0	-1390
2021	930	0	-1720
2022	930	0	-1450
2023	930	0	-1452
Mean	778.6	0.164	-1061.7

**Table A.3.:** Regressions overview table for original data. All regressions are significant at the chosen significance level  $\alpha=0.05$ . The large condition numbers are a result of the large difference between the orders of magnitude of the data sets and should therefore not be an issue.

Statistic	ELA	AAR	SMB	AAR-SMB
R <sup>2</sup>	0.15	0.154	0.258	0.372
Adjusted R <sup>2</sup>	0.125	0.129	0.238	0.354
F-statistic probability	0.0197	0.0181	9.65E-04	7.83E-05
Slope coefficient	2.21	-8.20E-03	-36.89	1.94E-04
p-value (slope)	0.02	0.018	1.00E-03	0
Offset coefficient	-3.75E+03	16.89	7.24E+04	0.7418
p-value (offset)	0.046	0.015	1.00E-03	0
Condition number	3.48E+05	3.48E+05	3.75E+05	3.74E+03

**Table A.4.:** Regressions overview table for WGMS data. All regressions are significant at the chosen significance level  $\alpha=0.05$  with the exception of the AAR. The large condition numbers are a result of the large difference between the orders of magnitude of the data sets and should therefore not be an issue.

Statistic	ELA	AAR	SMB	AAR-SMB
R <sup>2</sup>	0.153	0.098	0.16	0.9
Adjusted R <sup>2</sup>	0.12	0.063	0.128	0.892
F-statistic probability	0.0399	0.105	0.035	2.32E-07
Slope coefficient	8.28	-8.80E-03	-33.44	4.74E-04
p-value (slope)	0.04	0.105	0.035	0
Offset coefficient	-1.59E+04	17.87	6.61E+04	0.5783
p-value (offset)	0.049	0.102	0.038	0
Condition number	5.00E+05	5.00E+05	5.00E+05	1.07E+03

**Table A.5.:** Regressions overview table for length of hydrological year, melt season end, and total glacier area. Only the glacier area regression is significant at the chosen significance level  $\alpha=0.05$ . The large condition numbers are a result of the large difference between orders of the magnitude of the data sets and should therefore not be an issue.

Statistic	Hydrological year	Melt season end	Glacier area
R <sup>2</sup>	3.00E-03	2.00E-03	0.502
Adjusted R <sup>2</sup>	-0.024	-0.027	0.488
F-statistic probability	0.755	0.07192	1.32E-06
Slope coefficient	0.0828	0.0574	-0.0977
p-value (slope)	0.755	0.268	0
Offset coefficient	198.9	122.87	214.47
p-value (offset)	0.708	0.286	0
Condition number	3.57E+05	3.48E+05	3.48E+05

**Table A.6.:** Regressions overview table for the DMI temperature and precipitation as well as the temperature at station Glacier. Only the DMI temperature regression is significant at the chosen significance level  $\alpha=0.05$ . The large condition numbers are a result of the large difference between the orders of magnitude of the data sets and should therefore not be an issue.

Statistic	DMI Temperature	DMI Precipitation	Station Glacier Temperature
R <sup>2</sup>	0.387	1.00E-03	0
Adjusted R <sup>2</sup>	0.37	-0.026	-0.091
F-statistic probability	2.39E-05	0.844	0.99
Slope coefficient	0.0494	-0.6127	-7.00E-04
p-value (slope)	0	0.844	0.99
Offset coefficient	-99.4415	2.10E+03	-1.18
p-value (offset)	0	0.737	0.992
Condition number	3.57E+05	3.57E+05	1.09E+06

**Table A.7.:** Correlation overview table for the ELA, AAR, and SMB original data against their WGMS equivalent and for the SMB against the length of the hydrological year. All correlations are significant at the chosen significance level  $\alpha=0.05$  except for the ELA - ELA (WGMS) correlation.

Data sets	Period	Correlation coefficient	p-value
ELA - ELA (WGMS)	1996-2023	0.284	0.0594
ELA - ELA (WGMS) (AAR > 0)	1996-2023	0.487	0.0216
AAR - AAR (WGMS)	1996-2023	0.424	6.10E-03
AAR - AAR (WGMS) (AAR > 0)	1996-2023	0.632	4.00E-03
SMB - SMB (WGMS)	1996-2023	0.566	3.20E-03
SMB - length of hydrological year	1985-2023	-0.443	4.80E-03

**Table A.8.:** Correlation overview table for various climate time series with the AMO and NAO indices. All correlations that are significant at the chosen significance level  $\alpha=0.05$  are marked in bold font.

Data sets	Period	Correlation coefficient	p-value
Tasiilaq temperature - AMO	1985-2023	<b>0.635</b>	<b>1.43E-05</b>
Tasiilaq temperature - NAO	1985-2023	<b>-0.393</b>	<b>0.0133</b>
Tasiilaq precipitation - AMO	1985-2023	-0.117	0.4795
Tasiilaq precipitation-AMO	1958-2023	<b>-0.334</b>	<b>6.10E-03</b>
Tasiilaq precipitation - NAO	1985-2023	0.209	0.2094
Station Glacier - AMO	2010-2022	0.328	0.2734
Station Glacier - NAO	2010-2022	-0.473	0.1028
Station Glacier - AMO (monthly)	2010-2022	<b>0.377</b>	<b>1.41E-06</b>
Station Glacier - NAO (monthly)	2010-2022	<b>-0.268</b>	<b>8.00E-04</b>
Tasiilaq temperature - precipitation (raw)	1958-2023	-0.082	0.5133
Tasiilaq temperature - precipitation (10-year mean)	1958-2023	<b>-0.788</b>	<b>5.79E-13</b>

**Table A.9.:** Correlation between ELA, AAR, and SMB and temperature and precipitation at the DMI climate station in Tasiilaq. The correlation coefficient for ELA, AAR, SMB, and SMB (WGMS) is the Pearson correlation coefficient, the correlation coefficient for ELA (WGMS) and AAR (WGMS) is the Kendall  $\tau$  correlation coefficient. Correlations significant at the  $\alpha = 0.05$  significance level are marked in bold font. The time period for the original data is 1985 to 2023 and 1996 to 2023 for the WMGS data.

Time series	Precipitation		Temperature		
	Correlation coefficient	p-value	Correlation coefficient	p-value	
ELA	-0.322	0.0554		0.164	0.3381
AAR	<b>0.382</b>	<b>0.0217</b>		-0.125	0.4675
SMB	0.305	0.0587		<b>-0.522</b>	<b>6E-04</b>
ELA (WGMS)	-0.158	0.2683		0.139	0.3354
AAR (WGMS)	0.143	0.3278		-0.142	0.3372
SMB (WGMS)	0.289	0.1351		-0.196	0.3176

**Table A.10.:** Correlation between ELA, AAR, and SMB and indices of the AMO and NAO. The correlation coefficient for ELA, AAR, SMB, and SMB (WGMS) is the Pearson correlation coefficient, the correlation coefficient for ELA (WGMS) and AAR (WGMS) is the Kendall  $\tau$  correlation coefficient. Correlations significant at the  $\alpha = 0.05$  significance level are marked in bold font. The time period for the original data is 1985 to 2023 and 1996 to 2023 for the WMGS data.

Time series	AMO Index		NAO Index	
	Correlation coefficient	p-value	Correlation coefficient	p-value
ELA	<b>-0.400</b>	<b>0.0157</b>	-0.273	0.1072
AAR	<b>-0.395</b>	<b>0.0175</b>	0.257	0.1298
SMB	<b>-0.700</b>	<b>7.03E-07</b>	<b>0.467</b>	<b>0.0027</b>
ELA (WGMS)	<b>0.497</b>	<b>5E-04</b>	-0.170	0.2338
AAR (WGMS)	<b>-0.466</b>	<b>1.4E-03</b>	0.180	0.2173
SMB (WGMS)	<b>-0.477</b>	<b>0.0103</b>	0.363	0.0578

# B

## Scripts

This appendix includes all scripts used to calculate the data given in Appendix A as well as a short flowchart showing in which order the scripts should be run if one were to recreate this study. The scripts have been converted from the original Python and JavaScript files to PDF documents using the Code to PDF tool by Tarik Jaber, available [here](#).

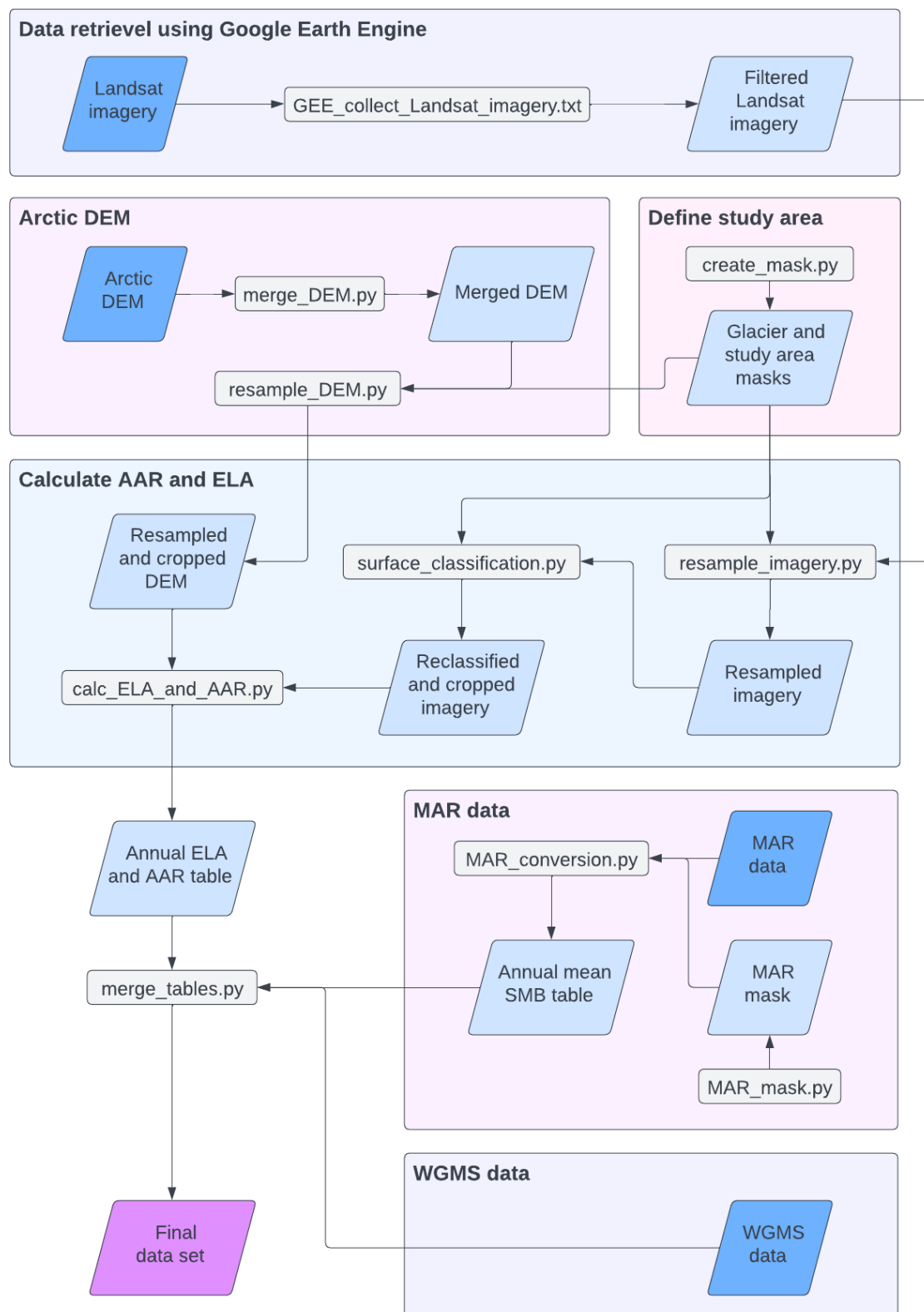


**Figure B.1.:** Flowchart overview of Google Earth Engine and Python scripts

## GEE\_collect\_Landsat\_imagery.txt

```
1 // created on: 2024-03-21
2 // @author: Jasper Heuer, based on Gyula Mate Kovács
3 // use: collect and cloud mask Landsat 5/7/8/9 imagery
4 // comment: 2 geometries: mask_geometry is the outline of the glacier, export_geometry is the
5 // extent of the study area
6
7 // get data =====
8
9 // var dataset = ee.ImageCollection("LANDSAT/LT05/C02/T1_L2")
10 // var dataset = ee.ImageCollection("LANDSAT/LE07/C02/T1_L2")
11 // var dataset = ee.ImageCollection("LANDSAT/LC08/C02/T1_L2")
12 var dataset = ee.ImageCollection("LANDSAT/LC09/C02/T1_L2")
13   .filterDate("2021-01-01", "2024-12-31")
14   .filter(ee.Filter.calendarRange(8, 9, "month"))
15   .filterBounds(mask_geometry); // filter by extent of glacier
16
17 print(dataset); // to check the number of images in unfiltered collection
18
19 // define functions =====
20
21 // define cloud function:
22 function createSnowMask(image) {
23   var qa = image.select('QA_PIXEL'); // extract QA_PIXEL band
24
25   // create masks for snow, cloud, and cloud shadow:
26   var snowMask = qa.bitwiseAnd(1 << 5).neq(0).rename('snowmask');
27   var cloudMask = qa.bitwiseAnd(1 << 3).neq(0).rename('cloudmask');
28   var cloudShadowMask = qa.bitwiseAnd(1 << 4).neq(0).rename('shadowmask');
29
30   // return image with the snow, cloud, and cloud shadow masks as bands:
31   return image.addBands([snowMask, cloudMask, cloudShadowMask]).clip(export_geometry);
32 }
33
34 // define scaling function:
35 function applyScaleFactors(image) {
36   // scale optical bands and thermal band:
37   var opticalBands = image.select('SR_B_').multiply(0.0000275).add(-0.2);
38
39   // add scaled bands to the image:
40   return image.addBands(opticalBands, null, true)
41     .clip(export_geometry);
42 }
43
44 // define cloud ratio function:
45 function cloudRatio(image) {
46   // count cloud pixels:
47   var count = image.select("cloudmask").reduceRegion({
48     reducer: ee.Reducer.histogram(),
49     geometry: mask_geometry, // only ratio above the glacier is of interest
50     scale: 30,
51     maxPixels: 1e10
52 });
53
54   // get histogram values:
55   var histogram = count.get("cloudmask"). getInfo();
56   var ratio = null; // initialize ratio as null
57
58   // handle cloud free/completely cloudy images (histogram length = 1) issue:
59   if (histogram == null) { // check if histogram exists
60     var vals = ee.List(count.get("cloudmask").getInfo()["histogram"]);
61     // check if cloud free/completely cloudy and set ratio accordingly for special cases:
62     if (vals.size().getInfo() == 1) {
63       ratio = vals.get(0).getInfo() == 0 ? 1 : vals.get(0).getInfo() == vals.get(0).getInfo() ? 0 : 0;
64       print(ratio);
65     } else {
66       // calculate cloudiness ratio:
67       var number_of_0_pixels = vals.get(0).getInfo(); // cloud free pixels
68       var number_of_1_pixels = vals.get(1).getInfo(); // cloudy pixels
69       ratio = number_of_1_pixels / (number_of_1_pixels + number_of_0_pixels);
70     }
71   }
72
73   // set cloud ratio as image property:
74   return image.set("CLOUD_RATIO", ratio);
75 }
76
```

```

77 // apply masking =====
78 var dataset = dataset.map(applyScaleFactors).map(createSnowMask); // scale imagery
80
81 // visualize imagery =====
82
83 var visualization = {
84   bands: ['SR_B3', 'SR_B2', 'SR_B1'],
85   min: 0.0,
86   max: 0.5,
87 };
88
89 // visualize true color image, snow mask and cloud mask:
90 Map.addLayer(dataset.first(), visualization, 'True Color');
91 Map.addLayer(dataset.first().select("snowmask"), {min: 0, max: 1, palette:['black', 'white']}, 'Snow Mask');
92 Map.addLayer(dataset.first().select("cloudmask"), {min: 0, max:1, palette:['black', 'red']} , 'Cloud Mask');
93
94 // count cloud pixels =====
95
96 // create list of images:
97 var n_img = dataset.size(). getInfo();
98 var image_list = dataset.toList(n_img);
99 var image_list2 = ee.List([]); // create empty list to store images with cloud ratio
100
101 // loop through images:
102 for(var i = 0; i < n_img; i++) {
103   var image_i = ee.Image(image_list.get(i));
104   var with_ratio = cloudRatio(image_i);
105   image_list2 = image_list2.add(with_ratio);
106 }
107
108 // convert list of cloud ratio imagery into collection:
109 var cloudratio_dataset = ee.ImageCollection.fromImages(image_list2);
110
111 // filter collection by cloud ratio <= 0.1:
112 var filtered_dataset = cloudratio_dataset.filter(ee.Filter.lte("CLOUD_RATIO", 0.1));
113
114 print(filtered_dataset); // check number of images again
115
116 // export imagery =====
117
118 var id = filtered_dataset.aggregate_array("system:index");
119
120 id.evaluate(function(list){
121   list.map(function(id){
122     var image = filtered_dataset.filter(ee.Filter.eq("system:index", id)).first();
123     var mask = filtered_dataset.filter(ee.Filter.eq("system:index", id)).first()
124       .select("cloudmask").lt(1); // reverse mask values
125     var masked_img = image.updateMask(mask);
126
127     Export.image.toDrive({
128       image: masked_img.select(["SR_B1", "SR_B2", "SR_B3", "SR_B4", "SR_B5", "SR_B7"]),
129       scale: 30,
130       region: export_geometry,
131       crs: "EPSG:4326",
132       maxPixels: 1e13,
133       folder: "MITTIVAKKAT_cloud_mask", // change output folder here, if needed
134       description: id,
135       formatOptions: {cloudOptimized: true}
136     });
137   });
138 });
139

```

## merge\_DEM.py

```
1 # -*- coding: utf-8 -*-
2 """
3 created on: 2024-03-18
4 @author: Jasper Heuer
5 use:      merge raster datasets into single file
6 """
7
8 # import packages =====
9
10 import os
11 import glob
12 from osgeo import gdal
13
14 # import data =
15
16 base_path = "C:/Jasper/Master/Thesis/Data/Arctic_DEM/"
17 os.chdir(base_path)
18
19 file_list = glob.glob("./raw/*.tif")
20
21 # merge rasters =====
22
23 vrt = gdal.BuildVRT("./merged.vrt", file_list) # build virtual raster from file list
24 gdal.Translate("./merged_DEM.tif", vrt, xRes=2, yRes=-2) # specify resolution of output raster
25
26 # set data to none:
27 vrt = None
28
29 # clean drive =
30
31 os.remove("./merged.vrt")
32
```

## create\_mask.py

```
1 # -*- coding: utf-8 -*-
2 """
3 created on: 2024-03-19
4 @author: Jasper Heuer
5 use: 1) create raster mask for glacier extent
6       2) polygonize raster to WGS-84 shapefile
7       3) polygonize raster to UTM-24N shapefile
8 """
9
10 # import packages =====
11
12 import os
13 import numpy as np
14 from osgeo import gdal, osr, ogr
15
16 # set working directory =
17
18 base_path = "C:/Jasper/Master/Thesis/Data/"
19 os.chdir(base_path)
20
21 # create raster mask =====
22
23 driver = gdal.GetDriverByName("GTiff")
24
25 # set coordinates:
26 xmin = 547515
27 xmax = 558795
28 ymin = 7283505
29 ymax = 7290015
30
31 # set metadata:
32 outfn = "./Masks/mask.tif"
33 nbands = 1
34 xres = 30
35 yres = -30
36 dtype = gdal.GDT_Int16
37
38 # calculate raster height/width in pixel:
39 xsize = abs(int((xmax-xmin) / xres))
40 ysize = abs(int((ymax-ymin) / yres))
41
42 # create new raster:
43 ds = driver.Create(outfn, xsize, ysize, nbands, dtype)
44 ds.SetProjection("EPSG:32624")
45 ds.SetGeoTransform([xmin, xres, 0, ymax, 0, yres])
46 ds.GetRasterBand(1).Fill(1) # value of raster (and later on shapefile) mask
47 ds.GetRasterBand(1).SetNoDataValue(np.nan)
48
49 # FlushCache to write to disk and set data to none:
50 ds.FlushCache()
51 ds = None
52
53 # polygonize raster mask for WGS84 =====
54
55 src = gdal.Open(outfn) # open mask raster
56 srcband = src.GetRasterBand(1) # get first (and only) band
57
58 shape_driver = ogr.GetDriverByName("ESRI Shapefile")
59 dst = shape_driver.CreateDataSource("./Masks/mask_WGS84.shp")
60
61 sp_ref = osr.SpatialReference()
62 sp_ref.SetFromUserInput('EPSG:4326')
63
64 dst_layername = "mask"
65 dst_layer = dst.CreateLayer(dst_layername, srs = sp_ref)
66
67 # create field in attribute table:
68 fld = ogr.FieldDefn("mask", ogr.OFTInteger)
69 dst_layer.CreateField(fld)
70 dst_field = dst_layer.GetLayerDefn().GetFieldIndex("mask")
71
```

```
72 gdal.Polygonize(srcband, None, dst_layer, dst_field, [], callback=None)
73
74 # set data to none:
75 dst.FlushCache()
76 src = None
77 dst = None
78
79 # polygonize raster mask for UTM-24N =====
80
81 src2 = gdal.Open(outfn) # open mask raster
82 srcband2 = src2.GetRasterBand(1) # get first (and only) band
83
84 shape_driver = ogr.GetDriverByName("ESRI Shapefile")
85 dst2 = shape_driver.CreateDataSource("./Masks/mask_UTM-24N.shp")
86
87 sp_ref2 = osr.SpatialReference()
88 sp_ref2.SetFromUserInput('EPSG:32624')
89
90 dst_layername = "mask"
91 dst_layer = dst2.CreateLayer(dst_layername, srs = sp_ref2)
92
93 # create field in attribute table:
94 fld = ogr.FieldDefn("mask", ogr.OFTInteger)
95 dst_layer.CreateField(fld)
96 dst_field = dst_layer.GetLayerDefn().GetFieldIndex("mask")
97
98 gdal.Polygonize(srcband2, None, dst_layer, dst_field, [], callback=None)
99
100 # set data to none:
101 dst2.FlushCache()
102 src2 = None
103 dst2 = None
104
```

## resample\_DEM.py

```
1 # -*- coding: utf-8 -*-
2 """
3 created on: 2024-03-15
4 @author: Jasper Heuer
5 use: 1) reproject input-DEM to fit Landsat data grid using gdal.Warp
6       2) crop DEM to glacier extent
7 """
8
9 # import packages =====
10
11 import os
12 from osgeo import gdal
13 import numpy as np
14
15 # import data =====
16
17 base_path = "C:/Jasper/Master/Thesis/Data/"
18 os.chdir(base_path)
19
20 # warp raster with gdal =====
21
22 # define meta data:
23 dst_crs = "EPSG:32624" # define destination CRS
24 res = 30 # define resolution in meters
25
26 fn_in = "./Arctic_DEM/merged_DEM.tif"
27 fn_out = "./Arctic_DEM/DEM_reproj.tif"
28 fn_mask = "./Masks/mask.tif"
29
30 # get corner coordinates for mask:
31 mask = gdal.Open(fn_mask)
32 xmin, ymax = mask.GetGeoTransform()[0], mask.GetGeoTransform()[3] # get top left coordinates
33
34 mask = None # set to none
35
36 ds = gdal.Open(fn_in) # read dataset
37 # inspect projection by typing ds.GetProjection() in the console- NOT the editor
38
39 # reproject to common grid:
40 ds_reproj = gdal.Warp(fn_out, ds, dstSRS=dst_crs,
41                       xRes=res, yRes=-res, # specify resolution
42                       cutlineDSName="./Masks/mask_UTM-24N.shp", # cut by extend of mask
43                       cropToCutline=True, dstNodata=np.nan,
44                       resampleAlg="average")
45 # if error with mask, try mask_WGS84.shp instead - projection issues not fully understood yet
46
47 # set data to none:
48 ds = None
49 ds_reproj = None
50
51 # read reprojected data and adjust GeoTransform to exactly align with common grid:
52 ds2 = gdal.Open(fn_out)
53 print(ds2.GetGeoTransform())
54
55 ds2.SetGeoTransform([xmin, res, 0.0, ymax, 0.0, -res]) # change top left coordinates
56 print(ds2.GetGeoTransform())
57
58 # write to disk:
59 driver = gdal.GetDriverByName("GTiff")
60 moved = driver.CreateCopy("./Arctic_DEM/DEM_full_extent.tif", ds2)
61
62 # set data to none:
63 ds2 = None
64 moved = None
65
66 # crop DEM =====
67
68 dem_in = "./Arctic_DEM/DEM_full_extent.tif"
69 dem_out = "./Arctic_DEM/DEM_crop.tif"
70
71 dem_ds = gdal.Open(dem_in)
```

```

72     dem_crop = gdal.Warp(dem_out, dem_ds,
73                           cutlineDSName="./Masks/mittivakkat_outline.shp",
74                           cropToCutline=True, dstNodata=np.nan)
75
76     dem_ds = None
77     dem_crop = None
78
79     # clean drive =====
80
81     os.remove("./Arctic_DEM/DEM_reproj.tif")
82     os.remove("./Arctic_DEM/merged_DEM.tif")
83     os.remove("./Arctic_DEM/DEM_reproj.tif.aux.xml")
84
85     # old version with rasterio =====
86
87     """
88
89     dst_crs = "EPSG:32624"
90
91     with rasterio.open("./Arctic_DEM/14_44_1_1_2m_v4.1/14_44_1_1_2m_v4.1_browse.tif") as src:
92         transform, width, height = calculate_default_transform(
93             src.crs, dst_crs, src.width, src.height, *src.bounds)
94         kwargs = src.meta.copy()
95         kwargs.update({
96             "crs": dst_crs,
97             "transform": transform,
98             "width": width,
99             "height": height
100        })
101
102    with rasterio.open("./Arctic_DEM/14_44_1_1_2m_v4.1/14_44_1_1_2m_v4.1_browse_resample.tif",
103                      "w", **kwargs) as dst:
104        for i in range(1, src.count+1):
105            reproject(
106                source=rasterio.band(src, i),
107                destination=rasterio.band(dst, i),
108                src_transform=src.transform,
109                src_crs=src.crs,
110                dst_transform=transform,
111                dst_crs=dst_crs,
112                resampling=Resampling.nearest)
113
114 """

```

## resample\_imagery.py

```
1 # -*- coding: utf-8 -*-
2 """
3 created on: 2025-03-25
4 @author: Jasper Heuer
5 use: 1) reproject Landsat GEE imagery to common grid
6 2) adjust GeoTransform to line up grids exactly
7 """
8
9 # import packages =====
10
11 import os
12 import glob
13 import time
14 import shutil
15 import numpy as np
16 from osgeo import gdal
17
18 # import data =====
19
20 base_path = "C:/Jasper/Master/Thesis/Data/"
21 os.chdir(base_path)
22
23 start_time = time.time() # set start time
24
25 # create new directories:
26 path_reprojected = "./Landsat/Reprojected"
27 path_resampled = "./Landsat/Resampled"
28
29 if not os.path.exists(path_reprojected):
30     os.makedirs(path_reprojected)
31 if not os.path.exists(path_resampled):
32     os.makedirs(path_resampled)
33
34 # create file list:
35 file_list = glob.glob("./Landsat/GEE_imagery/" + "*.tif", recursive=True)
36
37 # define variables =====
38
39 fn_mask_raster = "./Masks/mask.tif"
40 dst_crs = "EPSG:32624" # destination coordinate system
41 res = 30 # pixel size in meters
42
43 # get corner coordinates for mask:
44 mask = gdal.Open(fn_mask_raster)
45 xmin, ymax = mask.GetGeoTransform()[0], mask.GetGeoTransform()[3]
46
47 mask = None # set to none
48
49 # batch reproject =====
50
51 # create list of dates:
52 date_list = []
53
54 for i in range(0, np.size(file_list)):
55     if file_list[i].split("\\")[1][0:4] == "LT05":
56         date_list.append("LT05_" + file_list[i].split("\\")[1][12:20])
57     elif file_list[i].split("\\")[1][0:4] == "LE07":
58         date_list.append("LE07_" + file_list[i].split("\\")[1][12:20])
59     elif file_list[i].split("\\")[1][0:4] == "LC08":
60         date_list.append("LC08_" + file_list[i].split("\\")[1][12:20])
61     elif file_list[i].split("\\")[1][0:4] == "LC09":
62         date_list.append("LC09_" + file_list[i].split("\\")[1][12:20])
63     else:
64         print("Could not determine sensor for file: " + file_list[i].split("\\")[1])
65         pass
66
67 # run reprojection loop:
68 for i in range(0, np.size(file_list)):
69     print("Reprojecting: " + str(date_list[i]))
70
71     fn_in = file_list[i]
```

```

72     fn_out = "./Landsat/Reprojected/" + str(date_list[i]) + "_reprojected.tif"
73
74     ds = gdal.Open(fn_in) # read dataset
75     # inspect projection by typing ds.GetProjection() in the console- NOT the editor
76
77     # reproject to common grid:
78     ds_reproj = gdal.Warp(fn_out, ds, dstSRS=dst_crs,
79                           xRes=res, yRes=-res,
80                           cutlineDSName="./Masks/mask_UTM-24N.shp", # cut by extend of mask
81                           cropToCutline=True,
82                           outputType=gdal.GDT_Float32, # comment this one out if UInt16 is wanted
83                           dstNodata=np.nan)
84
85     # set data to none:
86     ds = None
87     ds_reproj = None
88
89     print("Done!")
90
91 # batch adjust GeoTransform =====
92
93 reproj_file_list = glob.glob("./Landsat/Reprojected/" + "*tif", recursive=True)
94
95 # create list of dates:
96 reproj_date_list = []
97
98 for i in range(0, np.size(reproj_file_list)):
99     reproj_date_list.append(reproj_file_list[i].split("\\\\")[1][0:13])
100
101 # run GeoTransform adjustment loop:
102 for i in range(0, np.size(reproj_file_list)):
103     print("Adjust GeoTransform: " + str(reproj_date_list[i]))
104
105     ds2 = gdal.Open(reproj_file_list[i])
106     ds2.SetGeoTransform([xmin, res, 0.0, ymax, 0.0, -res]) # adjust GeoTransform
107
108     # save copy to drive
109     driver = gdal.GetDriverByName("GTiff")
110     moved_ds = driver.CreateCopy("./Landsat/Resampled/" + str(reproj_date_list[i]) +
111                                 "_resample.tif", ds2)
112
113     # set data to none:
114     ds2 = None
115     moved_ds = None
116
117     print("Done!")
118
119 # print duration:
120 print(f"Duration: {time.time() - start_time} seconds")
121
122 # clean-up drive =====
123
124 shutil.rmtree("./Landsat/Reprojected") # remove folder
125

```

## surface\_classification.py

```
1 # -*- coding: utf-8 -*-
2 """
3 created on: 2024-03-26
4 @author: Jasper Heuer
5 use:
6     1) calculate ratio of no data pixels
7     2) crop imagery to glacier extent
8     3) classify glacier surface into snow/ice/bedrock based on simple threshold values
9     4) detect border pixels between classes
10 """
11 # import packages =====
12
13 import os
14 import glob
15 import time
16 import rasterio
17 import numpy as np
18 from osgeo import gdal
19 from rasterio.plot import show
20
21 # define variables =====
22
23 base_path = "C:/Jasper/Master/Thesis/Data/"
24 os.chdir(base_path)
25
26 start_time = time.time() # set start time
27
28 # create new directories:
29 path_reclassified = "./Landsat/Reclassified/"
30 path_cropped = "./Landsat/Cropped/"
31 path_borders = "./Landsat/Borders/"
32
33 if not os.path.exists(path_reclassified):
34     os.makedirs(path_reclassified)
35 if not os.path.exists(path_cropped):
36     os.makedirs(path_cropped)
37 if not os.path.exists(path_borders):
38     os.makedirs(path_borders)
39
40 # define file names:
41 fn_mask = "./Masks/mittivakkat_outline.shp"
42 fn_raster_mask = "./Masks/mask.tif"
43 study_area_out = "./Masks/no_data_ratio.tif"
44
45 # define meta data:
46 dst_crs = "EPSG:32624"
47 res = 30
48
49 # calculate number of no data pixels =====
50
51 # create raster where glacier area pixels = 1 and other pixels = 0
52 study_area = gdal.Open(fn_raster_mask)
53 study_crop = gdal.Warp(study_area_out, study_area,
54                         cutlineDSName=fn_mask,
55                         cropToCutline=True,
56                         dstNodata=0)
57
58 # read data:
59 no_data_ds = rasterio.open(study_area_out)
60 no_data_full = no_data_ds.read()
61
62 # count 0- and 1-pixels:
63 no_data_classes, no_data_counts = np.unique(no_data_full, return_counts=True)
64 no_data_dict = dict(zip(no_data_classes, no_data_counts))
65 no_data_sum = sum(no_data_counts)
66
67 # calculate ratio between 0-pixels and total number of pixels:
68 no_data_base_ratio = no_data_dict[0] / no_data_sum
69
70 # batch crop to Mittivakkat mask =====
71
```

```

72     file_list = glob.glob("./Landsat/Resampled/" + "*.tif", recursive=True)
73
74     # create list of dates:
75     date_list = []
76
77     for i in range(0, np.size(file_list)):
78         date_list.append(file_list[i].split("\\")[1][0:13])
79
80     # batch crop imagery:
81     for i in range(0, np.size(file_list)):
82         img_in = file_list[i]
83         img_out = "./Landsat/Cropped/" + str(date_list[i]) + "_cropped.tif"
84
85         img_ds = gdal.Open(img_in)
86
87         # crop imagery to study area:
88         img_crop = gdal.Warp(img_out, img_ds,
89                               cutlineDSName=fn_mask,
90                               cropToCutline=True,
91                               dstNodata=np.nan)
92
93         img_ds = None
94         img_crop = None
95         img_out = None
96
97         print("Cropped: " + str(date_list[i]))
98
99     # batch classify surface =====
100
101    file_list2 = glob.glob("./Landsat/Cropped/" + "*.tif", recursive=True)
102
103    # create list of dates:
104    date_list2 = []
105    for i in range(0, np.size(file_list2)):
106        date_list2.append(file_list2[i].split("\\")[1][0:13])
107
108    # batch reclassify imagery/detect pixels:
109    for i in range(0, np.size(file_list2)):
110        if date_list2[i][0:4] == "LC08" or date_list2[i][0:4] == "LC09":
111            img_ds = rasterio.open(file_list2[i])
112            img_full = img_ds.read()
113            band_01 = img_ds.read(2)
114
115        else:
116            img_ds = rasterio.open(file_list2[i])
117            img_full = img_ds.read()
118            band_01 = img_ds.read(1)
119
120        # reclassify surface based on pixel threshold:
121        reclass = np.where((band_01 > 0.55), 3,
122                           np.where((band_01 ≥ 0.075), 2,
123                                     np.where((band_01 > 0), 1,
124                                             np.where((band_01 == np.nan), 0, 0))))
125
126        # check ratio of no data pixels to number of pixels
127        classes, counts = np.unique(reclass, return_counts=True)
128        classes_dict = dict(zip(classes, counts))
129        number_of_pixels = sum(counts)
130
131        no_data_ratio = classes_dict[0] / number_of_pixels
132
133
134        # filter by amount of no data in study area:
135        if no_data_ratio > (no_data_base_ratio + ((1 - no_data_base_ratio) * 0.2)):
136            print("Skipped image: " + str(file_list2[i].split("\\")[1][0:13]))
137            pass # if more than 20% of the image contains no data, skip image
138
139        else:
140            show(reclass) # plot reclass array
141
142        # detect pixels:
143        borders = np.zeros_like(band_01, dtype=int)
144        x_size, y_size = np.shape(borders)[0], np.shape(borders)[1]

```

```

145 # reclassify pixels based on border-type:
146 for k in range(x_size):
147     for j in range(y_size):
148         # select class 1 (bedrock):
149         if reclass[k,j] == 1:
150             slice = reclass[k-1:k+2, j-1:j+2] # get k1 neighborhood
151             if np.any(slice == 2):
152                 borders[k,j] = 4 # update border pixel value
153             if np.any(slice == 3):
154                 borders[k,j] = 5
155         # select class 2 (ice):
156         if reclass[k,j] == 2:
157             slice = reclass[k-1:k+2, j-1:j+2]
158             if np.any(slice == 3):
159                 borders[k,j] = 6
160             if np.any(slice == 1):
161                 borders[k,j] = 7
162         # select class 3 (snow):
163         if reclass[k,j] == 3:
164             slice = reclass[k-1:k+2, j-1:j+2]
165             if np.any(slice == 2):
166                 borders[k,j] = 8
167             if np.any(slice == 1):
168                 borders[k,j] = 9
169
170     # show(borders) # plot border array
171
172     # save reclass array as GeoTiff:
173     with rasterio.open(
174         "./Landsat/Reclassified/" + str(date_list[i]) + "_reclass.tif",
175         mode="w",
176         driver="GTiff",
177         height=img_full.shape[1],
178         width=img_full.shape[2],
179         count=img_full.shape[0],
180         dtype=img_full.dtype,
181         crs=img_ds.crs,
182         transform=img_ds.transform
183     ) as dst:
184         dst.write(reclass, 1)
185
186     # save border array as GeoTiff:
187     with rasterio.open(
188         "./Landsat/Borders/" + str(date_list[i]) + "_borders.tif",
189         mode="w",
190         driver="GTiff",
191         height=img_full.shape[1],
192         width=img_full.shape[2],
193         count=img_full.shape[0],
194         dtype=img_full.dtype,
195         crs=img_ds.crs,
196         transform=img_ds.transform
197     ) as dst:
198         dst.write(borders, 1)
199
200     print("Reclassified: " + str(date_list[i]))
201
202     # print duration:
203     print(f"Duration: {time.time() - start_time} seconds")
204

```

## calc\_ELA\_and\_AAR.py

```
1 # -*- coding: utf-8 -*-
2 """
3 created on: 2024-03-26
4 @author: Jasper Heuer
5 use: 1) calculate ELA and AAR for glacier
6       2) export data as CSV table
7 """
8
9 # import packages -----
10
11 import os
12 import glob
13 import time
14 import rasterio
15 import numpy as np
16 import pandas as pd
17
18 from osgeo import gdal
19 from datetime import datetime
20
21 # import data -----
22
23 base_path = "C:/Jasper/Master/Thesis/Data/"
24 os.chdir(base_path)
25
26 # import DEM:
27 dem_fn = "./Arctic_DEM/DEM_crop.tif"
28 dem_ds = rasterio.open(dem_fn)
29 dem = dem_ds.read(1)
30
31 # create list of reclass and border rasters:
32 reclass_list = glob.glob("./Landsat/Reclassified/" + "*.tif", recursive=True)
33 border_list = glob.glob("./Landsat/Borders/" + "*.tif", recursive=True)
34
35 # calculate ELA and AAR -----
36
37 start_time = time.time()
38
39 year_list = []
40 month_list = []
41 day_list = []
42 date_list = []
43 ELA_list = []
44 AAR_list = []
45 acc_list = []
46 abl_list = []
47
48 # loop over dates:
49 for i in range(0, np.size(reclass_list)):
50     border_ds = rasterio.open(border_list[i])
51     border = border_ds.read(1)
52
53     reclass_ds = rasterio.open(reclass_list[i])
54     reclass = reclass_ds.read(1)
55
56     year_list.append(border_list[i].split("\\\\")[-1][5:9])
57     month_list.append(border_list[i].split("\\\\")[-1][9:11])
58     day_list.append(border_list[i].split("\\\\")[-1][11:13])
59     date_list.append(border_list[i].split("\\\\")[-1][5:13])
60
61     # check that we are using the same date for ELA and AAR:
62     if border_list[i].split("\\\\")[-1][0:13] == reclass_list[i].split("\\\\")[-1][0:13]:
63         heights = []
64         x_coords = []
65         y_coords = []
66
67         # calculate ELA:
68         for k in range(0, border.shape[0]):
69             for j in range(0, border.shape[1]):
70                 if border[k,j] == 8:
71                     heights.append(dem[k,j])
```

```

72             x_coords.append(j)
73             y_coords.append(k)
74
75             ELA_array = np.array((x_coords, y_coords, heights)).T
76             ELA = np.mean(ELA_array[:, 2])
77
78             print("ELA calculated at date: "
79                  + str(year_list[i]) + str(month_list[i]) + str(day_list[i]))
80
81             # create dictionary with pixel counts for each class:
82             classes, counts = np.unique(reclass, return_counts=True)
83             classes_dict = dict(zip(classes, counts))
84
85             # calculate AAR (and handle special cases):
86             if 2 in classes_dict: # 2 = ice pixels
87                 if 3 in classes_dict: # 3 = snow pixels
88                     total_area = classes_dict[2] + classes_dict[3]
89                     accumulation_area = classes_dict[3]
90                     AAR = accumulation_area/total_area
91                     acc_size = classes_dict[3] * 900 # calculate size of accumulation area in m²
92                     print("AAR calculated at date: "
93                           + str(year_list[i]) + str(month_list[i]) + str(day_list[i]))
94                 else:
95                     AAR = 0
96                     ELA = 1020 # set ELA to max elevation of glacier
97                     acc_size = 0
98                     print("No snow pixels identified at date: "
99                           + str(year_list[i]) + str(month_list[i]) + str(day_list[i]))
100            elif 3 in classes_dict:
101                AAR = 1
102                acc_size = total_area * 900
103                print("No ice pixels identified at date: "
104                    + str(year_list[i]) + str(month_list[i]) + str(day_list[i]))
105            else:
106                AAR = np.nan
107                acc_size = np.nan
108                print("No snow or ice pixels identified at date: "
109                    + str(year_list[i]) + str(month_list[i]) + str(day_list[i]))
110            pass
111
112            # create output lists:
113            AAR_list.append(AAR)
114            ELA_list.append(ELA)
115            acc_list.append(acc_size / 1000000) # in km²
116            abl_list.append(((total_area *900) - acc_size) / 1000000) # in km²
117
118        else:
119            print("Border and reclass rasters not from the same date!")
120            pass
121
122    # create output array =====
123
124    data_array = np.array((year_list, month_list, day_list, date_list,
125                           ELA_list, AAR_list, acc_list, abl_list)).T
126
127    df = pd.DataFrame(data=data_array, columns=["Year", "Month", "Day", "Date", "ELA", "AAR",
128                                                 "Accumulation_area", "Ablation_area"])
129    df = df.sort_values(by=["Year", "Month", "Day"], axis=0, ascending=True) # sort dataframe by date
130    df = df.reset_index() # reset index
131    df = df.drop("index", axis=1) # drop old index column
132
133    # get lowest AAR per year ("true" AAR):
134    df_analysis = df.loc[df.groupby("Year").AAR.idxmin()].reset_index(drop=True)
135
136    # export data to disk:
137    df.to_csv("./CSV/ELA_AAR_complete_table_" + datetime.now().strftime("%Y%m%d_%H%M%S") + ".csv",
138              sep=",")
139    df.to_csv("./CSV/ELA_AAR_complete_table_latest.csv", sep=",")
140
141    df_analysis.to_csv("./CSV/ELA_AAR_analysis_table_" + datetime.now().strftime("%Y%m%d_%H%M%S")\
142                      + ".csv", sep=",")
143    df_analysis.to_csv("./CSV/ELA_AAR_analysis_table_latest.csv", sep=",")
144
```

```

145 # export images used in analysis =====
146
147 path_analysis = "./Landsat/Analysis_images/"
148 if not os.path.exists(path_analysis):
149     os.makedirs(path_analysis)
150
151 # create file list:
152 file_list = glob.glob("./Landsat/Cropped/" + "*.tif", recursive=True)
153 file_list2 = glob.glob("./Landsat/Reclassified/" + "*.tif", recursive=True)
154
155 # create date list:
156 date_list = list((df_analysis["Date"]))
157
158 # check if image is used for analysis and create copy in new folder:
159 i = 0
160 for i in range(0, len(file_list)):
161     file_date = file_list[i].split("\\\\")[-1][5:13]
162     if str(file_date) in date_list:
163         driver = gdal.GetDriverByName("GTiff")
164         ds = gdal.Open(file_list[i])
165         ds = driver.CreateCopy("./Landsat/Analysis_images/" + file_list[i].split("\\\\")[-1][0:13] +
166                               "_analysis.tif", ds)
167         ds = None
168     else:
169         pass
170
171 for i in range(0, len(file_list2)):
172     file_date = file_list2[i].split("\\\\")[-1][5:13]
173     if str(file_date) in date_list:
174         driver = gdal.GetDriverByName("GTiff")
175         ds = gdal.Open(file_list2[i])
176         ds = driver.CreateCopy("./Landsat/Analysis_images/" + file_list2[i].split("\\\\")[-1][0:13] +
177                               "_analysis_reclass.tif", ds)
178         ds = None
179     else:
180         pass
181
182
183 # print duration:
184 print(f"Duration: {time.time() - start_time} seconds")
185

```

## MAR\_mask.py

```
1 # -*- coding: utf-8 -*-
2 """
3 created on: 2024-05-24
4 @author: Jasper Heuer
5 use:      create mask for MAR resample and cropping of raw data
6 """
7
8 # import packages =====
9
10 import os
11 import numpy as np
12 from osgeo import gdal, osr, ogr
13
14 # set working directory =====
15
16 base_path = "C:/Jasper/Master/Thesis/Data/"
17 os.chdir(base_path)
18
19 # create raster mask =====
20
21 driver = gdal.GetDriverByName("GTiff")
22
23 # set coordinates (by adding 5000m * np.sqrt(2) in each direction to get all MAR pixels):
24 xmin = 547515 - (5000 * np.sqrt(2)) # = length of diagonal of 5000m pixel
25 xmax = 558795 + (5000 * np.sqrt(2))
26 ymin = 7283505 - (5000 * np.sqrt(2))
27 ymax = 7290015 + (5000 * np.sqrt(2))
28
29 # set metadata:
30 outfn = "./Masks/MAR_mask.tif"
31 nbands = 1
32 xres = 30
33 yres = -30
34 dtype = gdal.GDT_Int16
35
36 # calculate raster height/width in pixel:
37 xsize = abs(int((xmax-xmin) / xres))
38 ysize = abs(int((ymax-ymin) / yres))
39
40 # create new raster:
41 ds = driver.Create(outfn, xsize, ysize, nbands, dtype)
42 ds.SetProjection("EPSG:32624")
43 ds.SetGeoTransform([xmin, xres, 0, ymax, 0, yres])
44 ds.GetRasterBand(1).Fill(1) # value of raster (and later on shapefile) mask
45 ds.GetRasterBand(1).SetNoDataValue(np.nan)
46
47 # FlushCache to write to disk and set data to none:
48 ds.FlushCache()
49 ds = None
50
51 # polygonize raster mask for WGS84 =====
52
53 # read mask file:
54 src = gdal.Open(outfn) # open mask raster
55 srcband = src.GetRasterBand(1) # get first (and only) band
56
57 # define driver:
58 shape_driver = ogr.GetDriverByName("ESRI Shapefile")
59 dst = shape_driver.CreateDataSource("./Masks/MAR_mask_UTM-24N.shp")
60
61 # set CRS:
62 sp_ref = osr.SpatialReference()
63 sp_ref.SetFromUserInput('EPSG:32624')
64
65 # create new layer:
66 dst_layername = "mask"
67 dst_layer = dst.CreateLayer(dst_layername, srs = sp_ref)
68
69 # create field in attribute table:
70 fld = ogr.FieldDefn("mask", ogr.OFTInteger)
71 dst_layer.CreateField(fld)
```

```
72 dst_field = dst_layer.GetLayerDefn().GetFieldIndex("mask")
73
74 # polygonize raster to shapefile:
75 gdal.Polygonize(srcband, None, dst_layer, dst_field, [], callback=None)
76
77 # set data to none:
78 dst.FlushCache()
79 src = None
80 dst = None
81
```

---

## MAR\_conversion.py

```
1 # -*- coding: utf-8 -*-
2 """
3 created on: 2024-05-20
4 @author: Jasper Heuer
5 use: 1) convert NetCDF files to GeoTIFF
6       2) adjust GDAL affine matrix
7       3) crop to study area and export
8 """
9
10 # import packages =====
11
12 import os
13 import glob
14 import time
15 import shutil
16 import rasterio
17 import numpy as np
18 import pandas as pd
19 import xarray as xr
20
21 from osgeo import gdal
22 from datetime import datetime
23
24 # need to have rasterio and rioxarray installed
25
26 # import data =====
27
28 basepath = "C:/Jasper/Master/Thesis/Data/"
29 os.chdir(basepath)
30
31 start_time = time.time() # set start time
32
33 # create new directories:
34 path_geotiff = "./MAR/daily_5km_tiff/"
35 path_cropped = "./MAR/daily_5km_cropped/"
36 path_resampled = "./MAR/daily_5km_resampled/"
37
38 if not os.path.exists(path_geotiff):
39     os.makedirs(path_geotiff)
40 if not os.path.exists(path_cropped):
41     os.makedirs(path_cropped)
42 if not os.path.exists(path_resampled):
43     os.makedirs(path_resampled)
44
45 # create file list:
46 file_list = glob.glob("./MAR/daily_5km_raw/" + "*.nc", recursive=True)
47
48 # create list of dates:
49 date_list = []
50
51 for i in range(0, np.size(file_list)):
52     date_list.append(file_list[i].split("ERA5-")[1][0:4])
53
54 # convert data to GeoTIFF format =====
55
56 for i in range(0, np.size(file_list)):
57     # read data:
58     ds = xr.open_dataset(file_list[i], decode_coords="all")
59
60     # create list of days:
61     start_day = datetime.strptime(str(date_list[i]) + "-01-01", "%Y-%m-%d")
62     print(start_day)
63     year_length = len(ds.coords["TIME"])
64     day_list = pd.date_range(start_day, periods=year_length)
65
66     # read and export surface mass balance data:
67     for j in range(0, len(ds.coords["TIME"])):
68         smb = ds["SMB"][j]
69
70         # set spatial extent and CRS:
71         smb = smb.rio.set_spatial_dims(x_dim="x", y_dim="y")
```

```

72     smb.rio.write_crs("epsg:3413", inplace=True) # CSR of MAR data
73
74     # export as GeoTIFF:
75     smb.rio.to_raster(path_geotiff + "MAR_SMB_" + str(day_list[j])[0:10] + ".tif")
76
77     print("Exported: " + str(file_list[i].split("\\\\")[-1][0:-3]))
78
79 # adjust GDAL affine matrix =====
80
81 file_list2 = glob.glob(path_geotiff + "*.tif", recursive=True)
82
83 for i in range(0, np.size(file_list2)):
84     # read data:
85     data = gdal.Open(file_list2[i])
86     geotrans = data.GetGeoTransform()
87
88     # calculate new transform matrix:
89     new_geotransform = [geotrans[0] * 1000, geotrans[1]* 1000, 0.0,
90                         geotrans[3] * 1000, 0.0, geotrans[5] * 1000]
91
92     # set new transform:
93     data.SetGeoTransform(new_geotransform)
94
95     # reproject to common grid:
96     data_resample = gdal.Warp(path_resampled + str(file_list2[i].split("\\\\")[-1][0:-4]) + "_res.tif",
97                               data, dstSRS="EPSG:32624", xRes=30, yRes=-30,
98                               cutlineDSName=".\\Masks\\MAR_mask_UTM-24N.shp", # cut by extent of mask
99                               cropToCutline=True,
100                              outputType=gdal.GDT_Float32, # comment this one out if UInt16 is wanted
101                              dstNodata=np.nan)
102
103     # set data to none:
104     data = None
105     data_resample = None
106
107     # read resampled data:
108     data = gdal.Open(path_resampled + str(file_list2[i].split("\\\\")[-1][0:-4]) + "_res.tif")
109
110     # crop data to extent of study area:
111     data_cropped = gdal.Warp(path_cropped + str(file_list2[i].split("\\\\")[-1][0:-4]) + "_crop.tif",
112                               data, dstSRS="EPSG:32624", xRes=30, yRes=-30,
113                               cutlineDSName=".\\Masks\\mittivakkat_outline.shp", # cut by extend of mask
114                               cropToCutline=True,
115                               outputType=gdal.GDT_Float32, # comment this one out if UInt16 is wanted
116                               dstNodata=np.nan)
117
118     # set data to none:
119     data = None
120     data_cropped = None
121
122     print("Adjusted geotransform and cropped: " + str(file_list2[i].split("\\\\")[-1][0:-4]))
123
124 # create SMB time series =====
125
126 # create file list:
127 file_list3 = glob.glob("./MAR/daily_5km_cropped/" + "*.tif", recursive=True)
128
129 year_list = []
130 month_list = []
131 day_list = []
132 date_list = []
133
134 # extract date loop:
135 for i in range(0, np.size(file_list3)):
136     year_list.append(file_list3[i].split("SMB_")[-1][0:4])
137     month_list.append(file_list3[i].split("SMB_")[-1][5:7])
138     day_list.append(file_list3[i].split("SMB_")[-1][8:10])
139     date_list.append(file_list3[i].split("SMB_")[-1][0:10])
140
141 # extract daily SMB:
142 smb_list = []
143
144 for i in range(0, np.size(file_list3)):
```

```
145     data = rasterio.open(file_list3[i])
146     raster = data.read()
147
148     smb = np.nanmean(raster)
149     smb_list.append(smb)
150
151 array = np.array((year_list, month_list, day_list, date_list, smb_list)).T
152
153 df = pd.DataFrame(array, columns=["Year", "Month", "Day", "Date", "SMB"])
154 df["Date"] = pd.to_datetime(df["Date"])
155 df["Date"] = df["Date"].dt.strftime("%Y%m%d")
156
157 df = df.sort_values(by=["Year", "Month", "Day"], axis=0, ascending=True) # sort dataframe by date
158
159 # export to disk:
160 df.to_csv("./CSV/SMB_table_" + datetime.now().strftime("%Y%m%d_%H%M%S") + ".csv", sep=",")
161 df.to_csv("./CSV/SMB_table_latest.csv", sep=",")
162
163 # clean up drive =====
164
165 shutil.rmtree("./MAR/daily_5km_resampled/")
166 shutil.rmtree("./MAR/daily_5km_tiff/")
167
168 # print duration:
169 print(f"Duration: {time.time() - start_time} seconds")
170
```

## merge\_tables.py

```
1 # -*- coding: utf-8 -*-
2 """
3 Created on: 2024-05-20
4 @author: Jasper Heuer
5 use: merge all data into final analysis table
6 """
7
8 # import packages =====
9
10 import os
11 import numpy as np
12 import pandas as pd
13 from datetime import datetime
14
15 # import data =====
16
17 basepath = "C:/Jasper/Master/Thesis/Data/"
18 os.chdir(basepath)
19
20 # read own data:
21 smb = pd.read_csv("./CSV/SMB_table_latest.csv", sep=",")
22 aar = pd.read_csv("./CSV/ELA_AAR_analysis_table_latest.csv")
23 aar = aar.loc[aar.groupby("Year").AAR.idxmin()].reset_index(drop=True) # get lowest AAR per year
24
25 # read WGMS ELA and AAR data:
26 wgms = pd.read_csv("./Other/DOI-WGMS-FoG-2024-01/data/mass_balance_overview.csv", sep=",")
27 wgms["NAME"] = "MITTIVAKKAT"
28 wgms = wgms[["YEAR", "ELA", "AAR"]]
29
30 # adjust scaling issue:
31 wgms["ELA"] = wgms["ELA"]
32 wgms["AAR"] = wgms["AAR"] / 100 # missing decimal point and expressed in percent
33
34 # read WGMS mass balance data:
35 wgms_mass = pd.read_csv("./Other/DOI-WGMS-FoG-2024-01/data/mass_balance.csv", sep=",")
36
37 # lower bound = 9999 singles out rows with value for the entire glacier:
38 wgms_mass = wgms_mass[(wgms_mass["NAME"] == "MITTIVAKKAT") & (wgms_mass["LOWER_BOUND"] == 9999)]
39 wgms_mass = wgms_mass[["YEAR", "ANNUAL_BALANCE"]]
40 wgms_mass["ANNUAL_BALANCE"] = wgms_mass["ANNUAL_BALANCE"]
41
42 wgms = wgms.merge(wgms, on="YEAR")
43 wgms = wgms.rename(columns={"YEAR": "Year"})
44
45 # get annual SMB =====
46
47 date_list = []
48 index_list = [623] # initialize with index of 15th of September 1984
49 smb_list = []
50 hydro_list = []
51
52 for i in range(0, len(aar)):
53     date_list.append(aar["Date"][i])
54
55 for i in range(0, len(date_list)):
56     index = smb[(smb["Date"] == date_list[i])].index[0]
57     index_list.append(index)
58
59 # insert 15th of September as season end for no data years:
60 index_list.insert(10, 4275)
61 index_list.insert(24, 9389)
62 index_list.insert(26, 10119)
63
64 # calculate annual SMB:
65 for i in range(0, len(index_list)-1):
66     section = smb[(smb.index > index_list[i]) & (smb.index <= index_list[i+1])]
67     total_smb = sum(section["SMB"])
68     smb_list.append(total_smb)
69
70 # calculate length of melt season:
71 for i in range(0, len(index_list)-1):
```

```

72     hydro_year_length = index_list[i+1] - index_list[i]
73
74     # manage unrealistically long melt seasons, due to missing data in year before:
75     # (not really needed anymore)
76     if hydro_year_length > 500:
77         hydro_year_length_length = np.nan
78
79     hydro_list.append(hydro_year_length)
80
81 # create dataframe =====
82
83 aar = aar.drop("Unnamed: 0", axis=1)
84
85 # create list with all years:
86 year_list = pd.DataFrame(np.arange(1985, 2024, 1), columns=["Year"])
87
88 df = year_list.merge(aar, on="Year", how="outer")
89 df = df.merge(wgms, on="Year", how="outer")
90 df = df.merge(sens_df, on="Year", how="outer")
91
92 df["SMB"] = smb_list
93 df["Hydro_year"] = hydro_list
94
95 df = df.rename(columns={"ELA_X": "ELA", "AAR_X": "AAR", "ANNUAL_BALANCE": "WGMS_SMB",
96                      "ELA_y": "WGMS_ELA", "AAR_y": "WGMS_AAR"})
97
98 # export to disk:
99 df.to_csv("./CSV/complete_table_" + datetime.now().strftime("%Y%m%d_%H%M%S") + ".csv", sep=",")
100 df.to_csv("./CSV/complete_table_latest.csv", sep=",")
101 df.to_excel("./CSV/complete_table_latest.xlsx")
102

```